Wind Energy Science, Engineering and Policy

National Science Foundation

Research Experiences for Undergraduates

Symposium Proceedings

8 August 2012

IOWA STATE UNIVERSITY

Preface

This volume brings together the research results of a remarkable group of ten undergraduates who came together at Iowa State University for 10 weeks to apply their skills at scientific research. Without prior experience in these research areas or familiarity with each other, these students from across the US converged on the Iowa State campus in the summer of 2012 to learn about the science, engineering and policy relating to one of the most promising areas of renewable energy. As a fast-track into the science and engineering underpinning wind energy they participated in a short course, Lunch & Learn, and webinar sessions led by faculty, industry professionals, wind energy entrepreneurs and others engaged in the wind power enterprise. They toured operating utility-scale wind farms, an energy utility trading floor, turbine-components manufacturing plants, a research wind tunnel, and a meteorological field observing site in an operating wind farm.

Students practiced and honed their research skills in faculty-led research program under daily guidance of postdoctoral research associates, graduate students and laboratory supervisors. During their 10-week stays students weekly produced an updated draft on their research project in the form of a journal paper. They also attended an off-campus science meeting where they presented individual project posters describing their work. Their final products include the journal-targeted papers that comprise this volume and 20-minute power-point presentations of their findings in a symposium attended by mentors and other researchers and students in the Iowa State University community. But they also took some time off to experience the Iowa State Fair!

As you page though this compilation of research results you should note the diversity of topics all relating the general theme of wind energy. This permanent record of their achievements would not be possible without the dedication and assistance of the research mentors listed on their individual papers, along with the many faculty members at Iowa State, wind energy industry professionals, and support staff in the College of Engineering. And the day-to-day tasks necessary to run such a program would never have been accomplished had it not been for the tireless efforts of Ms. Barbara Brown, who was assisted by Ms. Katherine Rice on the capstone task of assembling and editing this proceedings.

Financial support for the program was provided by the National Science Foundation under grant number 1063048.

Eugene S. Takle
Principal Investigator

James D. McCalley
Co-Principal Investigator

August 2012

A copy of this proceedings or individual papers herein can be obtained by contacting via email gstakle@iastate.edu , jdm@iastate.edu, or by visiting http://www.windenergy.iastate.edu/reu.asp

TABLE OF CONTENTS

Wind Energy Science Engineering and Policy

Undergraduate Research Symposium

3041 Coover Hall

Wednesday 8 August 2012

8:25 Symposium Opening Remarks: Gary Mirka, Associate Dean, College of Engineering

8:30 **Development of an Automated Fabric Deformation System for Composite Wind Turbine Blade Manufacturing**
David Deisenroth Mentors: Dr. Matt Frank and Siqi Zhu

8:50 **Life Cycle Assessment of Taller Wind Turbines With Four Different Tower Designs**
Sarah A. Gustitus Mentors: Dr. Sri Sritharan and Dr. Say Kee Ong

9:10 **Analysis of Ramp Events and Two-Day Persistence Forecast Accuracy at 80 m**
Renee A. Showers Walton Mentor: Dr. William Gallus, Jr.

9:30 **Influence of Wind Turbines on Atmospheric Stability and Dew Duration**
Matthew J. Lauridsen Mentors: Dr. Eugene S. Takle and Daniel J. Rajewski

9:50 **Compression Failure in Marcels of Wind Turbine Blades**
Travis L. Tasker Mentors: Dr. Vinay Dayal, Lisa Brasche, and Ryan Kafka

10:10 Break

10:30 **Analysis of Biorenewable Precursor Fibers Formed From Blending Polylactic Acid, Butyrated Lignin, and Grafted Lignin**
Edward J. Angus Mentors: Dr. Michael Kessler, M. Thunga, G. Ramasubramanian

10:50 **Wind Farm Arrangement: Considering the Influence of Complex Terrain andTurbine Wake Interactions**
S. Rose Eilenberg Mentors: Dr. Hui Hu and Wei Tian

11:10 **Frequency Dynamic Impact by a Transmission Overlay in a Renewable Sourced Power System**
Elena C. Hoff Mentors: Dr. Dionysios Aliprantis and Hugo Villegas-Pico

11:30 **Recycling Turbine Blade Composites: Concrete Aggregate and Reinforcement**
Michael Hofmeister Mentors: Dr. Frank Peters, Dr. Sritharan, and Wenjun He

Analysis of Wind Turbine Noise Using Semi-Empirical Noise Simulation Software
Samuel Frishman Mentors: Dr. Anupam Sharma and Sunil Arolla
(this report was presented Aug 3)

11:50 Symposium Closing Remarks

Faculty, staff, mentors, and students are encouraged to attend

Development of an Automated Fabric Deformation System for Composite Wind Turbine Blade Manufacturing

DAVID DEISENROTH
Wind Energy Science Engineering and Policy REU, Iowa State University, Ames, Iowa
Mentors: Dr. Matt Frank and Siqi Zhu

Abstract

Large-scale wind turbine blades currently require intensive human labor during the fabric layup process. The intent of this work is to automate the idea of in-plane shifting fiberglass fabric as a way of increasing the automation of wind blade manufacturing.
The fiberglass fabric shifting method may be particularly useful for making fabric bend around curves in wind blade molds, without producing waves or wrinkles that can reduce the fatigue life. Laser scanning was used to show that shifted fabric samples can be produced through automated means, without out-of-plane deformation.
The capabilities of the automated shifting head were tested by producing a fabric sample with geometry that is much more extreme than required for wind blade manufacturing.
The tendency of fiberglass fabric to spring-back toward its original orthogonal orientation was observed. The fabric spring-back data obtained were statistically inconclusive, but some qualitative trends were observed and should be further investigated in future work. A strong correlation between shift angle and fabric spring-back severity will be necessary for developing reliable and consistent fiberglass fabric shifting manufacturing methods for wind blades.

1. Introduction

Large-scale wind turbine blades currently require intensive human labor during the fabric layup process. The current method of fabric layup requires workers to place and adjust the fabric until it lays as smooth as possible in the mold. Studies have been conducted to test the viability of in-plane shifting the fabric to decrease the amount of human labor required to adequately seat the fabric in the mold [1]. The intent of this project is to test the viability of an automated system that will form, or shift the fabric in-plane. The goal is to decrease the amount of human involvement and variability in the layup process. In particular, "shifting" could be an effective automation method for making fabric bend around the curvature of the blade without causing waves or wrinkles in the fabric. An improved fabric layup process could decrease manufacturing cost, decrease the amount of material needed, and increase fatigue life of wind turbine blades, therefore decreasing the unit cost of wind energy production [2].

2. Literature review

Composites are used in a wide array of applications including aerospace, automotive, recreation, nautical, and wind energy. Composites tend to have a high strength-to-weight ratio, as well as excellent adaptability for creating complex shapes. Composite materials consist of a fiber reinforcement contained within a polymer matrix. The combination of the high strength fiber and the polymer matrix are the cause of composites' respectable strength and weight qualities.

Composite components are formed in a mold which serves as a boundary to contain and shape the component. The components made from these materials often have

complex geometries that require the fiber material to adapt to surfaces with compound curves. The fiber can be applied in several ways; one method is to spray fibers and resin into the mold. Another method is to lay fiber fabric sheets into the mold, put a vacuum bag over the fabric, and use the vacuum to draw the resin into the component. A third method is to pre-impregnate strips of fabric with resin (prepreg), then lay the strips into the mold. The large scale of wind blades requires a large volume of fiber, so large sections of fiber fabric are the most practical way of placing the fiber in the mold. Wind blade components are also thick, requiring many layers, or plies, of fiber fabric.

The most common type of fiberglass fabric used for wind blade manufacture is unidirectional (UD) fabric. Fiberglass fabrics are made of grouped bundles, or tows, of fiber strands. In unidirectional fiberglass fabrics, the "number 1" orientation tows are large and run straight for the length of fabric. The number 2 orientation tows are much smaller and serve to keep the number 1 tows together to create sheets of fabric, as shown in Figure 1. Unidirectional fabrics are defined as non-crimp fabrics (NCF) because the number 1 tows do not have waves created by bending around the number 2 tows [1].

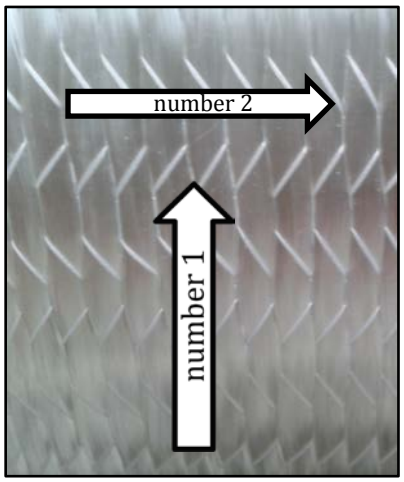

Figure 1: Unidirectional (UD) fiberglass fabric.

Wind blades have a complex geometry for aerodynamic efficiency, which makes fabric application, or layup, a difficult and expensive process. Currently, the non-prismatic shapes of wind blades require a mold. With current technologies, the most economically viable way to manufacture wind blades is to have workers manually manipulate the fabric until it lays as flat as possible in the mold. The complex motions human hands create while laying and seating the fiber in the mold are difficult to replicate with an automated system because they are based on sensory input [4].

There are several automated methods for applying fiber fabric to the mold. One technique is to pre-impregnated (prepreg) the fabric with resin before it is laid in the mold. The resin is cured enough to have a tacky quality that keeps it secured to the surface of the mold and other layers of fabric. The automated prepreg method is commonly used in aerospace applications where cost is not such a limiting factor. The automated prepreg method is commonly referred to as "tape layup." The strips of tape are narrow, which causes the prepreg method to be expensive. It is currently not practical to use prepreg tape layup for large wind blade manufacturing [5].

Another automated fabric forming method is vacuum forming. In the vacuum forming layup process, fabric is placed on a positive mold. A negative mold is then place on top of the fabric. A vacuum is then applied and the negative pressure forces the molds together, distributing the fabric and causing the resin to flow into the part. The vacuum forming method is not suitable for wind blade manufacture because of the large scale of molds required [6].

Attempts have been made to outfit a robotic arm with common layup tools to effectively mimic the hand movements of workers seating the fabric in the mold. The robotic arm used sensory input to apply the

appropriate amount of pressure to the tools to adequately manipulate the fabric. This method is also very expensive and not practical for the large scale of wind blade manufacturing [4].

One critical aspect of the fabric layup process is preventing out-of-plane deformation of the fabric. Out-of-plane deformation occurs when some of the tows are forced to span a shorter distance than the corresponding parallel tows in the fabric. The tows that span the shorter distance are compressed, causing them to buckle, which then causes a wave to form in the fabric. If the wave is large enough, it will fold back on itself and become a wrinkle [1]. Waves and wrinkles cause significant decreases in the strength of the composite component. As the size of the wave increases, the ultimate strength of the composite decreases correspondingly [2].

Mathematical models have been developed to understand the behavior of fabric and how it can be manipulated to fit complex geometries. The most widely accepted is the pin jointed net (PJN) model. In this model, the fabric is composed of segments joined by pins at each tow intersection. This model is very useful for simulating fabric deformations, but it does not account for all of the behaviors of real fabric, such as slippage of the tows. The PJN model has been used to model the deformations in fabric and understand the deformations required to fit compound curves [7, 8, 9].

It has been shown that in-plane deformation is necessary for fitting the fabric into molds with complex geometry [6]. Using a theory based on the PJN model, it has been shown that fabric can be deformed in-plane to follow in-plane curves, without out-of-plane deformation. If strategically planned, in-plane deformation can be used to increase the fabric's ability to seat smoothly in the mold. One type of in-plane deformation is achieved by holding an end of the fabric steady while sliding the other end parallel to it. This type of deformation will be referred to as "shifting," because it effectively shifts the tows from their original rectangular shape into a parallelogram, as shown in Figure 2, below.

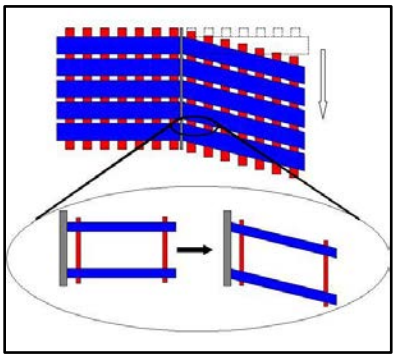

Figure 2: Visual representation the effect of shifting on unidirectional fiberglass fabric [1].

Multiple shifts with varying spacing and shift angle can closely approximate smooth curves while preventing out-of-plane deformation, as shown in Figure 3, below. The shifted sample, on the right, shows nearly no out-of-plane deformation, while the steered sample, on the left shows a direct correlation between the curvature (inverse of radius) of the sample and the magnitude of out-of-plane deformation [1].

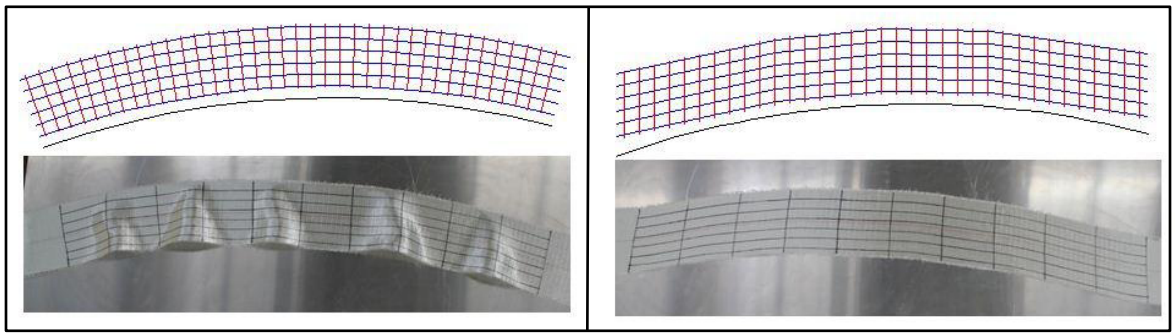

Figure 3: Steering schematic and steered sample compared to shifting schematic and shifted sample [1].

It has also been shown that in-plane shifting the fabric improves the fatigue life of the composite material by preventing out-of-plane deformation. Magnussen compared fabric samples of the same curvature that were formed with shifting and steering. When making the steered samples, the fabric was simply bent around the curvature, uniformly curving the number 1 tows, and aligning the number 2 tows radially. In the steered samples, waves formed because tows at the inside of the curve were forced to span a shorter distance. When the fatigue life of the steered samples was compared to the shifted samples, the shifted samples showed significantly higher fatigue life. As the curvature increased, the fatigue life of the steered samples decreased asymptotically to 1 cycle. The fatigue life of the shifted samples was unaffected by the amount of curvature of the fabric samples, because the tows remained parallel, the out-of-plane deformation was negligible [1].

Magnussen also showed that as the number of discrete shifts in the fabric samples increased, so did the fatigue life [1]. Samples were created with a fixed curvature, and the number of discrete shifts used to approximate the curvature was varied. The point at which the tows are bent was commonly the failure point of the samples. As the number of shifts increased, the severity of each shift decreased and the fatigue life increased asymptotically toward an ideal number of cycles that would be achieved if the tows were shifted in a smooth arc. Magnussen concluded that the shifting method is a feasible way to deform fabric in-plane without causing out-of-plane deformation, as well as that shifting fabric creates mechanically superior fiberglass composites when compared to steering, and that shifting is a feasible automation process that may decrease the amount of variability and human labor required for large composite component manufacture [1],

3. Experimental methods

The intent of this project was to determine whether or not automating the shifting process was feasible, and might be useful for wind blade manufacturing. A machine was developed to deform, or shift, the fabric in-process as it is deposited in the mold. The machine is in the form of a small unit that attaches to an 8 m by 2 m programmable gantry. The job of the "shifting head" is to carry a roll of fabric, shift it into appropriate planar shapes for the mold, and eject the fabric. The shifting head was designed to work in tandem with the gantry so that as the fabric is ejected, the gantry will move appropriately to keep the fabric stationary as it is manipulated and distributed into the mold. The fabric used was Saertex 930 $^{g}/_{m^3}$ unidirectional fiberglass NCF. The solid model used in design and manufacture of the shifting head is shown in Figure 4, below.

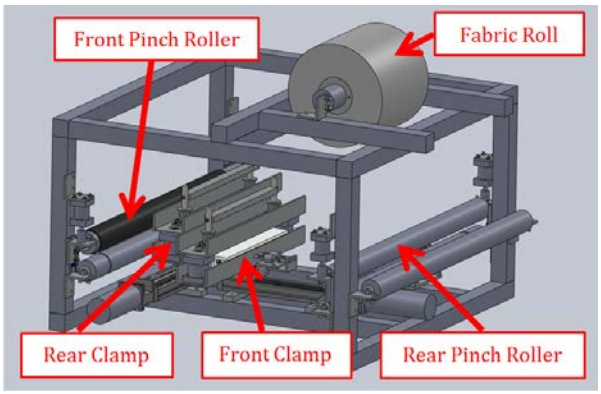

Figure 4: Shifting head solid model.

The shifting head was designed to be highly adjustable and adaptable. The machine has front and rear pinch rollers, as well as front and rear clamps. The machine starts with the fabric run through the pinch rollers and clamps, with a small section exiting the rear of the machine. The automated shifting process is shown in Figure 5, below.

In step 1, the front and rear pinch rollers begin in the open position while the front and rear clamps are grasping the fabric. In step 2, the front clamp moves a small distance, typically 0.05 inches, toward the front of the machine to tension the fabric between the clamps. The rear clamp then moves perpendicular to the length of the fabric as the front clamp moves toward the rear of the machine to complete one shift. In step 3, the clamps open as the pinch rollers close. The rollers then drive the fabric, ejecting some of it, and positioning it for another shift. This process can be repeated for the length of the roll. Varying the shift angle, as well as the distance between shifts can closely approximate a large variety of curves. The curvature of a shifted fabric sample is limited by the maximum angle the fabric will shift, referred to as the shear-lock limit. The shear-lock limit of the Saertex 930 $^{g}/_{m^3}$ unidirectional fiberglass NCF is approximately 25°.

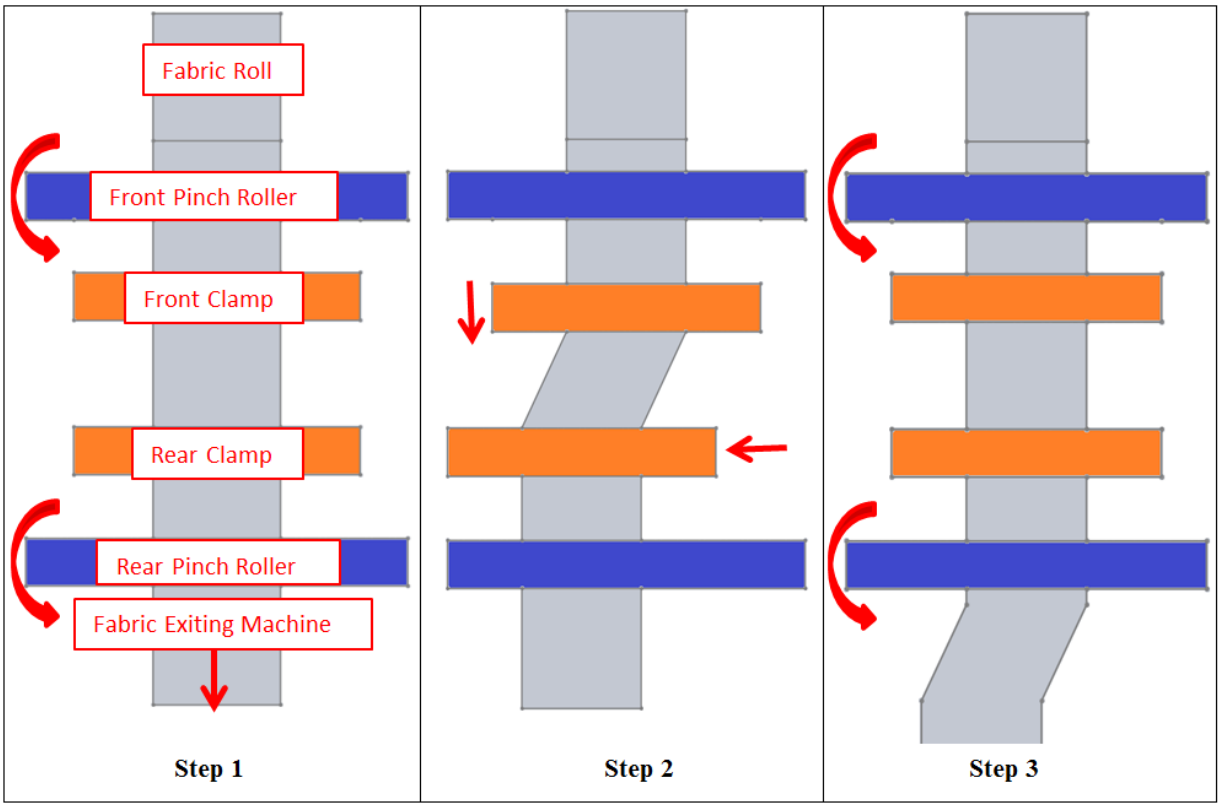

Figure 5: Schematic of automated fabric shifting machine.

In designing the machine, some preliminary work was done to predict the approximate clamping force required, the approximate fabric tension force required, and the clamp travel required to produce consistently shifted fabric samples. Figure 6, below, is an image of the shifting head components.

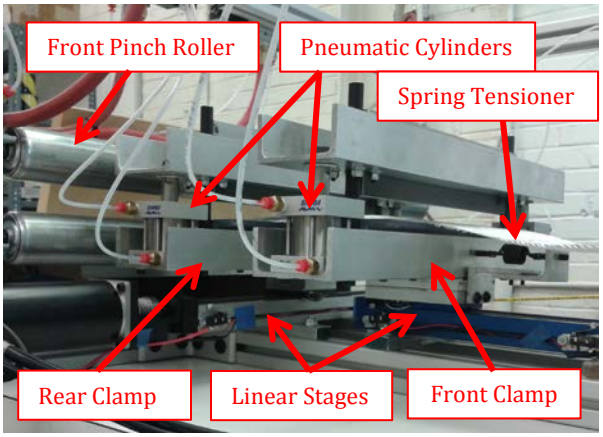

Figure 6: Shifting head components.

It was estimated that 620-N were required to adequately grasp the material in the clamps during the shifting process. The clamps are activated by small pneumatic cylinders and their clamping force is highly adjustable through pressure regulation. It was also estimated that the tensile force required to adequately and uniformly shift the fabric was 180-N. Each clamp is mounted on a linear stage, driven by a NEMA 23 motor. The stages are aligned to move the front clamp parallel to the fabric and the rear clamp perpendicular to the fabric. The front clamp was mounted on a spring loaded tensioning mechanism to adjust for the small amount of variability in the system. The distance the spring was deformed also indicated the amount of tension applied to the fabric.

In preliminary testing, the shifting head was stationary, with the fabric depositing onto a low friction surface. The low friction surface consisted of a converted air hockey table, in an effort to reduce the effects of friction as the shifted fabric is doled onto the surface, as shown in Figure 7, below.

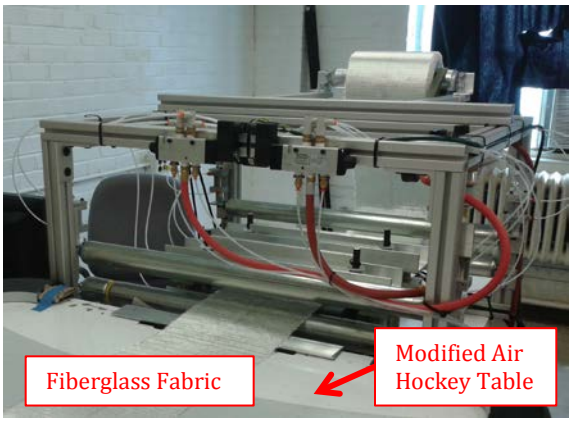

Figure 7: Shifting head stationary testing.

Samples produced by the machine were evaluated to answer the following questions:

1. Was the machine able to produce samples similar to that of Magnussen's shifting table?
2. Did the samples produced have negligible out-of-plane deformation, comparable to that of Magnussen?
3. How much spring-back occurred after the samples were deposited?

The primary goal of this project was to determine whether or not a machine could eject deformed fabric similar to that of the manual methods used in Magnussen's seminal work. The goal was to take an originally orthogonal, 200-mm wide, strip of Saertex 930 $^{g}/_{m^3}$ unidirectional fiberglass NCF and curve it 53°, with a curvature of 0.72 m^{-1}. This geometry is much more extreme than required for wind blade manufacture; such geometry shows the capability of the shifting method, as well as the capability of the automated shifting machine.

The secondary goal of the project was to determine whether or not the shifting head could produce in-plane shifted fabric samples without causing out-of-plane

deformation. Magnussen reported that when using the shifting method, the curvature of the fabric sample showed no correlation to out-of-plane deformation. Non-deformed samples were laser scanned and compared to shifted samples to quantify the amount of out-of-plane deformation induced by the shifting machine.

The final goal of the project was to determine how well the fabric keeps the shifted shape during the shifting process. The shift angle (degrees) of the fabric was measured at three points in the shifting process. The shift angle was measured by comparing the orientation of the number 1 tows to the number 2 tows. A shift angle of 0° indicates the fabric tows are orthogonal. Control measurements were recorded to assure the un-shifted fabric was, in fact, orthogonal. The un-shifted was found to be within ±1° of orthogonal.

To quantify the spring-back at the first stage of the shifting process, the shift angle was measured in the fully shifted position with the front and rear clamps grasping the fabric, as shown in Figure 8, below. The shift angle of the fabric clamped in the fully shifted position will be referred to as the "initial shift angle."

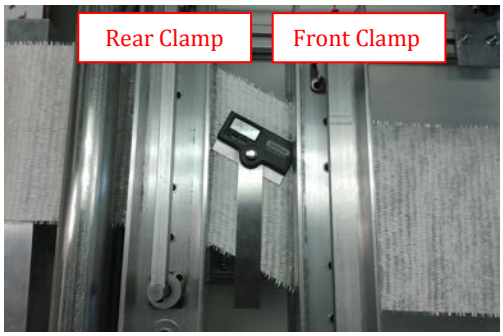

Figure 8: Measurement of initial shift angle.

Next, the clamps were released and the shift angle was measured again. The shift angle of the fabric after clamps were released will be referred to as "unclamped shift angle." The difference between the initial shift angle and unclamped shift angle will be referred to as "initial spring-back."

To quantify the spring-back induced by the rolling operation, the fabric sample was ejected from the machine and the shift angle was measured. The shift angle of the fabric after it was ejected from the machine will be referred to as "deposited shift angle." The difference between the unclamped shift angle and deposited shift angle will be referred to as "rolling spring-back." Figure 9, below, illustrates the measurement of the deposited shift angle.

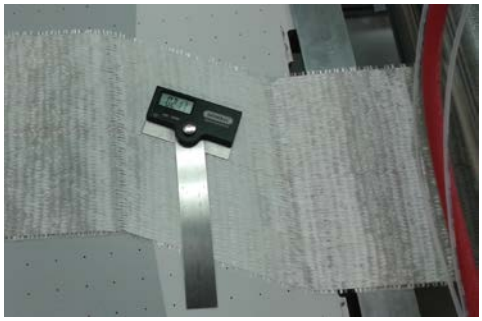

Figure 9: Measurement of deposited shift angle.

The difference between the initial shift angle and the deposited shift angle will be referred to as "total spring-back." The total spring-back is an additive function of the initial spring-back and the rolling spring-back.

The initial shift angle, unclamped shift angle, and deposited shift angle were measured at varying shift distances to investigate the effect of shift distance on spring-back severity. The shift distance is the fabric tow length between the clamp jaws. The shift distances investigated were 17.8 cm, 20.3 cm, 22.9 cm, 25.4 cm, and 27.9 cm. The nominal shift angle entered into the shifting head control program for each shift distance was 5°, 10°,15°, 20°, and 25°, for a total of 25 fabric samples.

4. Results

The primary goal of the shifting head was met by producing a fabric sample comparable to the sample manually produced by Magnussen. The shift parameters of Magnussen's fabric sample were evaluated, entered into the shifting head control program and the sample was produced, as shown in Figure 10, below.

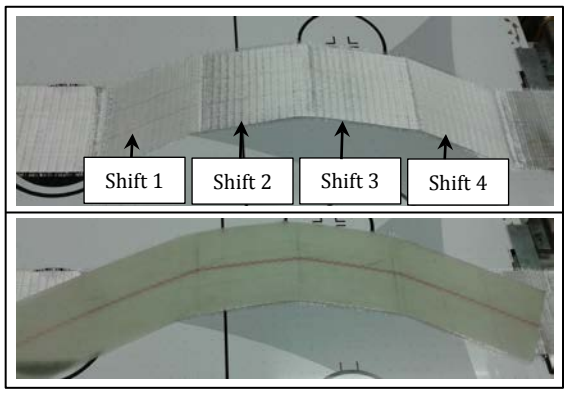

Figure 10: Deposited sample with an angle of 53° and a curvature of 0.72 m^{-1} (top) and Magnussen's manually shifted sample overlaid (bottom).

This example proves that the shifting head is capable of producing fabric samples with large angles and curvatures. The sample has an angle of 53°, with a curvature of 0.72 m^{-1}. The shift angle is defined as positive if the fabric was shifted in the counterclockwise direction in the orientation shown in Figure 10. Variation of the deposited shift and the ideal shift was observed, as shown in Table 1, below.

Table 1: Ideal shift angle compared to deposited shift angle for fabric sample with an angle of 53° and a curvature of 0.72 m^{-1}.

	Shift 1	Shift 2	Shift 3	Shift 4
Ideal Shift Angle (degrees)	26.50	8.50	-8.50	-26.50
Deposited Shift Angle (degrees)	28.45	11.80	-6.75	-24.95
Error in Deposited Sample (degrees)	1.95	3.30	1.75	1.55

For each shift, the observed shift angle was a larger value than the ideal shift angle. The shifts in the negative direction were decreased in magnitude, while the shifts in the positive direction were increased in magnitude. The net angle of the curved sample shown in Figure 9 was approximately 53°.

To evaluate the out-of-plane deformation of a shifted sample, the fabric was laser-scanned and compared to a virgin fabric sample. A best-fit plane was inserted into the 3D data, and the two samples were compared. An example of the scanned data of a virgin fabric sample is shown in Figure 11, below.

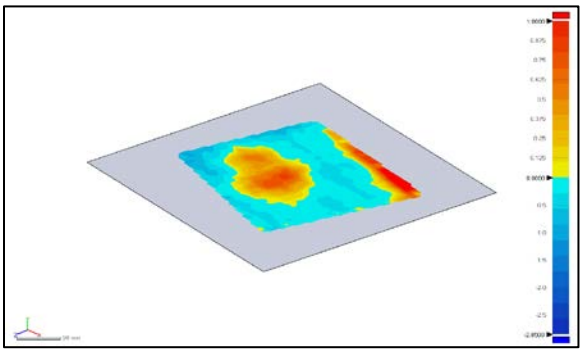

Figure 11: Laser scan data of virgin fabric sample with best-fit plane.

The standard deviation of the data points from the best-fit plane of the virgin fabric sample was 0.38 mm. The standard deviation of the data points from the best-fit plane of a 0.20 m shift distance by 10° shift angle fabric sample was 0.36 mm. This means that the standard deviation of the surface of the shifted sample decreased by 0.02 mm from that of the virgin fabric sample.

The results of the initial spring-back as a function of shift angle at five shift distances are shown in Figure 12, below. These data were obtained to understand the tendency of the fabric to spring back toward its initial orthogonal orientation after the machine clamps are released during a shifting operation.

Figure 12: Initial spring-back severity as a function of shift angle for five shift distances.

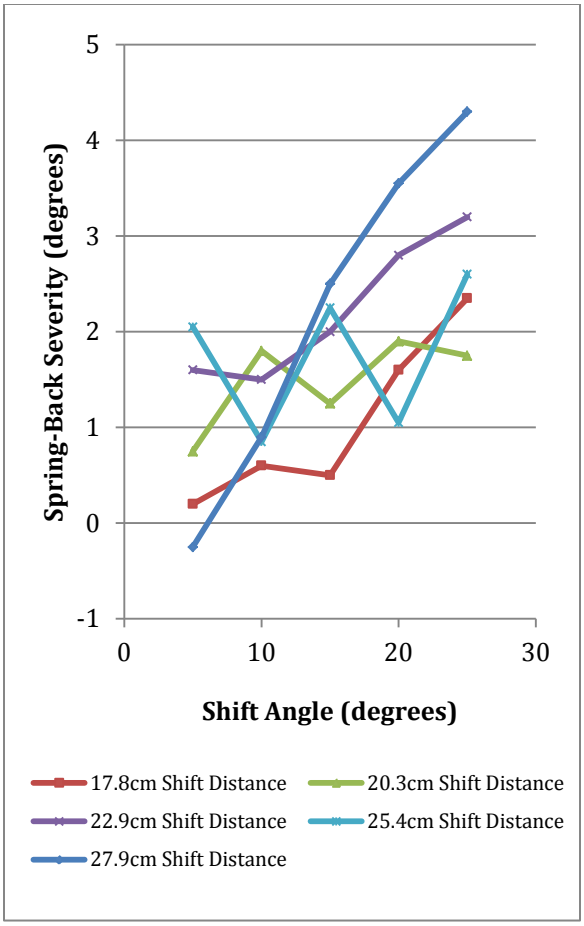

Figure 13: Rolling spring-back severity as a function of shift angle for five shift distances.

The data for initial spring-back severity as a function of shift angle is statistically inconclusive. Some qualitative trends can be observed, and investigated in future experiments.

To quantify the tendency of the fabric to continue to spring back toward its original orthogonal orientation during the rolling operation, the deposited shift angle was compared to the unclamped shift angle. The fabric rolling spring-back as a function of shift angle during fabric ejection is shown in Figure 13.

The data for rolling spring-back severity as a function of shift angle is statistically inconclusive, but trends can be observed and should be investigated in future experiments.

The total spring-back of the fabric was found by comparing the initial shift angle to the deposited shift angle. The total spring-back of the fabric is shown in Figure 14, below.

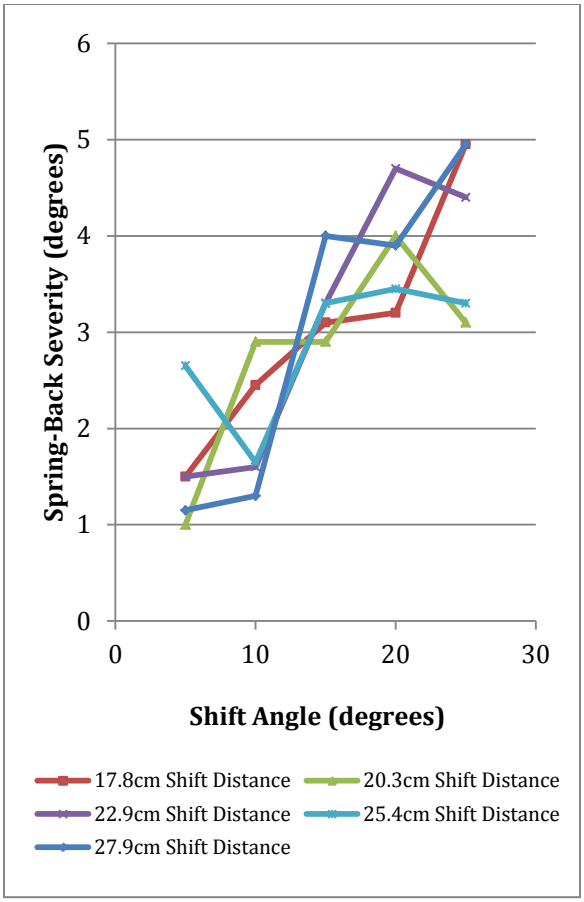

Figure 14: Total spring-back severity as a function of shift angle for five shift distances.

Although the data for total spring-back as a function of shift angle is not statistically conclusive, a qualitative trend is observable. It is evident that there is a relationship between shift angle and total spring-back.

5. Analysis and interpretation

The automated shifting machine was capable of producing a fabric sample with an angle of 53° and a curvature of 0.72 m^{-1}, which proves the machine's ability to produce fabric samples with a large curvature (small radius), and a large shift angle. In producing the sample, error in each shift angle was observed. The magnitude of the positive shift angles was increased, while the magnitude of the negative shifts was decreased. The effect was likely due to the friction between the air hockey table and the fiberglass fabric. As the fabric was ejected from the machine, the frictional force and the distance the fabric was shifted caused a moment in the plane of the fabric. This moment was in the positive (counterclockwise) direction, which translated into an increase in the shift angle in the fabric. In future experiments, the shifting head will be mounted on a programmable gantry that will allow it to move over the mold. This means the fabric will be stationary and the machine will be mobile, so fabric friction should not have this type of effect when the machine is used for its intended application.

The automated shifting machine can produce shifted fiberglass fabric samples without causing statistically significant out-of-plane deformation. The standard deviation of the surface of the shifted sample decreased by 0.02 mm from that of the virgin fabric sample. Considering the manufacturing tolerances in fiberglass fabric, the small inaccuracies of measuring equipment, and the variability of environmental factors, this data can conclude that the automated shifting head can produce shifted fabric samples with statistically negligible out-of-plane deformation.

Although the data for initial fabric spring-back were inconclusive, some qualitative trends can be observed. It appears that as the shift angle increases, so does the severity of fabric spring-back. As the shift angle increases, the number 1 tows are required to slide past each other an increasing distance, which translates into an increasingly observable tendency of the fabric to spring back toward its original orthogonal position.

It also appears that the shift distance has an effect on the tendency of the fabric to spring-back. As the shift distance increases, it appears that initial spring-back decreases.

In future work, a correlation between shift distance and spring-back severity, as well as and shift angle and spring-back severity may be derived, which could then be used set shift parameters for deforming the fabric before depositing it in a mold.

The data for rolling spring-back severity as a function of shift angle is not statistically conclusive, but a trend is present. It can be observed that as shift angle increases, rolling spring-back severity increases. This trend is likely due to the deformation the machine rollers induce on the fabric tows. As the fabric is compressed in the rollers and ejected from the machine, the deformation of the fabric tows may allow the tows to more easily slide past each other toward the initial orthogonal orientation.

Total spring-back is an additive function of both initial spring-back and rolling spring-back. Although the data are statistically inconclusive, it can be observed that total spring-back increases as shift angle increases. The combination of initial spring-back and rolling spring-back may be one of the most important observations of the fabric behavior as it is deformed and deposited by the machine. In future work, the correlation between fabric shift angle and total spring-back will be a critical relationship that will determine the magnitude of fabric deformation required within and automated shifting machine.

Further work is required to better understand the automated fiberglass fabric shifting process. Variables that can be fine-tuned and investigated include clamping force, fabric tension force, roller pinch force, roller alignment, frictional effects of fabric sliding through clamps, and spring-back tendencies throughout the shifting process. Further experimentation will reveal additional questions once the shifting head is used for its intended purpose, which is in conjunction with a programmable gantry.

6. Conclusions

The primary goal of this project was met by developing an automated shifting machine capable of producing fabric samples with geometry that is much more extreme than required for wind blade manufacturing. The machine was able to take an originally orthogonal, 200-mm wide, strip of Saertex 930 $^{g}/_{m^3}$ unidirectional fiberglass NCF and curve it 53°, with a curvature of 0.72 m^{-1}. This experiment shows that a machine can produce fabric samples with a large curvature (small radius), and a large shift angle. Future work with the shifting head may further develop the idea of automated shifting, as well as its applications in wind blade manufacturing.

The fiberglass fabric shifting method may be particularly useful for making fabric bend around curves in wind blade molds, without producing waves or wrinkles. Laser scanning was used to show that shifted fabric samples can be produced without out-of-plane deformation, through automated means. The data concluded that the automated shifting head can produce shifted fabric samples with statistically negligible out-of-plane deformation.

Although the data for fabric spring-back were statistically inconclusive, some qualitative trends can be observed and further investigated in future work. It appears that as the shift angle increases, so does the severity of initial spring-back, rolling spring-back, and total spring-back. Total spring-back, or the combination of initial spring back and rolling spring-back, may be one of the most important observations of the fabric behavior as it is deformed and deposited. A strong correlation between shift angle and fabric spring-back severity will be necessary for developing reliable and consistent fiberglass fabric shifting manufacturing methods for wind blades.

Acknowledgements

Support for this research was provided by a National Science Foundation Research Experience for Undergraduates site program in Wind Energy Science Engineering and Policy (WESEP) at Iowa State University.

References

C. J. Magnussen, “A fabric deformation methodology for the automation of fiber reinforced polymer composite manufacturing,” M.S. Thesis, Dept. Mech. Eng., Iowa State Univ., Ames, IA, 2011.

C. S. Yerramalli, T. Miebach, K. Chandraseker and S. C. Quek, "Fiber waviness induced strength knockdowns in composite materials used in wind turbine blades," GE-Global Research Center, Niskayuna

Fiberglass Woven Rocing 40oz 50" Width .035" Plain Weave. Digital image. Composite Envisions. 14 Aug. 2008. <http://compositeenvisions.com/raw-fabric-cloth-2/fiberglass-cloth-mat-roving-101/fiberglass-woven-roving-40oz-50-width-035-plain-weave-472.html>.

Kordi, Tarsha M., M. Husing, and B. Corves. "Development of a Multifunctional Robot End-Effector System for Automated Manufacture of Textile Preforms." Proc. of 2007 IEEE/ASME International Conference on Advanced Intelligent Mechatronics, AIM, Switzerland, Zurich. Piscataway, NJ: Institute of Electrical and Electronics Engineers, 2007. Print.

Mills, A. "Automation of Carbon Fibre Preform Manufacture for Affordable Aerospace Applications." *Composites Part A: Applied Science and Manufacturing* 32.7 (2001): 955-62. Print.

Hancock, S., and K. Potter. "The Use of Kinematic Drape Modelling to Inform the Hand Lay-up of Complex Composite Components Using Woven Reinforcements." *Composites Part A: Applied Science and Manufacturing* 37.3 (2006): 413-22. Print.

Robertson, R.E., T.-J. Chu, R.J. Gerard, J.-H. Kim, M. Park, H.-G. Kim, and R.C. Peterson. "Three-dimensional fiber reinforcement shapes obtainable from flat, bidirectional fabrics without wrinkling or cutting. Part 1. A single four-sided pyramid." Composites Part A: Applied Science and Manufacturing 31 (2000): 703-15.

Potter, K. "The influence of accurate stretch data for reinforcements on the production of complex structural mouldingsPart 1. Deformation of aligned sheets and fabrics." Composites 10 (1979): 161-67.

Sharma, S., and M. Sutcliffe. "A simplified finite element model for draping of woven material." Composites Part A: Applied Science and Manufacturing 35 (2004): 637-43.

Life Cycle Assessment of Taller Wind Turbines With Four Different Tower Designs

SARAH A. GUSTITUS
Wind Energy Science, Engineering and Policy REU
Iowa State University
Mentors: Dr. Sri Sritharan and Dr. Say Kee Ong

Abstract

Wind turbines are desirable as an alternative to power plants that use fossil fuels to generate electricity because wind turbines emit virtually no greenhouse gases during their operation. However, the production, construction and decommissioning of a wind turbine does produce a certain environmental impact, which can be quantified through a life cycle analysis (LCA) of the turbine. As the wind energy industry continues to grow, larger capacity turbines will be in higher demand, so that more energy can be produced for each turbine installed. One way to ensure greater energy production from turbines is to increase the height of the tower from today's typical 80 m (262 ft) hub height to a 100 m (328 ft) hub height to access higher velocity winds available at greater heights.

The production of the tower is known to be one of the largest sources of environmental impact during a turbine's life cycle. Because of the problems that arise when using steel to produce towers of this height, new tower are being designed. Full steel, full concrete, hybrid concrete-steel, and ultra high performance concrete (UHPC) towers are now being developed for 100 m (328 ft) hub heights. This paper uses LCA to assess these four 100 m (328 ft) tower designs to analyze how the use of different materials in the construction of taller towers affects the overall environmental impact involved in the lifecycle of a wind turbine. Two different LCA, one over 20 years, the other over 40 years, show that while the popular tubular steel tower design has the smallest environmental impact in the short term, the concrete tower design actually has a smaller environmental impact over the long term.

1. Introduction

In recent years wind energy has become a popular alternative energy source. The main attraction of wind energy is that it produces virtually no green house gas emissions during a turbines operation, unlike energy produced from burning fossil fuels such as coal or natural gas. Wind turbine technology is constantly being improved; one such improvement is the development of taller towers to access winds of higher speeds in order to increase the energy production from each turbine.

Although wind turbines emit no CO_2 while they are operating, CO_2 is emitted in the production of the turbines, transportation of the parts, maintenance on the turbines, and in the decommissioning process at the end of a turbine's life. This paper will assess the CO_2 emissions created over the lifetime of an individual wind turbine and compare those emissions to that of fossil fuel resources used to create the same amount of energy. This paper will analyze each stage in the life of a turbine to gain perspective on which stages produce the most emissions and examine the extent to which the turbine's production of clean, alternative energy negates these emissions. Also, since the tower of a turbine is a very energy intensive component, this paper will analyze differences in environmental impact created from four different types of 100 m tower designs: steel, hybrid, standard strength concrete, and ultra-high performance concrete (UHPC). Because of the

differences in lifespans of the different tower designs, each turbine will be assessed both over a 20-year period as well as a 40-year period. Through this information, it will become clearer where there is opportunity for the most improvement in the wind energy industry with respect to reducing environmental impact.

2. Literature review

Wind energy is becoming a preferred alternative to traditional energy sources provided through combustion of fossil fuels, in large part because a wind turbine produces no direct green house gas emissions during operation. However, the production, transportation, and de-commissioning of a wind turbine does create a measurable environmental impact. In order to quantify the environmental impact of a wind turbine, a Life Cycle Analysis (LCA) analyzing each stage of a turbine's life from cradle-to-grave must be carried out.

Previous studies on the environmental impact of wind turbines using LCA methodology have indicated that the manufacturing stage has the largest environmental impact of all of the stages of a turbine's life [1,2]. Within the manufacturing stage, the production of the tower is the most energy intensive process, and therefore has the most potential for green house gas emissions [1].

Taller towers are desirable for wind energy production because of their capability to accommodate higher capacity wind turbines. Furthermore, power is related to the cube, or the third power, of wind speed; therefore, if a turbine were to be placed high enough to reach winds 10% stronger than those located at current tower heights, that turbine would achieve about a 33% increase in available power [3]. Lastly, increased tower height will also increase the energy harvesting time due to the presence of steadier wind at higher elevations. However, when increasing tower height, there are several structural and economic factors that should be given consideration.

2.1 Steel Towers

The tower design most prominent in today's wind energy industry is the tubular steel tower. Steel is a desirable building material for towers because of its exceptional strength properties and ductility [4]. However, as tower heights approach 100 m (328 ft), steel towers become much more costly and the transportation of the parts becomes much more complex. Wider bases and thicker walls are required in higher towers in order to spread out the greater load and avoid buckling. However, a steel base with a diameter wider than about 4.4 m (14.4 ft) cannot be transported on land through conventional methods. This leads to much more costly and energy intensive transportation processes [5].

As steel sections become thicker, not only does the mere increase in quantity of material needed drive the price up, but steel fabrication issues also become more complex, and therefore more costly. The international market has also seen unprecedented rises in the cost of steel, making steel a less desirable material for tower construction [3,5].

2.2 Concrete Towers

One alternative to steel towers is concrete towers. While costs and complexities involved with steel towers increase exponentially with the height of the tower, according to LaNier, the converse is usually true for towers constructed using concrete [5]. Transportation logistics also are simpler for concrete. Much like steel towers, concrete towers are composed of several precast parts assembled on site to

make the whole tower; however, it is not necessary for the concrete tower parts to be monolithic, so smaller parts can be transported to the site and then post-tensioned together or be joined by suitable connections to make them act in a monolithic manner [4,5].

One disadvantage of using concrete is that a concrete tower would be much heavier than a steel tower of the same height. This means that a larger foundation would possibly be necessary, and more materials would have to be transported and used, adding to the cost and environmental impact of the project.

The decommissioning stage of a concrete tower's life is also different from that of a steel tower. Steel towers are typically designed to have about a 20-year lifetime before they must be decommissioned, at which point the steel is recycled. In contrast, concrete towers can have lifetimes of over 50 years. In this case, after 20-25 years the rotor blades, hub, cables, bearings, pitch control, cogs and hydraulics could be replaced using the same concrete tower. However, though the concrete tower has a longer lifetime, recycling options for this tower are limited, and the transport and processing of the resulting rubble is an energy-intensive process [6].

2.3 Hybrid Towers

Another tower design for taller turbines is the hybrid concrete-steel model. These hybrid towers consist of a concrete base with tubular steel sections placed on top of the base to reach the desired 100 m hub height. This design takes advantage of the economics and material strengths of both steel and concrete. The tubular steel sections of a hybrid tower would not be too wide for conventional transportation methods because the use of a concrete pedestal eliminates the need for a wider steel base. Also, the lighter hybrid tower would require a smaller foundation than the full concrete tower, and have less seismic weight [4,5].

LaNier [5] suggested that the construction of hybrid towers would also be less costly and time consuming than towers made of all steel or all concrete. Instead of using a large crane to install the nacelle at 100 m, a smaller crane could be used to perform the nacelle installation at the top of the steel section while it rests on the ground, after which the steel section could be jacked to the final 100 m hub height on top of the concrete pedestal [5].

However, as with the other designs, there are challenges with hybrid towers as well. Like with standard 80 m (262 ft) steel towers, steel tubular sections may need to be transported over long distances to the construction site. Also, using two different materials in such large quantities would require additional coordination for the contractor [4].

2.4 UHPC Towers

A fourth tower design currently under development at Iowa State University proposes using Ultra High Performance Concrete (UHPC).

2.4.1 Characteristics of UHPC

Research over the last few decades has led to the development of a new type of concrete known as UHPC, which is able to achieve higher strengths than standard concrete by eliminating typical defects in the microstructure of the concrete. While conventional concrete typically has an unconfined compressive strength of 3,000-6,000 psi (20-40 MPa), UHPC has a compressive strength of at least 21,700 psi (150 MPa), and can have compressive strengths approaching 30,000 psi (210

MPa). It also has low water content, internal fiber reinforcement and higher binder content. [4, 7-9]

The price per cubic yard of UHPC can be over ten times greater than the cost of conventional strength concrete. However, UHPC has many distinct advantages over regular concrete, such as “strength, ductility, flexibility and toughness, impact resistance, dimensional stability, durability increased useful life, impermeability, freeze/thaw resistance, corrosion resistance, abrasion resistance, aggressive environment resistance, and chemical resistance” according to the U.S. Department of Homeland Security [7]. Because of these advantages, structures built with UHPC can be constructed with a fraction of the volume of regular strength concrete that would be needed. A structure built with UHPC would also need less maintenance than a standard strength concrete counterpart. These advantages help make UHPC more cost effective when long term benefits are included [4, 7-9].

2.4.2 UHPC for Wind Turbine Towers

Towers built from UHPC would have the same benefits as regular strength concrete towers with respect to transportation coordination. Because UHPC towers could be built using segments that can be combined on site to act like a monolithic structure, the width of the base wouldn’t cause transportation challenges. In fact, many UHPC sections could be stacked on a single truck, which would further decrease the cost and environmental impact of transportation. In terms of distance for travel, UHPC is not as widely available as standard strength concrete, but local precasters could become certified to handle it if a viable UHPC tower design were presented to them. Also, material reductions would mean that a UHPC tower would be much lighter than a standard strength concrete tower, so that the lighter pieces could be lifted using small capacity cranes [4].

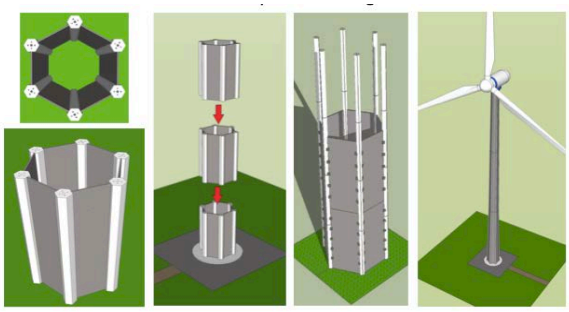

Figure 1: UHPC tower design

3. Experimental methods

3.1 Life Cycle Analysis

The Life Cycle Analysis (LCA) was used to assess each stage of the life of the wind turbine. The life of the wind turbine was broken down into the following stages: manufacture, transportation and erection, operation and maintenance, and decommissioning.

Two LCA were performed. One was for 20 years, the typical lifespan of a wind turbine. The second was for 40 years with a total replacement of the nacelles and rotors for each turbine after 20 years. Due to the durability of concrete tower components, the concrete tower, UHPC tower and the concrete base of the hybrid tower will remain in place to be fitted with the new turbine components. It was assumed that an entirely new steel tower, including foundation must be built for the latter half of the 40 years since steel towers are only expected to last 20-25 years.

3.1.1 Breakdown of the Life Cycle
Manufacturing Stage

The manufacturing stage includes the production of all parts of the wind turbine. The parts assessed are as follows:

- Rotor & Nacelle, not including the blades: the steel nacelle casing as well as the gearbox, generator, transformers and electronics, hub, and nose cone
- Blades
- (3)
- Tower
- Foundation
- Grid connection (materials such as cables and labor)

Table 1. Materials used in each tower design

	Concrete Tower	Hybrid Tower	Steel Tower	UHPC Tower
Steel, metric tons	----	160.8	335.2	----
Reinforcing Steel, metric tons	62.5	127.4	----	38.0
Standard Strength Concrete, metric tons	1924.6	1634.3	----	----
High Strength Concrete, metric tons	----	----	----	560.3
Ultra High Performance Concrete, metric tons	----	----	----	142.4

Table 2. Materials used in turbine components

Component	**Weight**	**Materials Breakdown**
Nacelle		
Bedplate/frame	13 t	13 t – steel
Cover	9.33 t	9.33 t – steel
Generator	7.14 t	5.71 t – steel
		1.43 t – copper
Brake System	1.02 t	1.02 t – steel
Gearbox	24.06 t	23.58 t – steel
		0.241 t – copper
		0.241 t – aluminum
Cables	1.63 t	0.69 t – aluminum
		0.94 t – copper
Revolving System	3.87 t	3.87 t – steel
Crane	1.02 t	1.02 t – steel
Transformers /sensors	6.93 t	3.47 t – steel
		1.38 t – copper
		1.38 t – aluminum
		0.7 t - plastic
Rotor		
Hub	19.2 t	19.2 t – steel
Blades	20.07 t	12.04 t – fibre glass
		8.03 t - epoxy
Bolts	0.73 t	0.73 t - steel

Transportation and Construction Stage

In this stage, the transportation of the parts of the turbine, as well as the transportation of crane used to erect each turbine will be considered. For simplicity, it will be assumed that when freight trucks are used, they can use a direct path without having to completely avoid any bridges or roadways unless otherwise noted. Transportation will be quantified in the units of km, the unit of the transport of 1000 kilograms of material over 1 km.

Operation and Maintenance Stage

This stage will assess the operation and maintenance involved in the entirety of each turbine's life. This will include transportation needed for technicians to visit each turbine for regular maintenance, as well as predicted replacement of turbine components.
In this stage, the transportation of the parts of the turbine, as well as the transportation of crane used to erect each turbine will be considered. For simplicity, it will be assumed that when freight trucks are used, they can use a direct path without having to completely avoid any bridges or roadways unless otherwise noted. Transportation will be quantified in the units of km, the unit of the transport of 1000 kilograms of material over 1 km.

Operation and Maintenance Stage

This stage will assess the operation and maintenance involved in the entirety of each turbine's life. This will include transportation needed for technicians to visit each turbine for regular maintenance, as well as predicted replacement of turbine components.

Decommissioning Stage

This stage will consider the disposal of materials at the end of the tower's life. Some materials will be sent to a landfill or incinerated, and others will be recycled for use in other products.

3.1.2 Environmental Impact

This LCA will determine the environmental effect of each wind turbine through the Eco-Indicator99 method. The environmental effects will be broken down into the following categories: carcinogens, organic respiration, inorganic respiration, climate change, radiation, ozone layer depletion, ecotoxicity, acidification and eutrophication, land use, minerals and fossil fuels.

3.2 Software/Database(s) used

This environmental analysis was performed using the SimaPro 7.3 software by Pré Consultants. Once information on the materials, processes and transportation involved in producing the turbine is input, the system is able to break down the environmental effects of each stage into the eleven categories listed in section 3 .1.2. Various versions of SimaPro software have been used in other professional wind turbine LCA [2, 10].

3.3 Assumptions and Limitations

For the purpose of this analysis, it will be assumed that each style of tower will host the same capacity turbine with the same rotor, nacelle, and grid connection cables. A 3 MW turbine will be used in this analysis. A capacity factor of 37.6% will be used to estimate the energy produced over the life of the wind turbine, which is assumed to be 20 years (though the lifetime of each tower differs). Any paint used on the tower is considered to have a negligible effect on the final environmental impact, and is therefore not included in the analysis.

The tower design will differ for each turbine. The design specifications for the UHPC tower will be based on the most updated design available at the time that this paper is written (July 2012). Though the towers each have different weights, the same foundation will be used for each because of other factors that could significantly influence the size of the foundation needed; it will be assumed that the foundation will

consist of 475 m^3 of concrete and 36 tons of reinforcing steel [11].

For maintenance, it will be assumed that each turbine will require one replacement generator over the course of its 20-year lifetime. Also, technicians must inspect the each turbine twice a year, leading to 900 km of travel by car per year, per turbine [11].

The decommissioning stage will only consider the best possible recycling scenario, where as many components as possible are recycled or refurbished for reuse in the most efficient ways possible.

4. Results

The turbine with the steel tower has the smallest overall environmental impact in the short term LCA covering 20 years, followed by the turbine with the hybrid tower. This is largely due to the high efficiency of recycling steel compared to the low efficiency of recycling concrete. When looked at over 40 years, the turbine with the concrete tower has the smallest overall environmental impact, and is also followed by the turbine with the hybrid tower. The durability of the concrete tower (or concrete tower base in the case of the hybrid tower) is the reason for these turbines having a smaller long term impact than the steel tower.

In both scenarios, the turbine with the UHPC tower has the largest overall impact, though in the long term the difference in impacts between this turbine and its counterparts becomes significantly smaller. The main reason for the large difference between the impact of the UHPC tower and the standard strength concrete tower is that the production of UHPC requires almost twice the energy of the production of an equal amount of standard strength concrete due to a larger amount of cement used in UHPC [12].

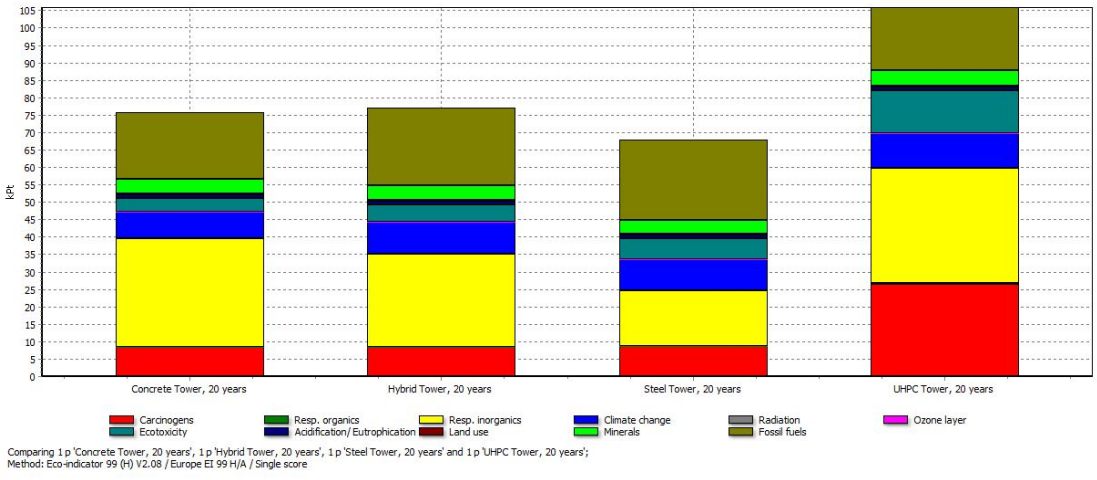

Figure 2: Single score comparison of the four towers over 20 years. Analysis method: EcoIndicator99. Results given in kilo-ecopoints.

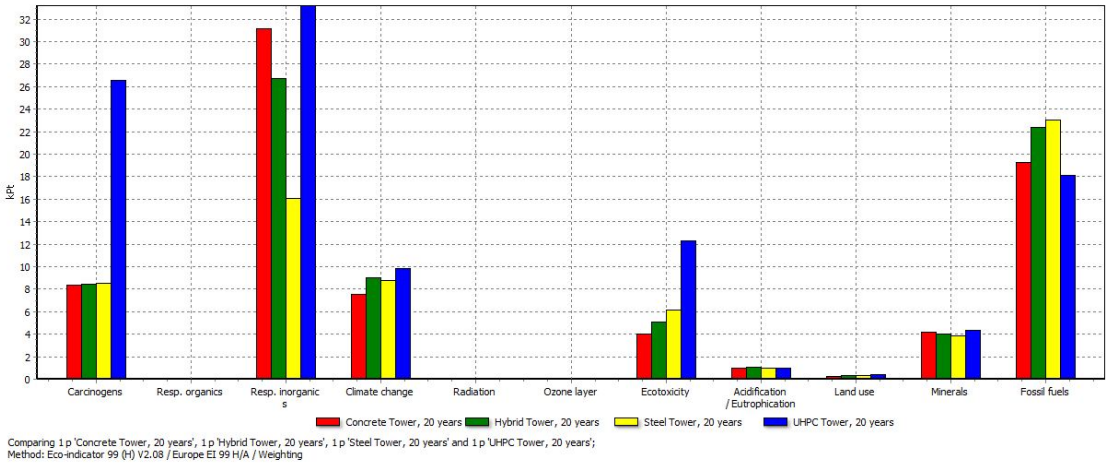

Figure 3: Weighted comparison of all four turbines over 20 years. Analysis method: EcoIndicator99. Results given in kilo-ecopoints (kpt).

4.1 LCA over 20 years

In each turbine all of the components with the exception of the towers were identical. The nacelle and rotor (not including the blades) had the largest contribution to the overall score of each turbine. The blades and foundation had the same overall impact score, which was just over a third of the impact of the nacelle and rotor; however, the scores differed in each individual impact category.

The manufacturing stage had the largest impact in each turbine, followed by transportation, and then maintenance. In every turbine, manufacturing accounted for at least half of the total environmental impact. Transportation had the largest effect in the case of the concrete tower, comprising of approximately 45% of the total impact of the tower alone. In comparison, the transportation of the nacelle and rotor components comprised of less than 1% of their total environmental impact; transportation accounted for approximately 20% of the impact of the foundation. Maintenance accounted for 4-5% of each tower's impact.

The decommissioning phase had a very different impact on each turbine depending on the type of tower. This phase had a positive effect on the turbines with the steel and hybrid towers, while it had a negative effect on the turbines with the concrete and UHPC towers. Before considering the decommissioning phase the turbine with the steel tower has the largest overall environmental impact; afterwards, the decommissioning phase eliminates 18% of the impact caused by the other stages, making this turbine the most environmentally sustainable of the four turbines analyzed. The decommissioning phase had the largest negative effect on the turbine with the UHPC tower, where this phase increased the overall impact by 34%, making it the least sustainable turbine whereas it is the second most sustainable turbine before this phase is considered. However, it must be remembered that it is highly unlikely that the UHPC tower or concrete tower would be decommissioned after 20 years due to their durability; the lifespan of the UHPC tower is expected to be higher than 40 years even, giving it the potential to last through three total nacelle and rotor replacements without requiring a new tower.

4.2 LCA over 40 years

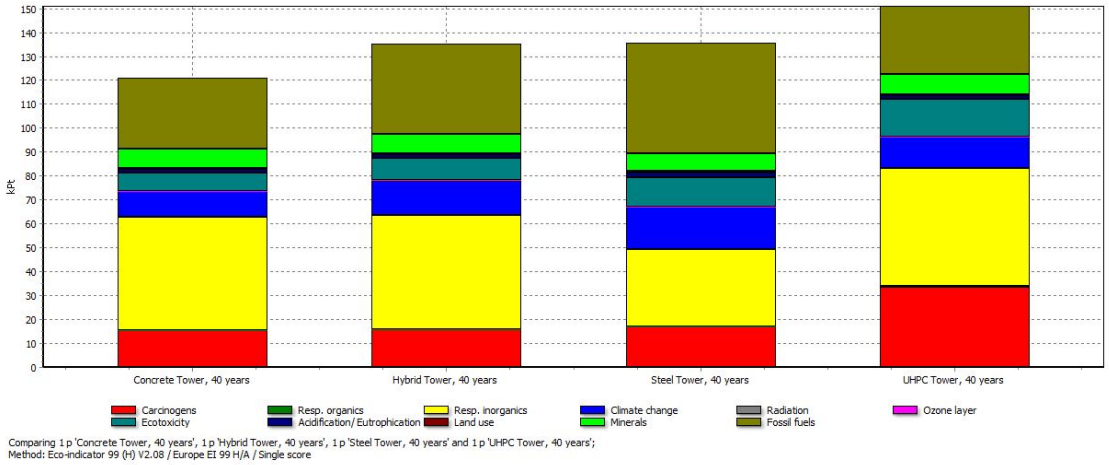

Figure 4: Single score comparison of all four towers over 40 years. Analysis method: EcoIndicator99. Results given in kilo-ecopoints (kpt).

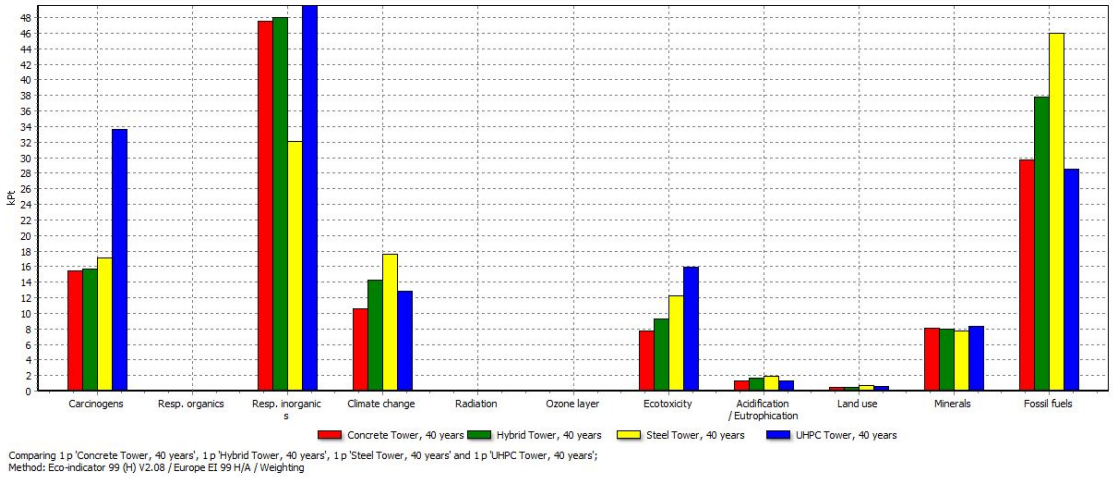

Figure 5: Weighted comparison of all four turbines. Analysis method: Ecoindicator99. Results given in kilo-ecopoints (kpt).

Over 40 years the concrete tower has the smallest overall impact, followed by the hybrid tower, the steel tower, and then the UHPC tower. The impact of the turbine with the steel tower doubles because every turbine component must be new, including the tower and foundation. The impact of the hybrid tower increases by 75% of the original 20-year impact because while the concrete tower base and the foundation remain in place, the steel tower top and the nacelle and rotor, including the blades, must be replaced. However, the turbines with the concrete and UHPC towers only need the replacement of the nacelle and rotor, including the blades, resulting in their impacts increasing by 60% and 42% of their original scores, respectively.

5. Analysis and interpretation

Though each tower does produce a quantifiable environmental impact, this impact still pales in comparison when looked at next to energy produced from burning fossil fuels. The ability of wind

turbines to produce energy without emissions during their operation means that turbines can pay back their environmental impact relatively quickly.

It is assumed based on the 37.6% capacity factor that each turbine will be able to produce approximately 9.881 GWh per year. Assuming that the clean energy produced from a wind turbine were to exclusively displace energy produced from coal, an overall impact of 580,000 ecopoints per year would be avoided; deducting the impact created over the life of a turbine, this means that a total impact of 11,500,000 ecopoints is prevented over the 20 year lifespan. If energy from natural gas were exclusively displaced instead, an impact of 653,000 ecopoints per year (mainly in consumption of fossil fuels) would be avoided, or an impact of 13,000,000 over 20 years after deducting the impact of the turbine.

Payback times for each turbine's impact can be found by finding the percent of the turbines' 20-year lifetime that it would take for impact avoided to equal the impact generated over the turbine's life. These payback times differ depending on what energy source the impact avoided is from. Each turbine can pay back its impact in a majority of the impact categories in less than a year. When compared to energy produced by coal, the turbines each payback their impacts in every category within their 20-year life span. However, when compared to energy produced from natural gas, it would take significantly longer than this life span to payback the impact on mineral consumption, though every other category is paid back within the 20 years. The payback times for each category are broken down in tables 1 and 2.

Table 3. Payback times for each turbine compared to energy produced from coal. Results given in days

	Concrete (days)	Hybrid (days)	Steel (days)	UHPC (days)
Carcinogens	23.7	24.1	24.3	75.9
Resp. Organics	101.3	106.9	102.6	131.6
Resp. Inorganics	44.3	37.9	22.9	47.2
Climate Change	24.6	29.4	28.7	32.0
Radiation	277.6	266.2	239.6	313.4
Ozone Layer	162.4	152.7	122.3	161.5
Ecotoxicity	163.3	206.2	250.7	502.2
Acidification/Eutrophication	24.7	27.2	23.9	25.7
Land Use	13.3	14.7	16.0	18.7
Minerals	1831.6 (5.0 years)	1766.0 (4.8 years)	1678.6 (4.6 years)	1914.6 (5.2 years)
Fossil Fuels	137.4	160.3	164.6	129.5

Table 4. Payback times for each turbine compared to energy produced from natural gas. Results given in days.

	Concrete (days)	Hybrid (days)	Steel (days)	UHPC (days)
Carcinogens	321.3	326.8	329.5	1027.4
Resp. Organics	33.4	35.2	33.8	43.3
Resp. Inorganics	70.7	60.5	36.5	75.3
Climate Change	43.3	51.8	50.5	56.3
Radiation	913.1	875.5	788.2	1030.7
Ozone Layer	2970.1 (8.1 years)	2791.2 (7.6 years)	2236.5 (6.1 years)	2952.2 (8.1 years)
Ecotoxicity	3935.3 (10.8 years)	4968.3 (13.6 years)	6040.7 (16.5 years)	12101.1 (33.2 years)
Acidification/Eutrophication	63.3	69.8	61.4	65.9
Land Use	746.1	826.6	899.1	1049.4
Minerals	19069.2 (52.2 years)	18386.5 (50.3 years)	17476.3 (47.9 years)	19933.9 (54.6 years)
Fossil Fuels	17.0	19.8	20.3	16.0

6. Conclusions

From this study we can see that though the recycling of steel makes the steel tower design the most environmentally friendly design over 20 years, when considering the long term future of an individual wind turbine or an entire wind farm the concrete tower will have the lowest overall impact. According to LaNier, when comparing a steel tower, hybrid tower, and concrete tower, a cast-in-place concrete tower is the most economically sound option [5]. With this taken into consideration, the constructing a turbine with a concrete tower seems to be the clear choice.

Both LCA suggest that the turbine with the UHPC tower has the largest environmental impact; however, the UHPC tower should not be dismissed as a nonviable tower option. UHPC has only been developed in recent decades, and so it is possible that as research continues on this type of concrete that the production process may become less energy intensive. More importantly, the exact lifetime of the UHPC has not yet been determined, but it is expected to be longer than 40 years. If the UHPC tower and concrete tower are able to be fitted with three nacelle and rotor replacements over 60 years instead of two replacements over 40 years, then the turbine with the steel tower would become the option with the largest environmental impact over that period of time. Also, over this longer time span the turbine with the UHPC tower has only a very slightly larger impact than that of the turbine with the hybrid tower; the turbine with the concrete tower retains the smallest environmental impact by a significant amount (see Fig. 5).

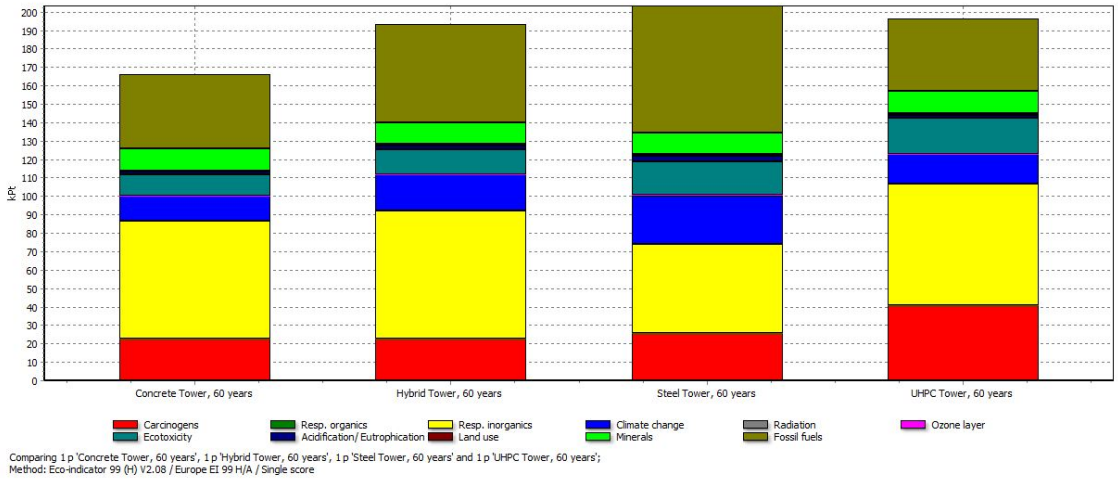

Figure 6: Projected LCA over 60 years, assuming a lifespan of 60 years for all concrete tower components. Analysis method: EcoIndicator99. Results given in kilo-ecopoints (kpt).

Overall it can be noted from this LCA that there is an undeniable environmental benefit from installing wind turbines, no matter what tower design is used. Further research into the lifespan of concrete tower components must be done before it can be definitively determined whether or not a UHPC tower is more environmentally friendly than a steel tower over the span of 60 years; however, assuming that concrete towers will last at least 40 years, it can be determined from this LCA that a tower composed completely of standard strength concrete is the most feasible option over that length of time, followed by the hybrid tower design.

Appendix A – 20 Year LCA Scores, given in ecopoints

	Concrete	Hybrid	Steel	UHPC
Carcinogens	8.32E3	8.46E3	8.53E3	2.66E4
Resp. Organics	23.4	24.7	23.7	30.4
Resp. Inorganics	3.12E4	2.67E4	1.61E4	3.32E4
Climate Change	7.54E3	9.03E3	8.8E3	9.81E3
Radiation	75.3	72.2	65	85
Ozone Layer	1.66	1.56	1.25	1.65
Ecotoxicity	4E3	5.05E3	6.14E3	1.23E4
Acidification/Eutrophication	980	1.08E3	950	1.02E3
Land Use	278	308	335	391
Minerals	4.19E3	4.04E3	3.84E3	4.38E3
Fossil Fuels	1.92E4	2.24E4	2.3E4	1.81E4
TOTAL	**7.58E4**	**7.71E4**	**6.78E4**	**1.06E5**

Appendix B – 40 Year LCA Scores, given in ecopoints

	Concrete	Hybrid	Steel	UHPC
Carcinogens	1.54E4	1.56E4	1.71E4	3.37E4
Resp. Organics	37.3	41.8	47.3	44.3
Resp. Inorganics	4.75E4	4.8E4	3.21E4	4.96E4
Climate Change	1.06E4	1.43E4	1.76E4	1.29E4
Radiation	121	118	130	131
Ozone Layer	2.77	2.67	2.5	2.76
Ecotoxicity	7.67E3	9.27E3	1.23E4	1.59E4
Acidification/Eutrophication	1.32E3	1.66E3	1.9E3	1.36E3
Land Use	469	499	670	583
Minerals	8.08E3	7.92E3	7.68E3	8.27E3
Fossil Fuels	2.97E4	3.78E4	4.6E4	2.86E4
TOTAL	**1.21E5**	**1.35E5**	**1.36E5**	**1.51E5**

Acknowledgements

Support for this research was provided by a National Science Foundation Research Experience for Undergraduates site program in Wind Energy Science Engineering and Policy (WESEP) at Iowa State University.

References

Guezuraga, B., Zauner, R., and Pölz, W., 2011, "Life cycle assessment of two different 2 MW class wind turbines," Renweable Energy, **37**, pp. 37-34

Martinez, E., Sanz, F., Pellegrini, S., Jimenez, E., and Blanco, J., 2009, "Life cycle assessment of a multi-megawatt wind turbine," Renewable Energy: An International Journal, **34**, pp. 667-73

DOE (U.S. Department of Energy), 2008, "20% Wind Energy By 2030," DOE/GO-102008-2567, Washington, DC

Lewin, T., Sritharan, S., 2010, “Design of 328-ft (100-m) Tall Wind Turbine Towers Using UHPC,” Iowa State University, Ames, IA

LaNier, M.W., 2005, “LWST Phase I Project Conceptual Design Study: Evaluation of Design and Construction Approaches for Economical Hybrid Steel/Concrete Wind Turbine Towers,” NREL Paper No. SR-500-36777, National Renewable Energy Laboratory, Golden, CO.

Lenzen, M., Munksgaard, J., 2001. “Energy and CO2 life-cycle analyses of wind turbines—review and applications,” Renewable Energy, **26**, pp. 339-62

Department of Homeland Security, 2011, “Ultra High Performance Concrete, Pathway to Commercialization,” http://www.dhs.gov/xlibrary/assets/uhpc-pathway-to-commercialization.pdf

Graybeal, B.A., 2006, “Material Property Characterization of Ultra-High Performance Concrete,” FHWA-HRT-06-103, PSI, Inc., Fairfax, VA

Vande Voort, T., Suleiman, M., Sritharan, S., 2008, “Design and Performance Verification of UHPC Piles for Deep Foundations,” IHRB Project TR-558, Center for Transportation Research and Education, Iowa State University, Ames, IA

Crawford, R.H., 2009, “Life cycle energy and greenhouse emissions analysis of wind turbines and the effect of size on energy yield,” Renewable and Sustainable Energy Reviews, **13**, pp. 2653-60

Vestas Wind Systems, 2006, “Life Cycle Assessment of offshore and onshore sited wind power plants based on Vestas V90-3.0 MW turbines.,” Aarhus N, Denmark.

Sritharan, S., 2009, “Use of UHPC for Sustainable Bridges in Seismic Regions,” *Proceedings of the 2009 US – Korea Conference on Science, Technology and Entrepreneurship*, Korean-American Scientists and Engineers Association, Raleigh, NC, 2009.

Analysis of Ramp Events and Two-Day WRF Wind Forecast Accuracy at 80 m

RENEE A. SHOWERS WALTON
Wind Energy Science Engineering and Policy REU, Iowa State University, Ames, Iowa
Mentor: William Gallus, Jr.

Abstract

Ramp events were studied at an 80-m meteorological tower in Pomeroy, IA from 29 May 2008 to 12 November 2009 and 26 June 2010-8 September 2010 and from nacelle data at six 80-m wind turbines in central Iowa from 26 June-8 September 2010 and 28 June-16 August 2011 in order to understand the causes and behavior of the ramps. The two sites are approximately 100 miles apart. A ramp event was defined as a 3 m s^{-1} change in wind speed in 4 hr or less. This is equivalent to a change in power output of 50% or more of total capacity. We observed 834 ramps in the Pomeroy data and 1324 ramps in the central Iowa data among the six turbines. This study found that forty percent of ramps in central Iowa occurred within 6 hr of ramps in Pomeroy, IA. Twenty percent of ramps occurred simultaneously. In Pomeroy, most ramps were attributed to storms or a strong pressure gradient. A two-day persistence forecast was also performed for each turbine and at the Pomeroy station. Hit rates were measured around 40% for each site. False alarm rate and threat score were also calculated.

1. Introduction

This study analyzed ramp events observed at an 80-m meteorological tower in Pomeroy, IA from 29 May 2008 to 12 November 2009 and 26 June 2010-8 September 2010 and from six 80-m wind turbines in central Iowa from 26 June-8 September 2010 and 28 June-16 August 2011. A ramp event was defined as a "change in wind power [of] 50% or more of total capacity in either 4 or 2 hr or less". The change in power in relation to capacity was determined by the power curve. This study analyzed atmospheric phenomena to determine the cause of ramp events at both locations. In cases where data from Pomeroy and central Iowa overlap, ramps were evaluated to determine whether any correlation existed between ramps at the two locations. Ramps in Pomeroy were attributed to storms and strong pressure gradients. It was determined that 40% of ramps in central Iowa occur within 6 hr of ramps in Pomeroy, IA.

2. Literature review

Ramp events make wind energy an unpredictable resource with sudden changes from optimal generation speeds to the cut-off range. With the U.S. Department of Energy's scenario of 20% of all electrical energy coming from wind by 2030 (Department of Energy 2008), uncertainty in power output drives wind farms to increase efficiency through better forecasts; however, few climatologies of ramp events exist, and the best forecasting method has yet to be discovered. Studies have shown that there are multiple causes of ramp events. Freedman et al (2008) used surface meteorological charts from the National Climatic Data Center (NCDC), wind profilers from the National Oceanic and Atmospheric Administration (NOAA), sounding data from the National Weather Service (NWS), NWS high-resolution Automated Surface Stations (ASOS) data, and archived Next-Generation Radar (NEXRAD) Weather Surveillance Radar 88 Doppler (WSR-88D) level II data, all

concurrent with the ramp event, to determine the meteorological cause. Ramp-ups are most often caused by nearby convection, followed by the passage of fronts, and finally low level jets. Ramp-downs are caused by a sudden decrease in pressure gradient (Freedman et al., 2008; Zack, 2008). Since ramps can be caused by different and small scale meteorological phenomena, they are very difficult to forecast.

Furthermore, lack of a formal definition for a ramp (Ferriera et al., 2010) makes forecasting such events difficult. One of the most commonly used definitions at this time is that a ramp event is a change in wind farm power output of 50% or more of installed capacity in 4 hr or less (Greaves et al., 2009). We adopt this definition for our study. Most forecasters use a single WRF PBL scheme to predict wind speed. While a Midwest study found six PBL schemes underestimated ramp events when used separately, it also discovered that using an ensemble of WRF PBL schemes provided a more accurate forecast for 80 m winds (Deppe et al., 2012). This was also observed in the study by Greaves et al (2009) who used several combinations of numerical weather prediction (NWP) models and found that combining different NWPs was always more accurate than using one NWP source (Ferreira 2010). Current NWP ramp forecasts are not very accurate temporally or spatially. Ferreira et al. (2010) provides a contingency table (Table 1) to help determine the accuracy of a forecast.

In Australia, the Wind Power Prediction Tool (WPPT) forecasts power output for the Woolnorth Bluff Point wind farm by combining real-time wind power observations with wind speed and direction forecasts from MesoLAPS, the Australian Bureau of Meteorology NWP (Cutler et al., 2007). This forecasting tool creates hourly forecasts of the wind farm power output. Cutler et al. (2007) demonstrated the accuracy of the WPPT by calculating its root mean squared error (RMSE) and comparing it to that of other models. At the site studied, climatology gave an RMSE of 35%, a 36-hr persistence forecast gave an RMSE of 50%, and the WPPT forecast at 36 hr gave an RMSE of 25%. This shows that significant improvements in wind forecasting are occurring, but there is still work to be done. As Francis et al. (2008) suggests, the solution may be to use NWPs in conjunction with upstream meteorological data. Or, if probabilistic forecasts are preferred, radar with pattern recognition could be used along with warnings from the NWS (Francis et al 2008).

Similar to the suggestions of Francis et al (2008), Linden et al (2012) focuses on using upstream observations to predict ramp events for Xcel wind turbines. Xcel uses WRF and MM5 ensemble forecasts that include Dynamic Integrated ForeCast (DICast), which was designed to be comparable to the human forecast process, as its operational forecast. All WRF and MM5 schemes used are originally run separately then a consensus is generated. This process has been proven to significantly reduce error in day-ahead wind-power forecasts (Myers et al. 2011); however, while it excels for events caused by large scale synoptic processes, even though timing is problematic, this process lacks skill in predicting ramps associated with mesoscale features. Therefore, Linden et al. (2012) created an algorithm that uses available upstream observations. They configured this algorithm for a wind farm in Colorado where they created rings of observation points surrounding the wind farm with 50 km between rings to approximate the distance for meteorological features to travel in 1-hr. With these eight rings, they created hourly forecasts. To forecast the wind 1 hr out they would use

rings one through eight, a 2-hr lead time would use rings two through eight and so on. Since this study used the surface wind speed observations to make turbine height forecasts, they multiplied the observed speed by 1.36 to estimate the 80 m wind. This method proved successful for forecasting ramp events associated with cold fronts and pressure gradient changes; however, it did not do well with ramps associated with convective events (Linden et al., 2012). As noted, more needs to be understood about their behavior for consistent skillful forecasts.

Ramp events in a West Texas study were observed to be most frequent in spring and summer in conjunction with convection (Freedman et al 2008). However, the Pomeroy, IA study (Deppe et al., 2012) found a bi-modal distribution with peaks in frequency in December and June, with minima in February and August. In winter months, the majority of ramp up events took 4 hr, but in the summer they took place in half the time due to the convective state of the atmosphere (Deppe et al., 2012). The difference in frequencies could be due to contrasting definitions of a ramp event or meteorological differences between locations of studies. Ramp-ups most often occur from 0000—0300 UTC (1800—2100 LST) as the surface layer decouples from the overlying atmosphere and the low level jet (LLJ) forms (Deppe et al., 2012). Ramp-ups in the West Texas study were also found to follow this pattern, peaking at 0100 UTC (1900 LST) (Freedman et al., 2008). Ramp-downs were not found to have a distinct pattern in the West Texas study; however, in the Pomeroy study they were found to peak from 1200—1500 UTC (0600—0900 LST). Around this time, the surface begins to warm and the LLJ ends.

3. **Experimental methods**

This study re-evaluates the ramp events from Deppe et al. (2012) and combines them with 2010 and 2011 wind speed data from a central Iowa wind farm. The central Iowa data were taken every 10 min and underwent extensive quality control. After excluding erroneous data classified by periods when the wind speed suddenly dropped to zero, any change in wind speed larger than 3 m s^{-1} in 4 hr or less, as in Deppe et al. (2012), was considered a ramp. After all ramp-ups and ramp-downs were identified, possible meteorological causes were sought for the Pomeroy, IA and central Iowa ramp events. We used Iowa State University's meteorological archive data server, the Iowa Environmental Mesonet (IEM: /mesonet.agron.iastate.edu/index.phtml) archives, and Unisys archives (http://weather.unisys.com/archive/sfc_map) to acquire surface and upper air conditions at the time of a ramp event for determining a meteorological cause. For the central Iowa ramps, wind speed data were available from multiple turbines within the same wind farm, which allowed the study to analyze how ramps affected a portion of the wind farm as a unit. Knowing whether a ramp affects all turbines in a wind farm the same will greatly improve forecasting abilities.

Correlations were sought between ramps at Pomeroy and central Iowa for periods when data from both sites were available. Finally, we looked at the accuracy of 2-day persistence ramp forecasts. For all days within the Pomeroy and central Iowa ramp event data sets a 2-day persistence forecast was performed. If a ramp occurred within +/-6 hr of the forecasted event it was considered a hit. Hit rate (HR) (Eq. 1), false alarm rate (FAR) (Eq. 2), and threat score (TS) (Eq. 3) were calculated using the following equations:

$$HR = \frac{Total\ number\ of\ correct\ forecasts\ (hits)}{Total\ number\ of\ events\ observed} \quad \textbf{(1)}$$

$$FAR = \frac{Total\ number\ of\ false\ alarms}{Total\ number\ of\ events\ forecasted} \quad \textbf{(2)}$$

$$\mathrm{TS} = \frac{Total\ number\ of\ correct\ forecasts\ (hits)}{Total\ number\ of\ events\ forecasted + Total\ number\ of\ misses} \quad \textbf{(3)}$$

4. Results

This study identified 834 ramps at Pomeroy and 1324 ramps in central Iowa among the six turbines. In some cases, ramps were not observed at all six turbines. There was a contradiction between the 2010 Pomeroy ramps and the 2010 central Iowa ramps in that the Pomeroy ramp-ups peaked in frequency around 0101-0200 and 1101-1200 LST (Fig. 1) while the central Iowa ramp-ups peaked around 0601-0700 and 2301-0000 LST (Fig. 2). Central Iowa ramp-ups in 2011 peaked in frequency 0901-1000 and 2101-2200 LST. It should be noted that the very short time period studied, 28 June-16 August 2011, could affect results.

During the time period where data from Pomeroy and central Iowa overlapped, the correlation of ramp events was studied. It was found that 40% of ramp events in central Iowa occur within 6 hr of a ramp in Pomeroy, IA (Fig. 8) suggesting they are due to small scale features. A study of the causes of these ramps is still in progress; however it was found that the ramps in 2008 and 2009 in Pomeroy, IA were due mostly to storms and a strong pressure gradient (Fig. 9). Two-day ramp persistence forecasts were tested for accuracy; hit rate, false alarm rate, and threat score were calculated for Pomeroy and each of the six turbines in central Iowa (Fig. 7). More work will be done in the near future to measure the pressure gradient during ramp events to determine whether a certain threshold of mesoscale forcing is required to cause a ramp. Future work will also include analyzing ASOS wind speed data to determine whether ramps at the surface are correlated with ramps at 80 m. The hit rate never exceeded 45% and false alarm rate was never below 50%, while the threat score was variable between 12% and 20%.

5. Analysis and interpretation

While the central Iowa ramp-ups exhibited a strong diurnal cycle, the ramp-ups in Pomeroy, IA did not. Having wind speed data from six wind turbine nacelles at the central Iowa wind farm as opposed to the one meteorological tower in Pomeroy, IA might explain this. Another factor could be the length of the data set. The overlap of data from Pomeroy and central Iowa only lasted two and a half months. More data need to be tested in order to understand the diurnal cycle of ramp events. Deppe et al. (2012) found ramp-ups to peak in frequency from 1800-2100 LST and Freedman et al. (2008) agreed with a peak at 1900 LST. This study discovered more than one peak in frequency with ramp-ups, 0600-0900 LST and 2200-0000 LST in central Iowa and 0000-0200 LST and 1100-1200 LST in Pomeroy, IA. While the main peak in frequency did not occur from 1800-2100 LST as in Deppe et al. (2012), in Fig. 1 and Fig. 3 a distinct increase in frequency of ramp-ups can be noted during this time period. The early morning peak in frequency of ramp-ups could be attributed to the presence of the nocturnal low level jet. Ramp-downs showed a more consistent peak in frequency around 1700-1900 LST. This can be decoupling of the surface layer caused by nocturnal cooling.

Forty percent of ramps in central Iowa occurred within 6 hr of a ramp in Pomeroy, IA. This suggests that these ramps were due to small scale features, such as thunderstorms. Twenty percent of ramps in central Iowa and Pomeroy, IA occurred simultaneously. These ramps were due to larger scale features, such as a strong

pressure gradient or the low level jet. The causes of Pomeroy, IA ramp events were also analyzed. Most were attributed to storms, as Freedman et al. (2008) discovered, as well as strong pressure gradients and the presence of the low level jet. With many meteorological causes, ramp events still need to be studied further in order to better understand their behavior.

A two-day ramp persistence forecast performed at the central Iowa wind farm and the Pomeroy, IA location was found to be inaccurate (Fig. 7). Wind energy companies use this type of forecast as a measure of zero-skill. This forecast, performed in Pomeroy, IA and at each turbine by year had false alarm rates from 50-70%. This suggests that a persistence forecast should not be used to predict ramp events. Some sort of model forecast is needed to predict these events.

6. Conclusions

The analysis and forecasting of ramp events are very important for wind energy companies to harness all of their potential energy. As a climatology of wind speed at turbine height is created, the behavior of the wind is better understood. The causes of ramp events can be pinned down and better forecasts can be made. Future work for this study includes determining the causes of the ramp events observed in central Iowa. The mesoscale pressure gradient will also be calculated in order to determine whether ramps occur under certain mesoscale forcing. In central Iowa, ramps were not always observed at each turbine. Due to their east-west orientation and the “B” line being directly south of the “A” line of turbines, the wind direction will be studied to determine whether a particular angle creates ramps at certain turbines. Finally, ASOS wind speed data near the Pomeroy and central Iowa 80-m locations will be evaluated during the same time period to determine whether ramps at 10-m coincide with ramps at 80-m.

Acknowledgements

Support for this research was provided by a National Science Foundation Research Experience for Undergraduates site program in Wind Energy Science Engineering and Policy (WESEP) at Iowa State University.

References

Cutler, N., M. Kay, K. Jacka, and T. S. Nielson, 2007: Detecting, categorizing and forecasting large ramps in wind farm power output using meteorological observations and WPPT. *Wind Energy*, **10,** 453-470, doi: 10.1002/we.235.

Department of Energy, 2008: 20% wind energy by 2030. Energy Efficiency and Renewable Energy Rep. DOE/GO-102008-2567, 1-2.

Deppe, A. J., W. A. Gallus, Jr., and E. S. Takle, 2012: A WRF ensemble for improved wind speed forecasts at turbine height. *Weather and Forecasting*, in press, doi: 10.1175/WAF-D-11-00112.1.

Ferreira, C., J. Gama, L. Matias, A. Botterud, and J. Wang, 2010: A survey on wind power ramp forecasting. Argonne National Laboratory. ANL/DIS-10-13, 40 pp.

Francis, N., 2008: Predicting sudden changes in wind power generation. *North American Windpower*, 58-60.

Freedman, J., M. Markus, and R. Penc, 2008: Analysis of West Texas wind plant ramp-up and ramp-down events. AWS Truewind Report. 250-278.

Greaves, B., J. Collins, J. Parkes, and A. Tindal, 2009: Temporal forecast uncertainty for ramp events. *Wind Engineering*, **33,** 309–320.

Iowa Environmental Mesonet, cited 2012: Archived data & plots. [Available online at http://mesonet.agron.iastate.edu/archive/.]

Iowa State University, cited 2012: Mtarchive data server. [Available online at http://mtarchive.geol.iastate.edu/.]

Linden, S., S. Haupt, and B. Myers, 2012: Observation-based wind-power ramp forecast system. *92nd Amer. Meteorol. Soc. Annual Meeting,* New Orleans, LA, NCAR, 13.4.

Myers, W. and S. Linden, 2011: A turbine hub height wind speed consensus forecasting system. *Ninth Conference on Artificial Intelligence and its Applications to the Environmental Sciences*, Seattle, WA, NCAR, 1.2.

Unisys Weather, cited 2012: Image and map archive. [Available online at http://weather.unisys.com/archive/sfc_map/.]

Appendices

Table 1: Freedman et al. (2008) contingency table used to determine forecast outcome

Table 1 Contingency Table Representing Event Observation and Event Forecast

Event Forecast	Event Observation		Total
	Yes	*No*	
Yes	TP *(hits)*	FP *(false alarms)*	Forecast *Yes*
No	FN *(misses)*	TN	Forecast *No*
Total	Observed *Yes*	Observed *No*	N = TP + FP + FN + TN

TP = true positive; FP = false positive; FN = false negative; TN = true negative.

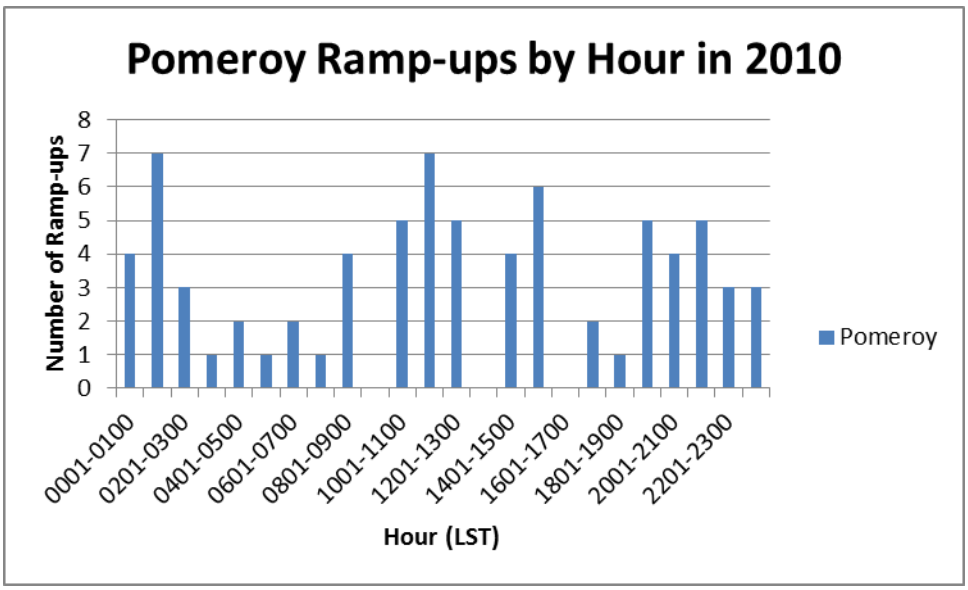

Figure 1: The number of ramp-ups by hour from 27 June – 8 September 2010 at 80 m in Pomeroy, IA

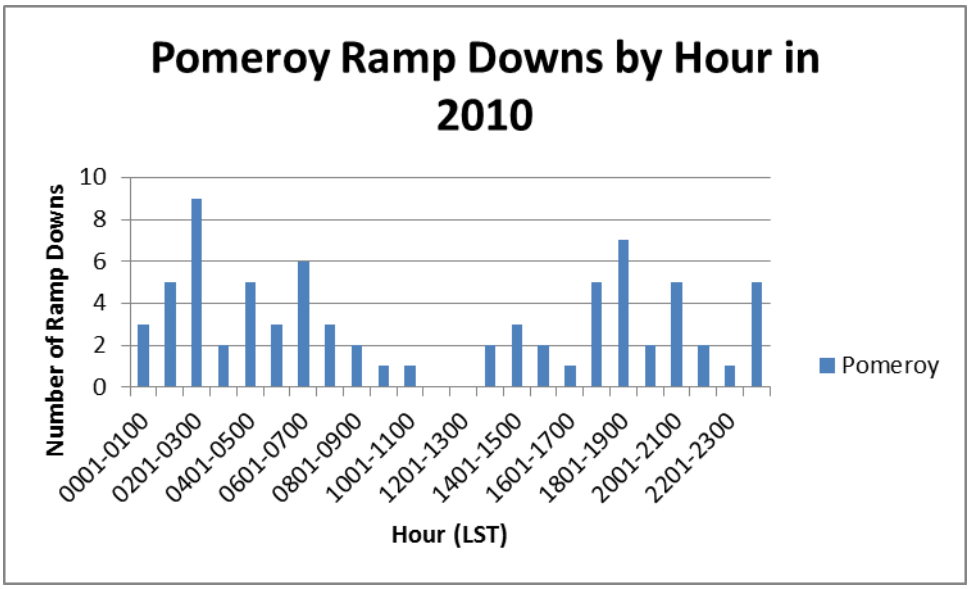

Figure 2: The number of ramp-downs by hour from 27 Jun – 8 September 2010 at 80 m in Pomeroy, IA

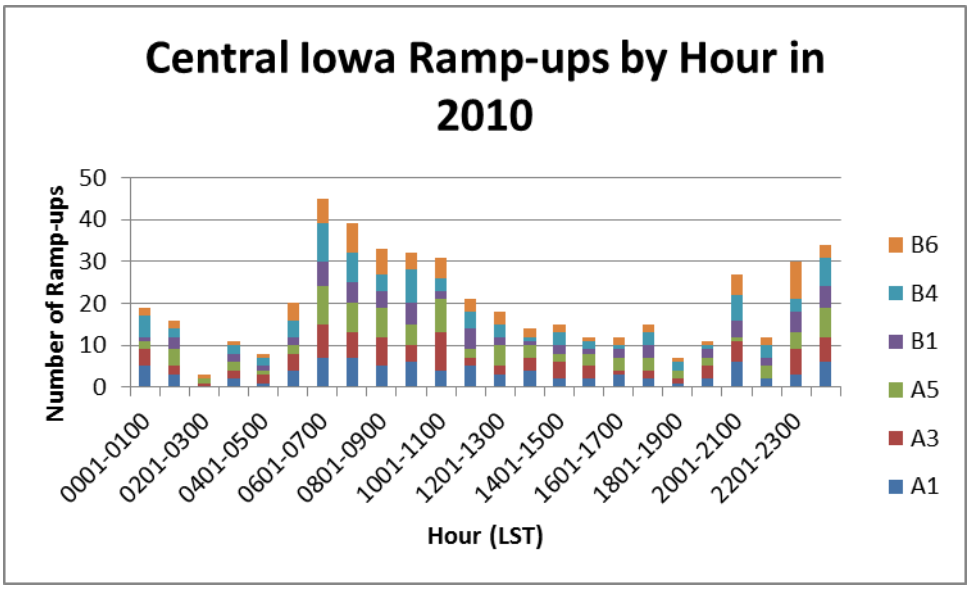

Figure 3: The number of ramp-ups by hour from 26 June-8 September 2010 at 80 m in central Iowa. Each color represents a different turbine.

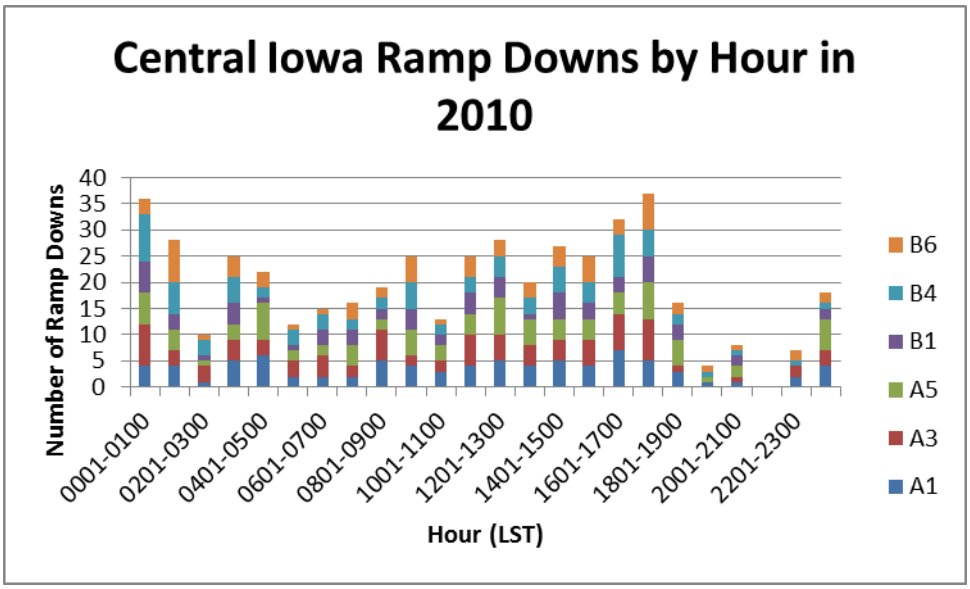

Figure 4: The number of ramp-downs by hour from 26 June-8 September 2010 in central Iowa. Each color represents a different turbine.

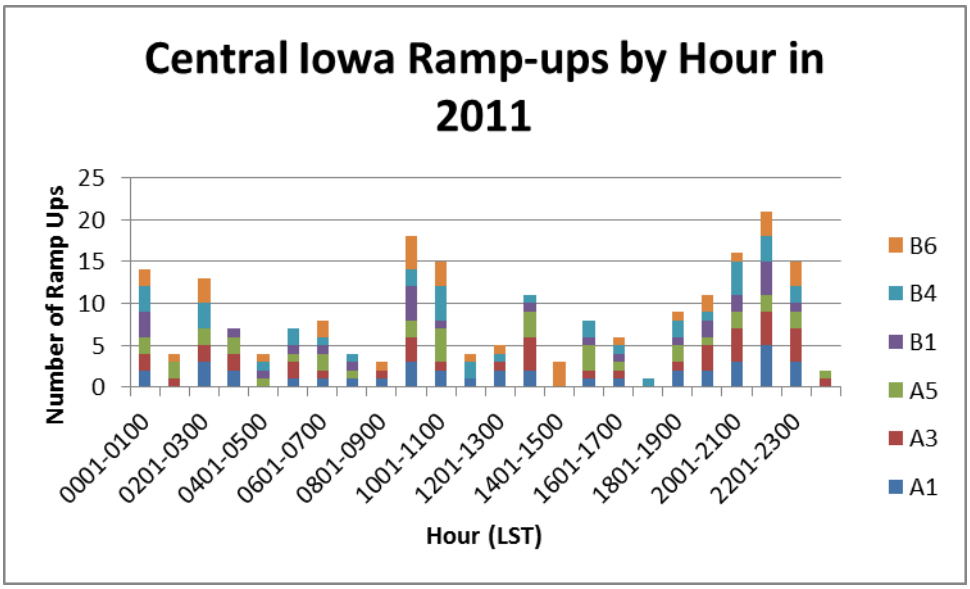

Figure 5: The number of ramp-ups by hour from 28 June-16 August 2011 in central Iowa. Each color represents a different turbine.

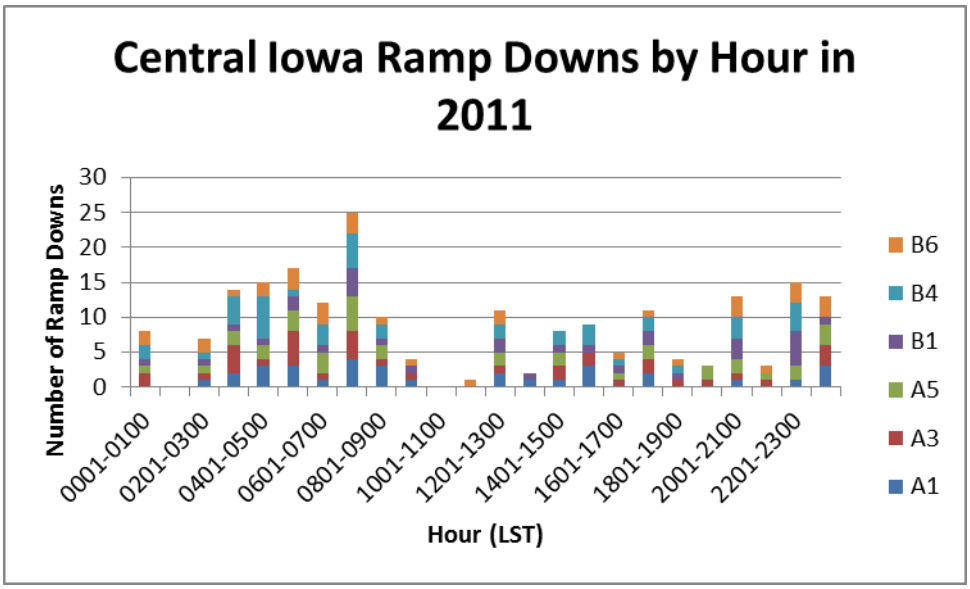

Figure 6: The number of ramp-ups by hour from 28 June-16 August 2011 in central Iowa. Each color represents a different turbine.

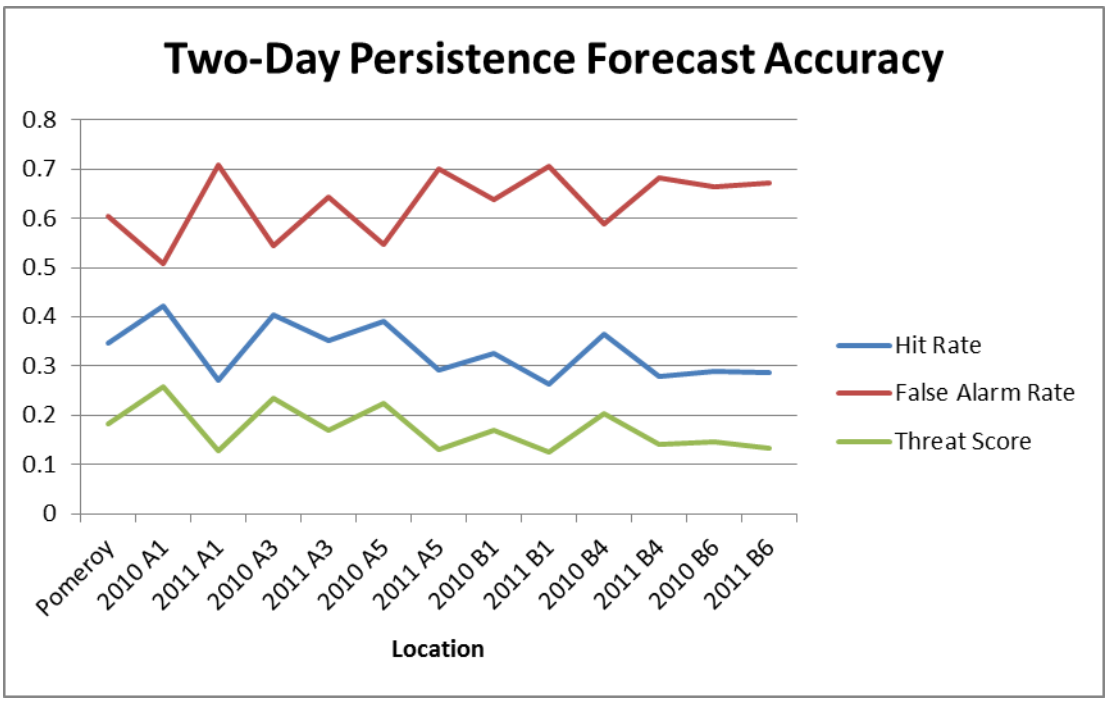

Figure 7: Two-day persistence forecasts performed for Pomeroy and each central Iowa turbine by year. False alarm rates ranged from 50-70% with hit rates from 30-40% suggesting a need for model forecasts.

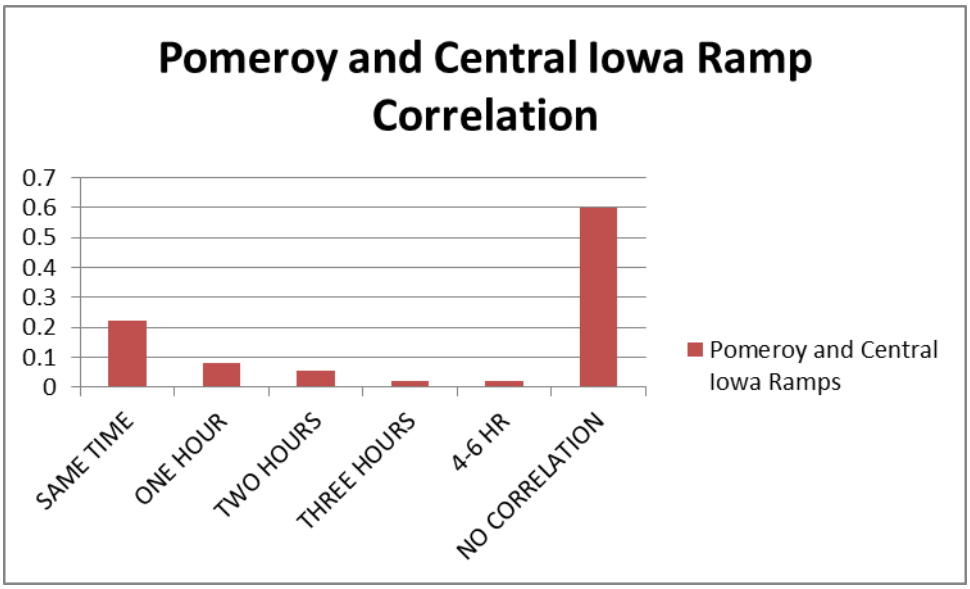

Figure 8: Forty percent of ramps in central Iowa occur within 6 hours of a ramp in Pomeroy, suggesting ramps are due to small-scale features.

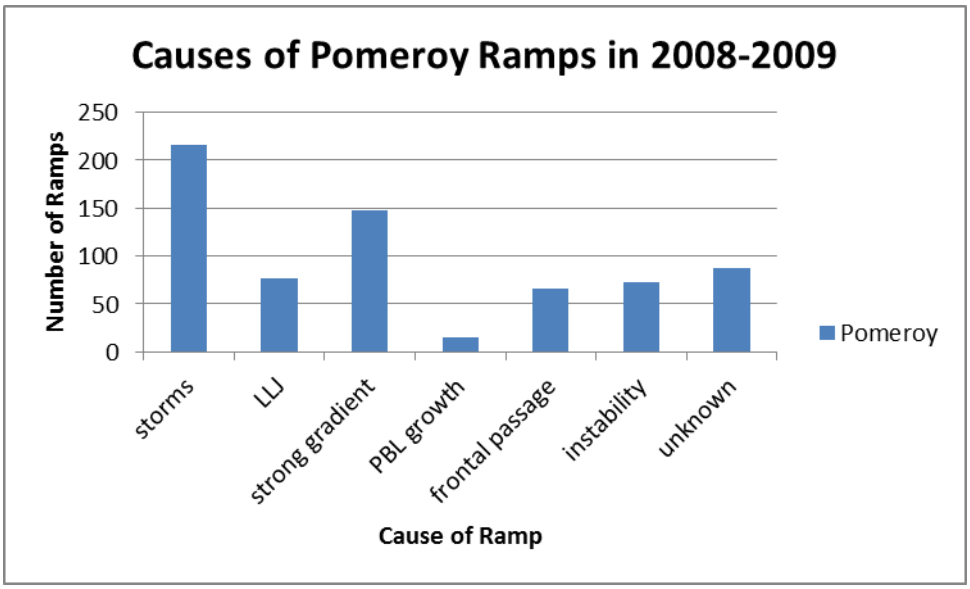

Figure 9: Ramps in Pomeroy from 2008-2009 were mainly due to storms. Further work will look into the causes of ramps in central Iowa.

Influence of Wind Turbines on Atmospheric Stability and Dew Duration

MATTHEW J. LAURIDSEN
Wind Energy Science Engineering and Policy REU, Iowa State University, Ames, Iowa
Mentors: Eugene S. Takle and Daniel J. Rajewski

Abstract

Recent scientific research has concluded that wind farms have an impact on local meteorology; however, the impacts on dew duration and near-surface atmospheric stability have not been reported in these published studies. As air passes through the turning blades of wind turbines, turbulence is generated. This turbulence enhances the vertical mixing in the atmosphere, which is thought to have an influence on atmospheric stability. In this study, the gradient Richardson number and Obukhov stability parameter are calculated and compared both upwind as well as in the wake region downwind of a line of turbines in a utility-scale wind farm. Given that the presence of dew is impacted by near-surface stability, the duration of dew is also hypothesized to be impacted downwind of wind farms. In this study, dew duration is quantified and compared at locations upwind and downwind of a line of turbines. Results from the stability study indicate there is a significant decrease in both the gradient Richardson number and Obukhov stability parameter in the wake of wind turbines. However, the dew study is more inconclusive. With the stability study providing promising results, there is a good basis for exploring alternative methods in a future dew duration study.

1. Introduction

Using data from the Crop/Wind-energy EXperiment (CWEX) at a central Iowa wind farm, I will quantify the impact of wind turbines on atmospheric stability and dew duration. As air passes through the turning blades of wind turbines, turbulence is generated. This turbulence enhances the vertical mixing in the atmosphere, often warming the surface at night and cooling it during the day. The turbine-enhanced vertical mixing usually produces a stronger effect at night due to the atmospheric boundary layer (ABL) being more stable and thinner than during the day. This turbulence-enhanced temperature change is noted to cause a change in the stability of the atmosphere, and that stability change will be examined in this research in terms of the gradient Richardson number *Ri* and the Obukhov stability parameter *z/L*. Additionally, turbulence generated by the turbines is suggested to wick away dew from nearby crops in the morning. This possible shortening of the dew duration will be another focus of this research. All of this information leads to two proposed hypotheses: 1) the turbine-enhanced vertical mixing will lead to a decrease in surface-layer stability, and 2) if (1) is correct, then dew duration will be shortened. The motivation for this study is that crop vulnerability to diseases is enhanced by the presence of dew, so an impact of turbines on dew duration could indirectly impact crops.

2. Literature review

Recent studies have concluded that the turbine-enhanced vertical mixing due to increased turbulence downwind of wind farms can significantly affect local weather. Such effects include a near-surface air temperature increase at night and early in the morning, and a decrease of temperature during the day (Baidya Roy et al. 2010), as well as changes in humidity and heat flux

(Baidya Roy 2011). Effects on the local weather are also stronger at night when the ABL is thinner and more stable as opposed to during the day (Zhou et al. 2012). Using the RAMS regional climate model to simulate effects of a wind farm as well as observations taken at the San Gorgonio wind farm in California during the summer of 1989, Baidya Roy et al. (2010) observed that downwind surface temperatures are increased during the night and decreased during the day. Temperatures often increase downwind of a wind farm during the night as the enhanced vertical mixing brings down warmer air aloft, warming the surface. However during the day, the air aloft is cooler, so enhanced vertical mixing will cool air at the surface. More recently, Baidya Roy (2011) again used the RAMS regional climate model and in this case initialized using radiosonde measurements from various locations in the western United States. Baidya Roy (2011) determined that the downwind enhanced vertical mixing carries down air that may have a different mixing ratio. As a result, downwind near-surface humidity will increase if the ambient mixing ratio lapse rate is positive, and decrease when the lapse rate is negative.

While modeling studies have suggested wind farms may change the stability of the ABL (Zhou et al. 2012), there is a lack of published articles that quantify this change in stability based on field measurements. In this research, the gradient Richardson number and Obukhov stability parameter are calculated and compared both upwind as well as in the wake region downwind of a line of turbines in a utility-scale wind farm. Likewise, there is an absence of published studies that discuss the change in dew duration downwind of a wind farm. Baidya Roy (2011) stated that humidity is changed downwind if air with a differing ambient mixing ratio is mixed down to the surface. Given that the presence of dew is impacted by near-surface humidity as well as stability, the duration of dew is likely impacted downwind of wind farms. In this study, dew duration is quantified and compared at locations upwind and downwind of a line of turbines.

3. Experimental methods

Data used in this study comes from the Crop/Wind-energy EXperiment 2011 (CWEX11) at Iowa State University. CWEX11 data was collected by two flux stations provided by Iowa State University located in the southern region of a central Iowa wind farm consisting of 200 1.5 MW GE turbines located in a NW-SE orientation. One flux station, “ISU1”, was located 160 m south of a line of turbines, and the other flux station, “ISU2”, was located 260 m north of the same line of turbines. This line of turbines is referred to as the “B-line”. Both ISU1 and ISU2 were positioned in corn fields, and recorded data in 10-min averages from 1 July – 16 August 2011. Each flux station measured temperature and relative humidity at 1 m, 3 m, and 8 m above the surface, as well as wind speed at 3 m and 8 m, net radiation, canopy temperature, pressure, precipitation, soil moisture, and heat flux. A sonic anemometer at 5 m also reported wind speed components and temperature at both locations. Furthermore, hub data from the B-line turbines including temperature, wind speed, yaw angle, power, and a turbine status of on/off were supplied for the period at 10-min intervals.

From these data, the gradient Richardson number *Ri* and Obukhov stability parameter *z/L* were calculated at the locations of ISU1 and ISU2 when ISU2 was in the wake of one of the B-line turbines, as well as when neither flux station was in the wake of a turbine. The equations used to calculate *Ri* and *z/L* are as follows:

$$Ri = \frac{\frac{g}{\overline{\theta}} \frac{\partial \overline{\theta_v}}{\partial z}}{\left(\frac{u_8 - u_3}{8\ m - 3\ m}\right)^2}$$

$$z/L = \frac{-zkg\overline{w'T'}}{Tu_*^3}$$

where g is gravity, θ is potential temperature, $\overline{\theta_v}$ is the mean virtual potential temperature, z is height, u_8 is wind speed at 8 m, u_3 is wind speed at 3 m, k is a von Karman constant, $\overline{w'T'}$ is the mean temperature flux, T is temperature, and u_* is friction velocity. Additionally, three sonic leaf wetness sensors were placed both north and south of the B-line. These sensors consist of plates over which a current passes, and that current is altered in the presence of dew. The sensors report values in mV that can then be interpreted to determine dew duration and intensity. The dew duration for the north and south sensors were then compared for nights and mornings when the turbines were running and the north sensors were in the turbine wake.

To ensure quality of results, guidelines were set in place when selecting data for the stability study. Data was only used when a turbine reported a yaw angle coinciding with a wake over ISU2 for a minimum of 10 min. With data being collected at 10-min intervals, this translates to a minimum of two consecutive reports of a wake over ISU2. For the control group, a no-wake case where neither ISU1 nor ISU2 were in the wake of a turbine was also examined. The wind direction angles used for the four wake cases and one west no-wake case are as follows:

	Wind direction
B1 wake	226-246 degrees
B2 wake	192-216 degrees
B3 wake	136-160 degrees
B4 wake	118-128 degrees
No-wake	260-280 degrees

To compensate for wind shear, data within a ±3 degree window of the four wakes was added to the dataset. After categorizing the data into the one no-wake and four wake cases, *Ri* and *z/L* were calculated, as well as the ISU2-ISU1 difference for these two stability parameters. Critical *Ri* values of ±2 and critical *z/L* values of ±10 were used. Average ISU2-ISU1 differences were calculated for the five *Ri* and five *z/L* cases, and a paired t-test was used to determine statistical significance. An alpha value of 0.01 was used when comparing the p-value for significance. The number of data points for each category is as follows:

		Number of data points
Ri	B1 wake	141
	B2 wake	435
	B3 wake	588
	B4 wake	262
	No-wake	103
z/L	B1 wake	135
	B2 wake	431
	B3 wake	570
	B4 wake	244
	No-wake	84

4. Results

The average ISU2-ISU1 *Ri* difference was found to be negative in the wakes of turbines B1, B2, B3, and B4. Likewise, the average *z/L* difference was negative in the wakes of B1, B2, B3, and B4. The ISU2-ISU1 *Ri* differences while ISU2 was in the wake of turbines B1, B2, B3, and B4 can be found in Figs. 1, 2, 3, and 4, respectively. Figs. 5, 6, 7, and 8 represent the ISU2-ISU1 *z/L* differences while ISU2 was in the wake of turbines B1, B2, B3, and B4, respectively. Statistical analysis in the form of a paired t-test using an alpha value of 0.01 showed all

results were statistically significant, with the exception of the *z/L* decrease in the wake of turbine B4. For the non-wake case when winds were coming from the west, ISU2 reported a lower *Ri* and higher *z/L* than ISU1. The decrease in *Ri* was found to be statistically significant; however, the increase in *z/L* is not significant. The ISU2-ISU1 *Ri* and *z/L* differences for the no-wake case are found in Figs. 9 and 10, respectively. Data points for all wake cases were compiled together and a total average was also computed for the Ri and z/L difference. Both of these total averages showed significant decreases in stability. The average ISU2-ISU1 differences for each case are as follows:

		Average difference (ISU2-ISU1)
Ri	B1 wake	-0.1031
	B2 wake	-0.1157
	B3 wake	-0.1164
	B4 wake	-0.0702
	Total wake cases	-0.1064
	No-wake	-0.2185
z/L	B1 wake	-0.3336
	B2 wake	-0.8371
	B3 wake	-0.1852
	B4 wake	-0.0606*
	Total wake cases	-0.3813
	No-wake	+0.1187*

*not significant

For the dew duration study, the quantification of duration with the leaf wetness sensors largely proved inconclusive. Figs. 11, 12, and 13 display different leaf wetness reports that represent the dataset. Fig. 11 shows good dew readings with the exception of the ISU1 sensor that stayed flat the entire night. Fig. 12 represents an average report from the sensors during a period with precipitation. The two spikes in the graph occur concurrently with two periods of rain from 02:10-02:30 LST and 05:30-05:40 LST. Finally, Fig. 13 shows an average reading when the wetness sensors malfunctioned and didn't report any dew.

5. Analysis and Conclusions

As hypothesized, the surface-layer stability is decreased in the wake of a wind turbine. Upon further analysis, it can be seen that the ISU2-ISU1 stability differs most at night. The fact that changes are more pronounced at night is supported by Zhou et al. (2012), who noted that effects on local weather are stronger at night when the ABL is thinner and more stable as opposed to during the day. With the atmosphere more unstable during the day, stability isn't affected much as the atmosphere is already well mixed. During the night under stable conditions, the wake of the turbine enhances vertical mixing, leading to a decrease in stability. A focus for future research will include splitting the wake data into overall atmospheric stability categories (stable, neutral, and unstable) and calculating ISU2-ISU1 *Ri* and *z/L*. A paired t-test will again be used to determine the statistical validity of the results. With greater stability decreases found at night, it is hypothesized that the stability will have a significant decrease in the wake of a turbine during stable conditions. For the most part, turbines B2 and B3 are seen to generate a stronger decrease in stability. With the location of ISU2 as seen in Fig. 14, turbines B2 and B3 are at a shorter distance from the ISU flux stations as opposed to B1 and B4. This closer distance is thought to lead to a more concentrated area of increased mixing, thus leading to a greater decrease in stability. With the decrease in stability among the wake groups easily explained by the turbine wakes, another explanation must be sought for the *Ri* decrease in the no-wake case. ISU1 and ISU2 were both positioned in fields of corn, however the fields were

owned by different farmers. Varying farming techniques, planting times, or corn types may have led to a difference in potential temperature or mean virtual potential temperature between ISU1 and ISU2, possibly leading to differing gradient Richardson numbers.

An inconclusive study for dew duration leads to more questions and thoughts for future studies than answers. The three sensors at each location all reported varying dew durations, and no location reported all three dew durations as greater than or less than the three dew durations reported at the second location. Precipitation as seen in Fig. 12, faulty sensor readings as seen in Fig. 13, corn transpiration, and other possible factors also greatly limited the dataset of good dew duration reports. Future dew duration research will be conducted using other methods to quantify dew duration such as the sign of moisture flux at ISU1 and ISU2. Leaf wetness and moisture flux data from the Crop/Wind-energy EXperiment 2012 (CWEX12) may also be used.

Acknowledgements

Support for this research was provided by a National Science Foundation Research Experience for Undergraduates site program in Wind Energy Science Engineering and Policy (WESEP) at Iowa State University. Data were provided by the Crop/Wind-energy EXperiment at Iowa State University (CWEX).

References

Baidya Roy, S., and J.J. Traiteur, 2010: Impacts of wind farms on surface air temperatures. *Proc. Natl. Acad. Sci*., **107**, 17899-17904.

Baidya Roy, S., 2011: Simulating impacts of wind farms on local hydrometeorology. *J. Wind Eng. Ind. Aerodyn*., **99**, 491-498.

Zhou, L., Y. Tian, S. Baidya Roy, C. Thorncroft, L. F. Bosart, and Y. Hu, 2012: Impacts of wind farms on land surface temperature. *Nature Clim. Change*, doi:10.1038/nclimate1505.

Appendices

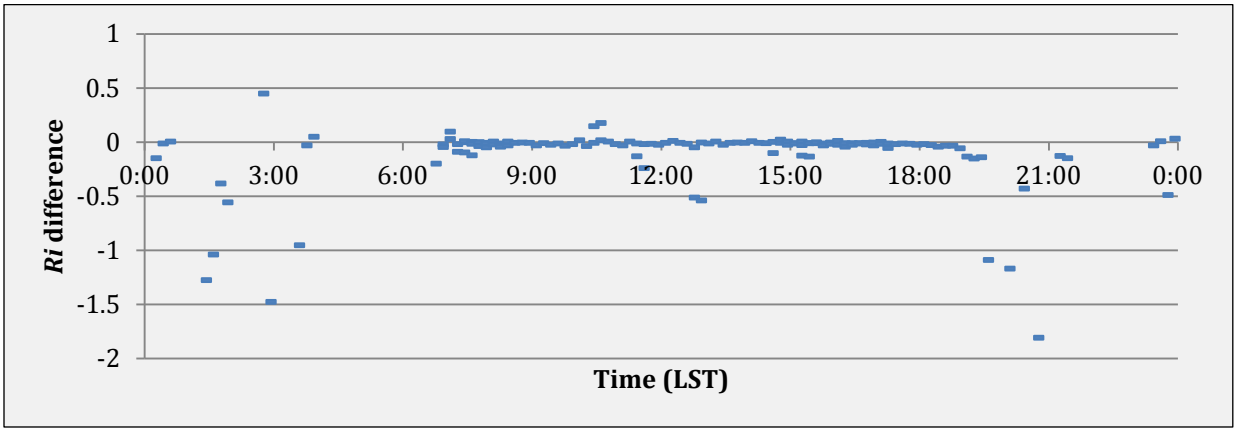

Figure 1. *Ri* change in the wake of B1. ISU2 *Ri*–ISU1 *Ri*.

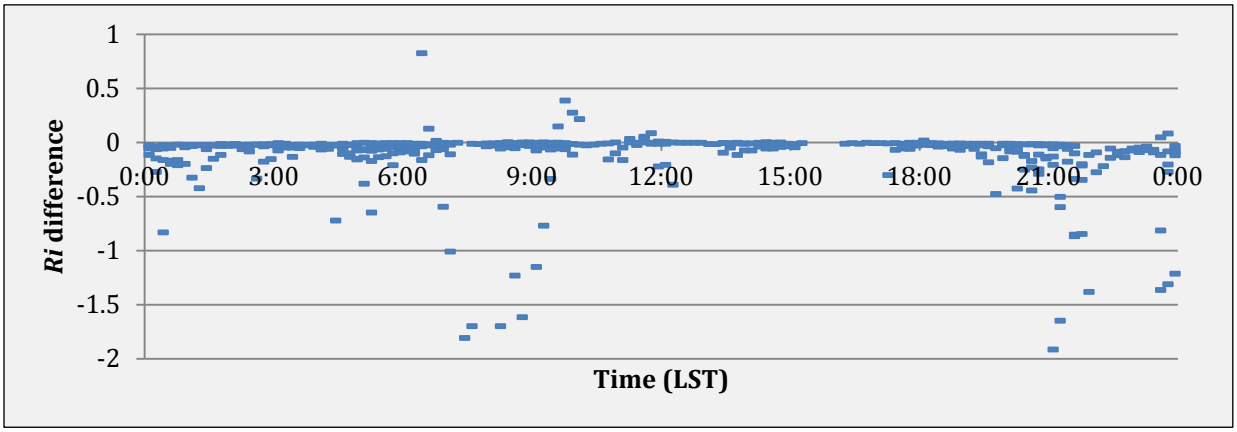

Figure 2. *Ri* change in the wake of B2. ISU2 *Ri*–ISU1 *Ri*.

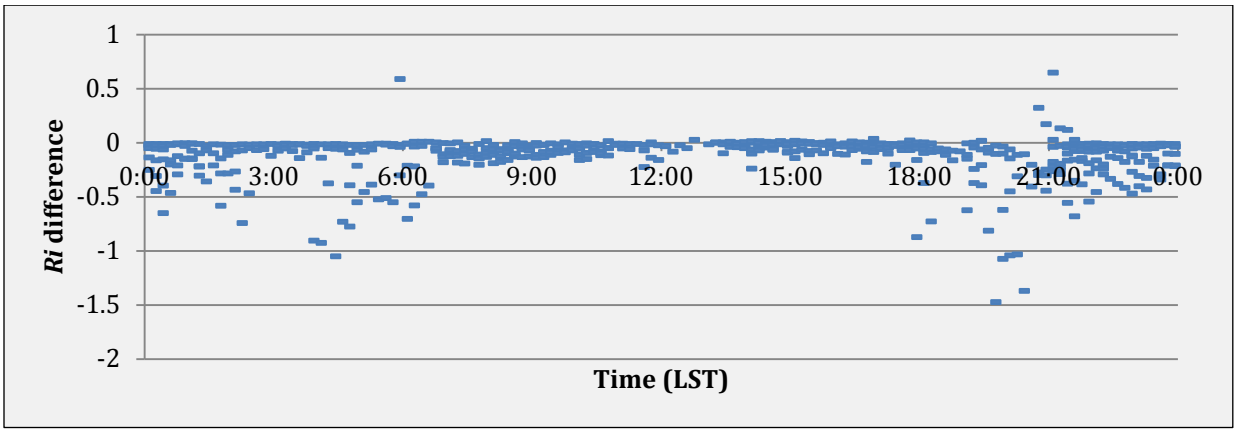

Figure 3. *Ri* change in the wake of B3. ISU2 *Ri*–ISU1 *Ri*.

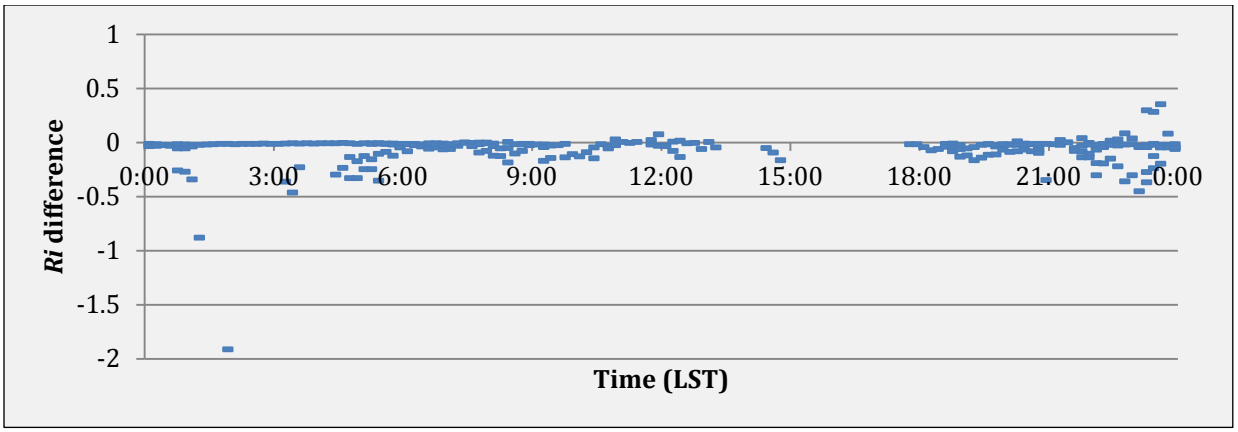

Figure 4. *Ri* change in the wake of B4. ISU2 *Ri*–ISU1 *Ri*.

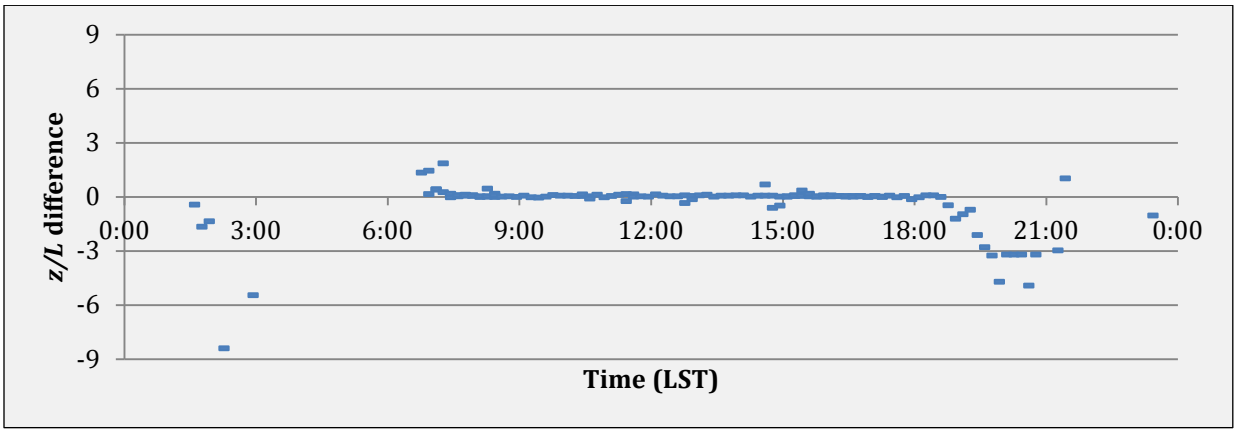

Figure 5. *z/L* change in the wake of B1. ISU2 *z/L*–ISU1 *z/L*.

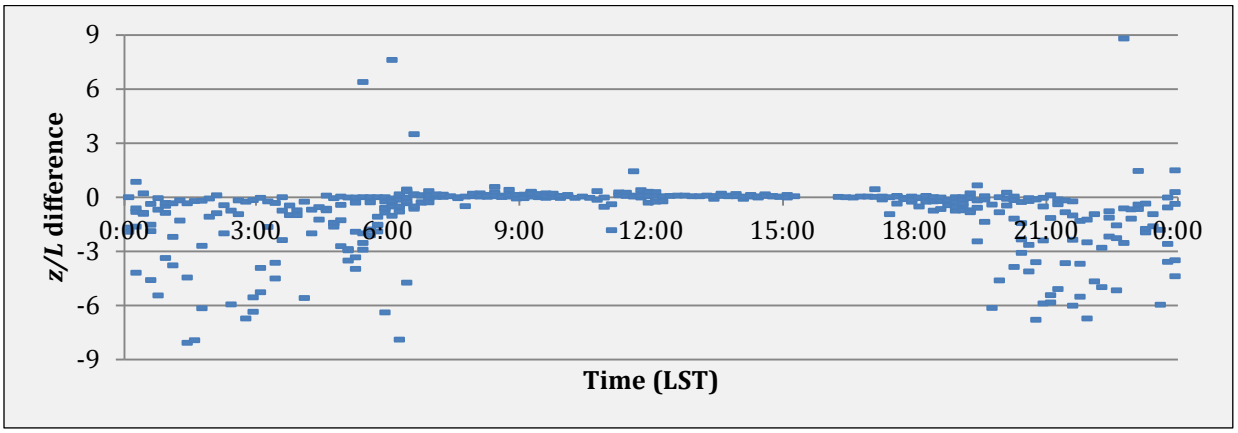

Figure 6. *z/L* change in the wake of B2. ISU2 *z/L*–ISU1 *z/L*.

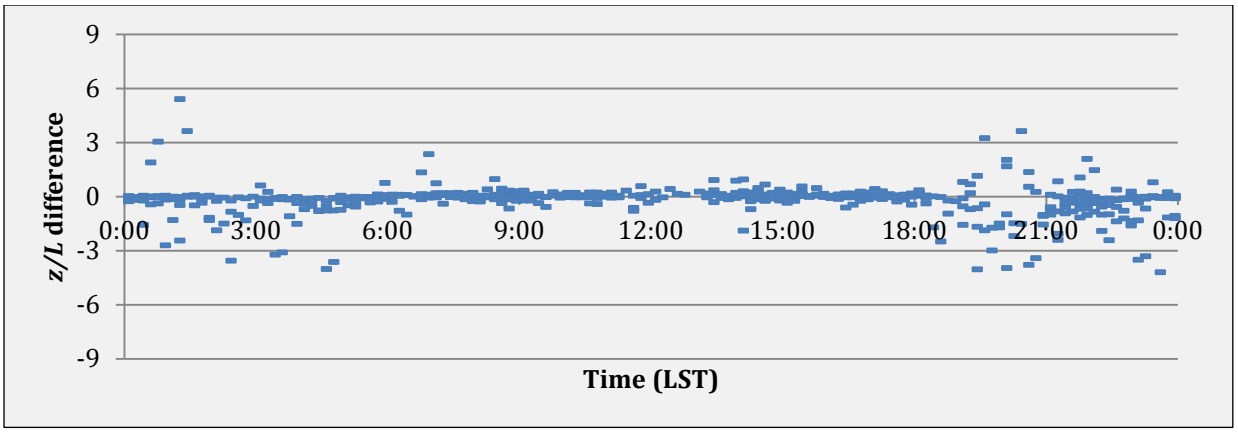

Figure 7. *z/L* change in the wake of B3. ISU2 *z/L*–ISU1 *z/L*.

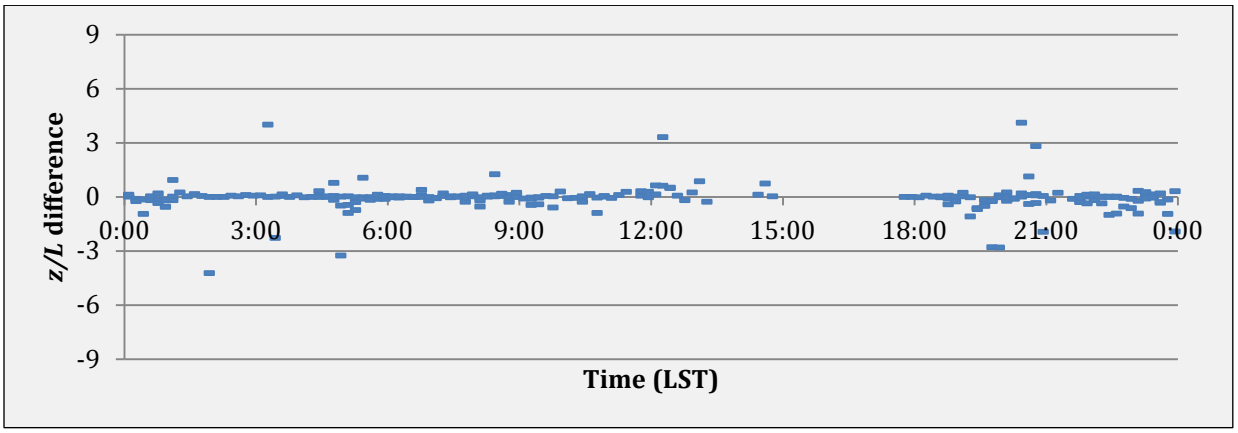

Figure 8. *z/L* change in the wake of B4. ISU2 *z/L*–ISU1 *z/L*.

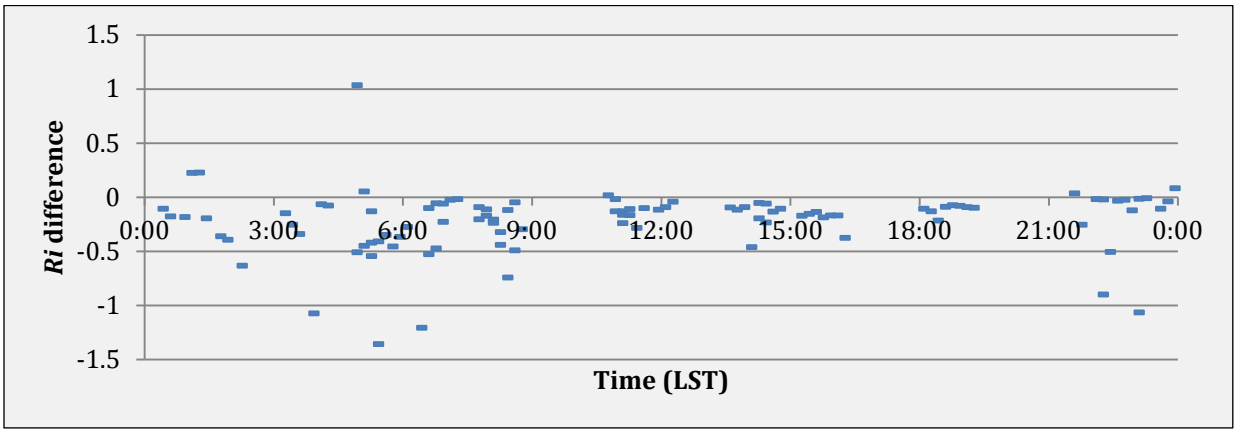

Figure 9. *Ri* change in the west no-wake case. ISU2 *Ri*–ISU1 *Ri*.

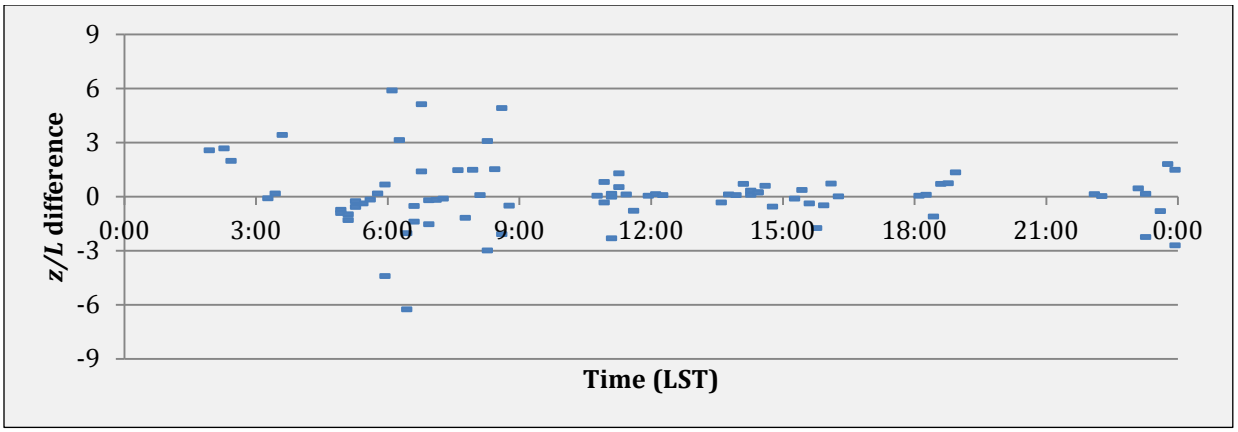

Figure 10. *z/L* change in the west no-wake case. ISU2 *z/L*–ISU1 *z/L*.

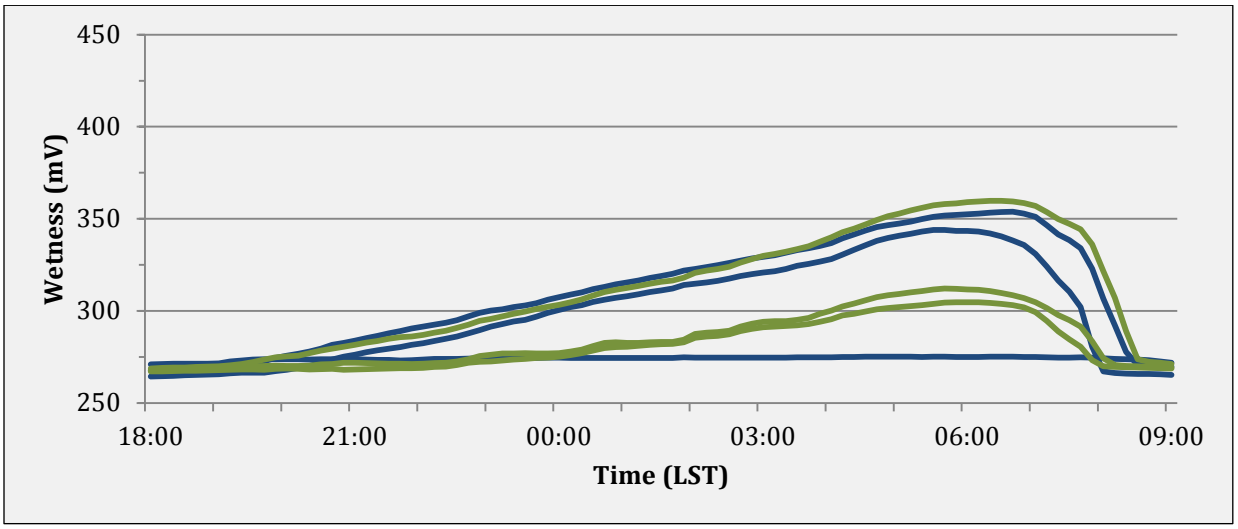

Figure 11. Leaf wetness sensor readings, 25 July – 26 July 2011. Blue: ISU1, Green: ISU2.

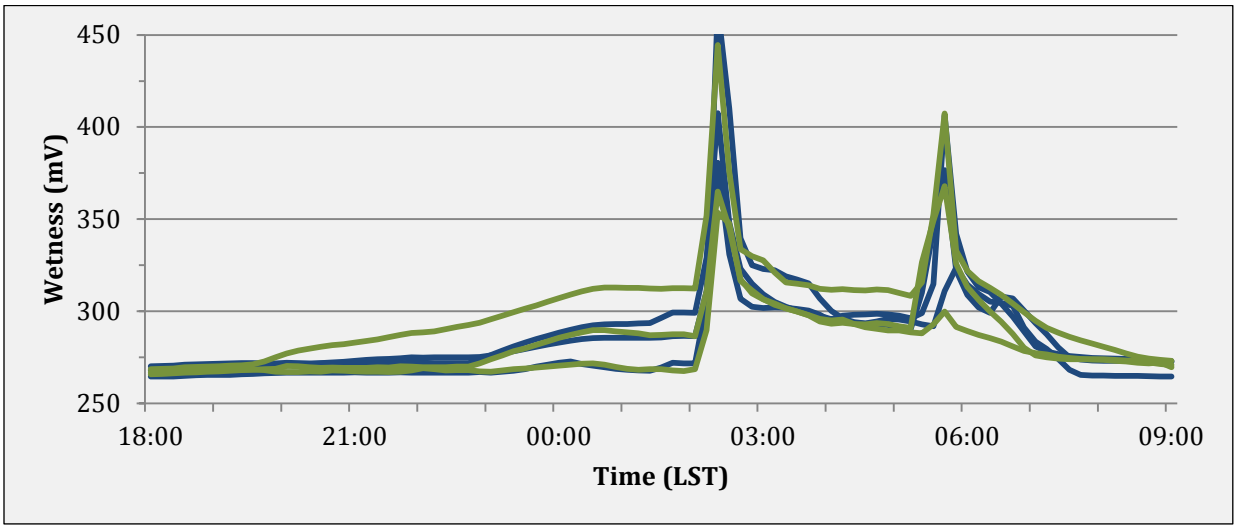

Figure 12. Leaf wetness sensor readings, 7 August – 8 August 2011. Blue: ISU1, Green: ISU2.

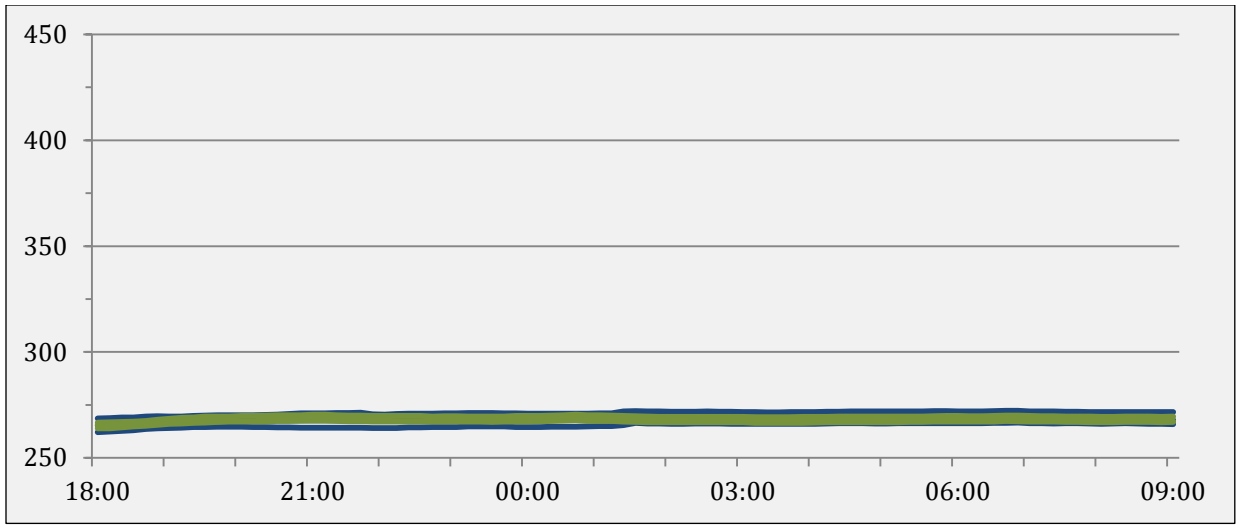

Figure 13. Leaf wetness sensor readings, 11 August – 12 August 2011. Blue: ISU1, Green: ISU2.

Figure 14. Location of CWEX11 instruments near the B-line.

Compression Failure in Marcels of Wind Turbine Blades

TRAVIS L. TASKER
Wind Energy Science Engineering and Policy REU, Iowa State University, Ames Iowa
Mentors: Vinay Dayal, Lisa Brasche, and Ryan Kafka

Abstract

The use of nonrenewable energy resources is diminishing fossil fuel reserves, increasing atmospheric greenhouse gases, and raising global health concerns; renewable energy may be one solution. Today, wind is exploited as an energy source in many areas because it is abundant and its environmental costs are relatively well understood. However, in order for wind to be a viable renewable energy source, turbine blades that are cheaper stronger, lighter, and longer-lived need to be developed. During blade manufacturing, defects such as dry patches, wrinkles, delamination, poor curing, and fiber misalignment are common. A wrinkle, also known as a marcel, is formed when fiber layers are unable to lay flat during infusion; the result is an outward wrinkle. Previous studies indicate that marcels can significantly decrease the compressive strength and fatigue life of composites. The purpose of this research was to test the influence of marcel size on composite compressibility and failure. To do this, artificial epoxy waves with different aspect ratios (12-20) were placed in the middle of 10 fiberglass layers during infusion. Compression and fatigue analysis was then performed on samples using an Instron and MTS testing machine. Two equations were developed for predicting the effect of wrinkle size on compressive strength and elasticity. In addition, compressive strength of the largest studied wave decreased by up to 47%. However, judging by the similarity between the control's and AR 20's failure loads, AR 20's or higher may be acceptable for wind turbine blades. Further analysis on fatigue life and compressive strength of AR's above 20 may be important in resolving what size marcels are suitable for blades.

1. Introduction

Excessive use of nonrenewable energy resources is diminishing fossil fuel reserves, increasing greenhouse gas concentrations in the atmosphere, and raising health concerns; renewable energy may be the solution (Panwar, Kaushik, & Kothari, 2011). Renewable energy resources such as wind, tidal, solar, *etc*. emit zero greenhouse gases and currently contribute 14 % of the world's energy (Panwar, Kaushik, & Kothari, 2011). Harvesting these resources is a sustainable method to fulfill energy needs and reduce environmental concerns (Varun & Bhat, 2009).

Today, wind is being exploited as an energy source because it is well understood and abundant (Esteban, Diez, López, & Negro, 2011). Although wind is seasonal, the energy created from wind turbines could be substantial (Sahin, 2004). A report by the U.S. Department of Energy in 2008 set out a plan where wind would provide 20% of the U.S. electricity by 2030; however, in order to achieve this goal, significant challenges need to be overcome (U.S. Department of Energy, 2008). One challenge is the development of cheaper, reliable, and longer blades (Yerramalli *et al*., n.d.).

Blades are crucial for energy production in wind turbine systems (Veers *et al.*, 2003). Based on their size, weight, and reliability requirements, composite blades made from fiberglass or graphite fibers cured in a polymer matrix are the only viable methods for blade production. During their manufacturing, blades often incur material defects that may degrade their mechanical properties. One of the most common defects is composite waviness. The goal of this paper is to test the compressibility of

fiberglass composite materials with artificially induced waves to improve the understanding of fiber waviness on compressive strength.

2. Background

Blades typically represent 10-15% of the total installed capital cost of a wind turbine system (Veers *et al.*, 2003). Therefore, in order for wind energy to be feasible, turbine blades that are cheaper, stronger, lighter, and durable need to be developed.

Blades are exposed to external loads originating from wind and gravity (Brondsted *et al.*, 2005). Wind induces both flap wise (load in the flexible direction) and edgewise (load in stiff direction of the chord line) bending on blades, causing both tension and compression (Hayman *et al*, 2008; Brondsted *et al.*, 2005). Additionally, blades undergo tension and compression from gravity when in the horizontal and vertical positions (Hayman *et al*, 2008; Brondsted *et al.*, 2005). As a result, the blades must be able to withstand both extreme and time-varying loads over its life. (Hayman *et al*, 2008).

The material requirements for blades are a high material stiffness for aerodynamic performance, low density to reduce gravitational forces, and a long-fatigue life (Brondsted *et al.*, 2005); carbon-fiber, fiberglass, and wood meet some of these specifications (Hayman *et al*, 2008; Yerramalli *et al*., n.d.). The most common material for wind turbine blades is fiberglass (Veers *et al.*, 2003). The fibers are typically combined through a laminating process with resins such as polyester, epoxy, or vinylester (Hayman *et al*, 2008). This laminating procedure is often crucial in establishing the blade's material properties (Hayman *et al*, 2008).

Manually manufacturing blades is the best way to keep costs at a minimum. Vacuum assisted resin infusion is the most common process for blade production (Hayman *et al*, 2008). Since wind induces bending stress primarily in the longitudinal direction, the majority of fiber layers are arranged along the length of the blade during infusion for reinforcement under compression and tension (Hayman *et al*, 2008). However, during blade manufacturing, defects such as dry patches, wrinkles, delamination, poor curing, and fiber misalignment are common (Yerramalli *et al*, n.d.; Figure 1). Wrinkles, also known as marcels, are formed when the fiber layers are unable to lie completely flat during infusion; the result is an outward wrinkle (Hayman *et al*, 2008). The main reason for this is that a flat sheet of fiberglass is draped on a doubly curved surface; hence, wrinkles are bound to occur. The thermal curing also enhances this effect. The sizes of the marcels are often characterized by their aspect ratios, a ratio of the wave length to height (Chakrapani, 2011).

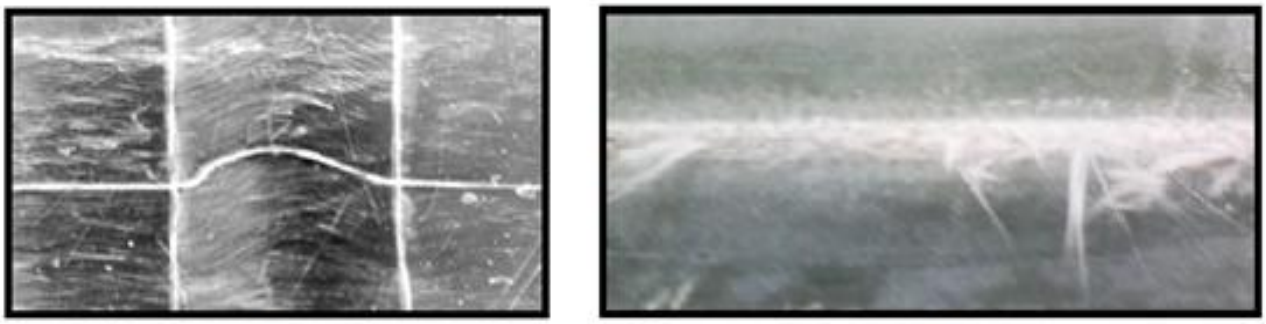

Figure 1. A) In plane waviness (photo from Mandell *et al.*, 2003). B) Dry spot in a composite material.

Waves are classified into two categories: (1) intrinsic waves that have no surface effects and (2) extrinsic or surface waves (Chakrapani, 2011). Wrinkles can significantly decrease the compressive strength and fatigue life of a composite (Hayman *et al*, 2008; Yerramalli *et al*, n.d.); the localized area of the marcel has lower mechanical properties than the rest of the composite material (Chakrapani, 2011). According to a study by Yerramalli *et al* (n.d), composite strength decreased as the aspect ratio decreased (lower aspect ratio means a bigger wave). Murri (1999) suggested that fatigue life is also affected by fiber waviness; research showed that a composite with waves decreased the fatigue life by a factor of 10^2 to 10^3. Adams and Bell (1994) reported that the strength reductions also depend on the number of fiber layers in the marcels. Additionally, the mechanical properties of matrix are important for the compressive strength of composites. Epoxy resin was shown to increase the compressive strength by 10-15% compared to vinyl ester (Veers *et al.*, 2003).

Two factors are believed to be responsible for a reduction in compressive strength of composites: (1) the wave may force fibers into a position that exacerbates the strand and (2) the wave creates a weak area for matrix dominated failure (Mandell *et al.*, 2003). However, there is still inconclusive evidence regarding the size (or aspect ratio) of waves suitable for meeting inspection or performance measures. Therefore, the goal of this project was to test the compressibility of fiberglass composite materials manufactured with marcels containing aspect ratios of 12-20. The results will improve understanding of the effect of fiber waviness on compressive strength.

3. Experimental Details

Infusion Mold

The mold was made from 40 fiberglass plies infused together with an epoxy matrix (after cut dimensions of 23" X 18"). A one inch wide piece of plexiglass (3/8" thick) followed the outside edge of the mold, yielding a set thickness for infused samples. Additionally, 2 cuts at each end of the mold were made in the plexiglass; one cut for an epoxy input and the other for a vacuum port (Figure 2).

Infusion and lay-up process

Molds were prepped for infusion by placing three coats of releasing agent (Frekote's 770-NC) and one coat of sealer (Frekote's B-15) on the surface. Two ten layer unidirectional fiberglass sheets (dimensions of 19" X 15.5") were then placed in the mold side by side; during the layup process, all fiberglass samples were surrounded on both sides by a peal cloth and an infusion grid to prevent dry spots and mold bonding (Figure 2). Depending on the desired characteristics of the composite, waves were artificially induced in samples by positioning epoxy molded waves with various aspect ratios at the center of the fiberglass layers; the aspect ratios (AR's) used in this study were 12, 16, 18, and 20. Before infusion, the top, bottom, and ports of the mold were sealed using tack tape. The system was then placed under vacuum (approximately 28 psi) and infused with a low viscosity and room temperature curing resin. Samples were removed after 24 hours.

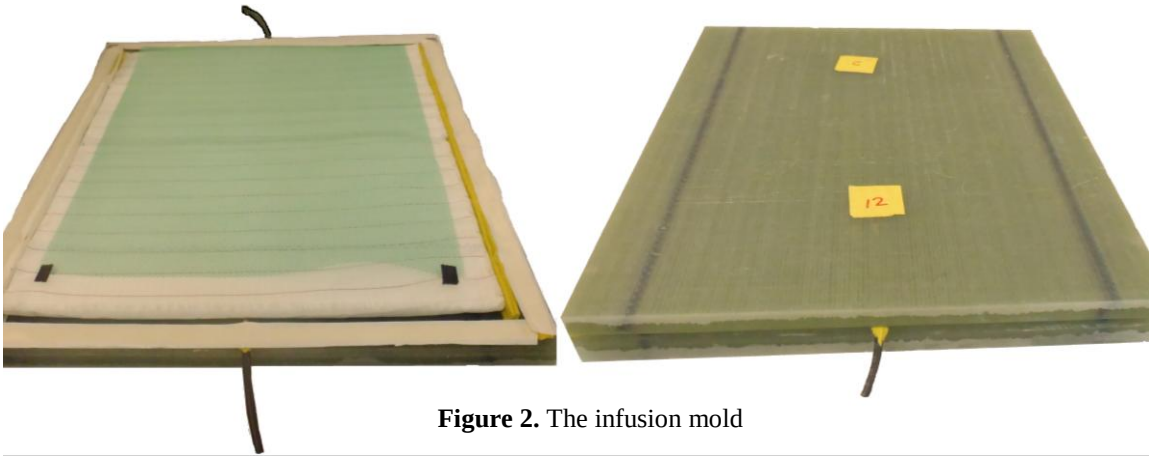

Figure 2. The infusion mold

Bag infusion

Samples were originally made in infusion molds but bag infusions yielded more constant results. For bag infusions, 10 layers of unidirectional fiberglass (18"x 24") were placed between two vacuum bags (approximate dimensions of 50" x 30") and laid flat on a table (Figure 3). Artificial waves with AR's of 12, 14, 18, and 20 were arranged at the center of the fiberglass layers. After that, all bag openings were sealed using tack tape. The system was then placed under vacuum (approximately 28 psi) and infused with resin. Samples were allowed to cure at room temperature for 24 hours.

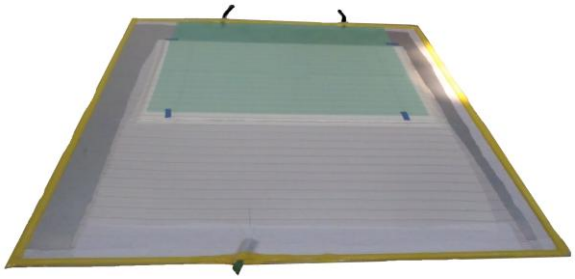

Figure 3. Bag infusion.

Compression Test Methods

The compression characteristics of a material are designed for failure testing in the absence of elastic buckling. Therefore, two different measures were taken to prevent buckling: (1) the elastic modulus of the composite material was determined through theoretical and experimental calculations and (2) an apparatus was designed to provide lateral constraint over 2 inches of the material during compression.

Theoretical elastic modulus

The rule of mixtures was used to calculate the elastic modulus of the composite material (Brondsted *et al.*, 2005). The rule states that in the longitudinal direction:

$$E_c = F_m E_m + F_r E_r \qquad (1)$$

where E_c is the elastic modulus of the composite, F_m and F_r are the fraction of matrix and fibers respectively, E_m and E_r are the respective elastic moduli of the matrix (0.42061×10^6 psi) and the fiberglass (9.427×10^6 psi). The composite material was determined to contain 55% fiberglass. Substituting into equation 1, the elastic modulus was:

$$E_c = (.55)*(9.427x10^6) + (.45)*(0.421x10^6) = 5.37 \times 10^6$$

Experimental elastic modulus

The theoretically calculated elastic modulus was compared to a value determined through tension testing. A stress vs. strain curve was plotted for tension performed on 6- 6" x 1" x 0.29" composite samples (Figure 4). The results yielded an elastic modulus of 5.86×10^6 psi.

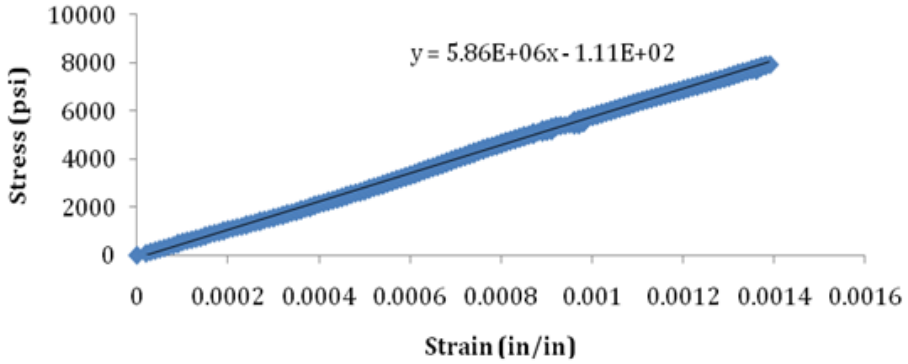

Figure 4. Stress vs strain plot

Calculating Sample dimensions for testing

In order to restrict buckling during compression, the ideal dimensions for test samples were calculated using Gerard and Becker's equation for flat plates in compression (Pollock, 1993). The equation states that the critical buckling stress is

$$\sigma_{cr} = \frac{\pi^2 k_c E}{12\,(1-\nu^2)} \left(\frac{t}{b}\right)^2 \qquad (2)$$

where σ_{cr} is the critical stress (taken to be b_f/ (a x t) for this study), E is the elastic modulus of the composite (5.86 x 10^6 psi), υ is Poisson's Ratio (0.28), a is the width of the sample, b is the length of the loaded edges (inches), t is the thickness (inches), and K_c is the compressive buckling coefficient (depending on a/b). The thickness was taken to be constant at 0.29 inches and the desired length under load was 2 inch. The critical load was substituted for 4,000 lb_f/ (a x 0.29). Therefore, solving equation 2 for a, the sample width was determined to be 0.5423 inches.

Thus, the composite dimensions to prevent buckling during compression were 6" (2 inch + 4 inches in clamps) x 0.5423" x .29" (Figure 5).

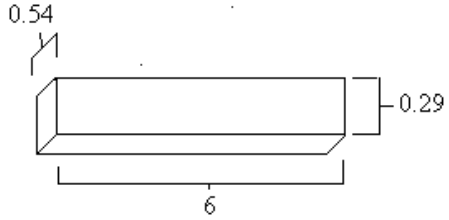

Figure 5. Dimensions of test samples

Compression analysis:

Compression analyses were performed on composite samples (control, 12 AR, 16 AR, 18 AR, and 20 AR) using an Instron testing machine (ramp rate of 0.005 inch/sec). Here, a control means a sample with the same dimensions but with no marcels. Additionally, a device (Figure 6) was modified from Mandell *et al*., (2008) to fit over the Instron compression plates and provide lateral restraint over 2 inches of the loaded edge.

Figure 6. Device designed to clamp and hold samples to Instron plates during compression.

Fatigue Testing

Fatigue testing was performed using an MTS hydraulic machine. Figure 7 illustrates how the samples were set up for testing. Samples with the same dimensions calculated above were clamped into place using the apparatus in Figure 6. The load was set to 80% of the max failure load calculated from the compression testing. Additionally, the frequency was set at 5 Hz. The test was then carried out by recording the number of cycles that samples could withstand before failure.

Figure 7. MTS setup for fatigue testing.

4. Results

After testing, stress vs strain plots were plotted for compression analysis. There were two mechanical properties that were specifically observed: the max load before failure ($\sigma_{ultimate}$) and the elastic modulus. The results for samples made in the infusion molds were relatively inconsistent. However, there was a general trend observed (Figure 8); samples containing waves with higher aspect ratios (smaller waves) had greater failure loads than samples with smaller aspect ratios (AR's). A similar trend was observed with the elastic moduli; larger AR's led to higher elastic moduli (Figure 9). There was a minor exception to the previous assertions. AR 14 had a greater failure load and elastic modulus than samples containing smaller waves (Figure 8 & 9). This result was attributed to poor infusion.

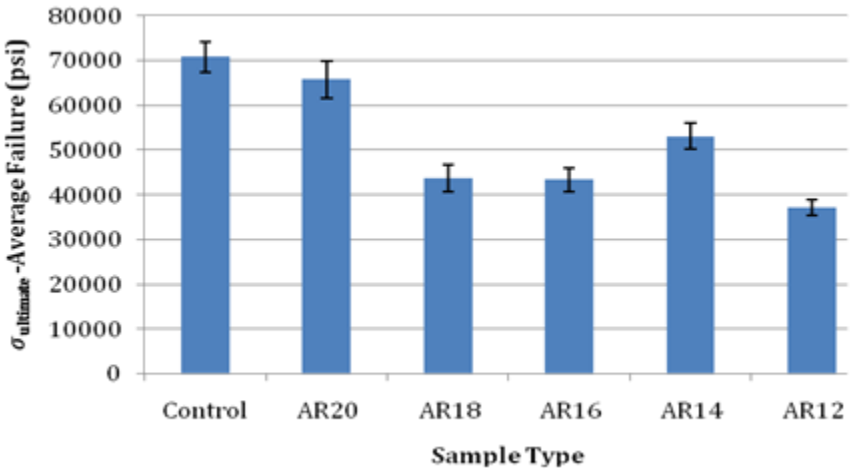

Figure 8. Average failure for samples with varying aspect ratios. Samples were made using the infusion mold.

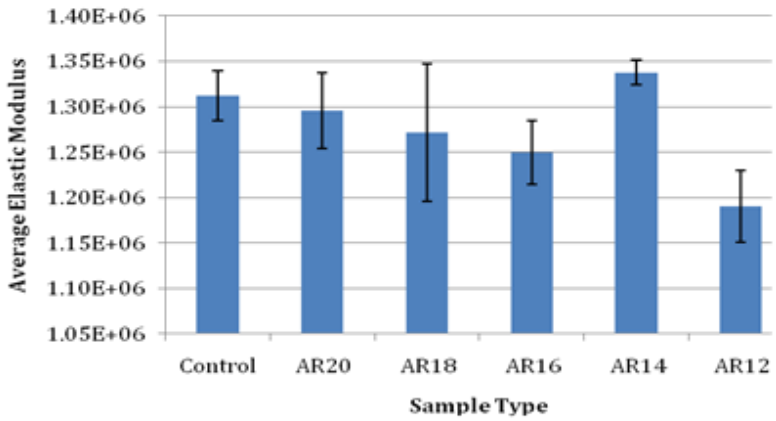

Figure 9. Average elastic modulus for samples with varying aspect ratios. Samples were made using the infusion mold.

Six separate infusions were performed to make all the test samples. Therefore, each time a new sample was made there was difficulty in ensuring that the previously made composites had the same fiber alignment and ratio of epoxy to fiberglass. By making the composite material in one large vacuum bag containing ten layers of fiberglass (dimensions 25" x 30") with aspect ratios of 20, 18, 14, and 12, the only property changing in all the samples was the wave (Figure 3). This method yielded more reliable results; full data from these tests are shown in Appendix 3. For analysis purposes, average failure loads and elastic moduli were calculated and are presented in Figure 10 and 11. The failure loads were correlated to a log curve while the elastic moduli were correlated to a linear curve (Figure 10 & 11). The controls had an average failure load of 73,000 psi whereas the AR 12 samples had a failure load of approximately 34,000 psi (represents a 47% decline in failure load strength). Additionally, the largest elastic modulus was observed in the control samples (1.30E+06) and the lowest (1.11E+06) in AR12 (Figure 11; Appendix 2). There was also a consistent type of break observed in all tests (Figure 12). All the samples with marcels broke around the wave at a 45 degree angle, whereas most of the control samples experienced crushing on one end. There were also 3 controls that broke at a 45 degree angle within the compression clamps.

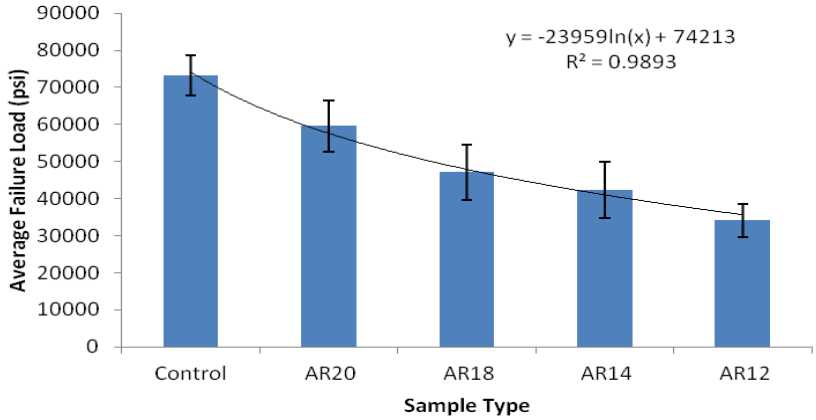

Figure 10. Average failure for samples with varying aspect ratios. Samples were made using the vacuum bag.

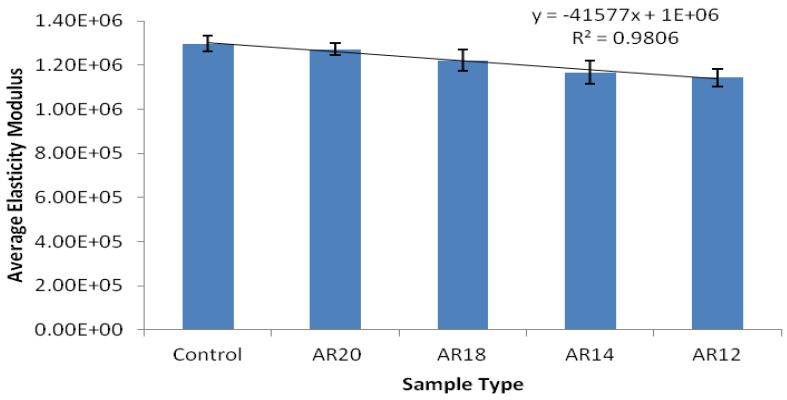

Figure 11. Average elastic modulus for samples with varying aspect ratios. Samples were made using the vacuum bags.

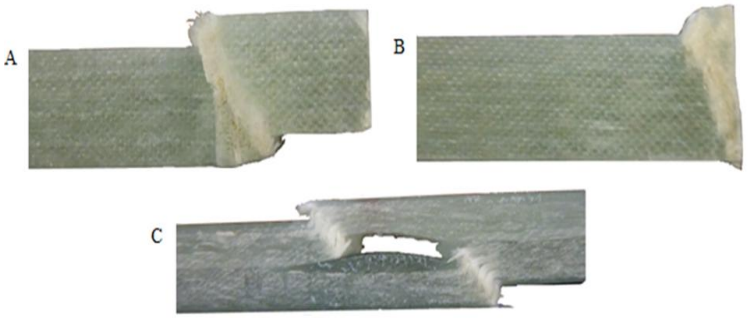

Figure 12. Shows the types of breaks observed during testing. Figure A and B show the stop view of different control sample breaks whereas Figure C shows a side view of a common marcel break.

Fatigue testing was performed on AR12 and AR 14 samples by recording the number of cycles that they were able to withstand at 80% of the AR 12 average max failure load (34147 psi). It appears that both AR 12 and AR 14 samples are able to bear a similar amount of fatigue cycles at the tested load (Figure 13). However, the overlap in error bars suggests that the results are inconclusive. Fatigue testing was also performed on AR18, AR 20, and control samples by recording the number of cycles those samples were able to withstand at 80% of the AR 18 average max failure load (49000 psi). All the wave samples had catastrophic failure and broke at a 45 degree angle around the wave (Figure 15 & Figure 16). Judging by the results observed in the compression testing, AR 18 samples were expected to have a shorter fatigue life than AR 20 samples at 49000 psi; AR 18 samples broke around 48000 psi whereas AR 20 samples broke around 59000 psi during compression testing. However, fatigue testing showed that AR 18 and AR 20 samples both broke around 500 cycles (Figure 14). In contrast, control samples never showed any signs of failure after 25000 cycles. Similar to the AR 12 and AR 14 results, the overlap in the AR 18, AR 20, and control data suggests the results are inconclusive.

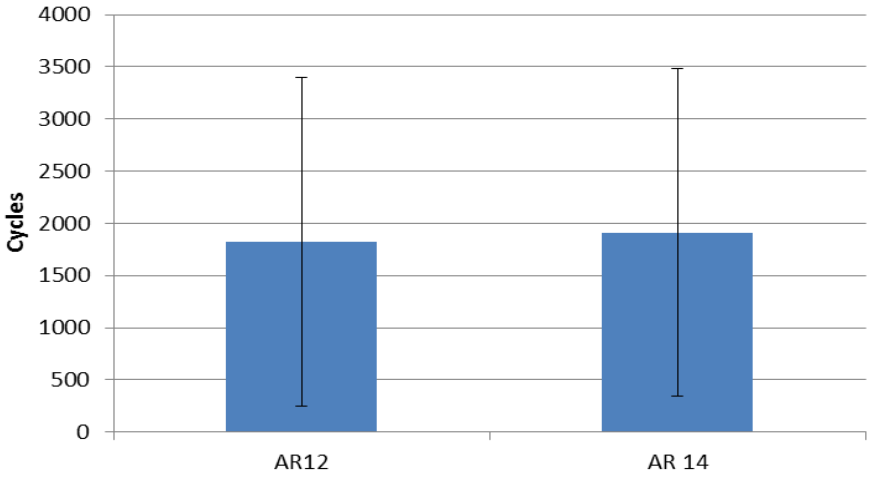

Figure 13. Number of cycles to failure at 80% of AR 12 average max failure load (34,147 psi)

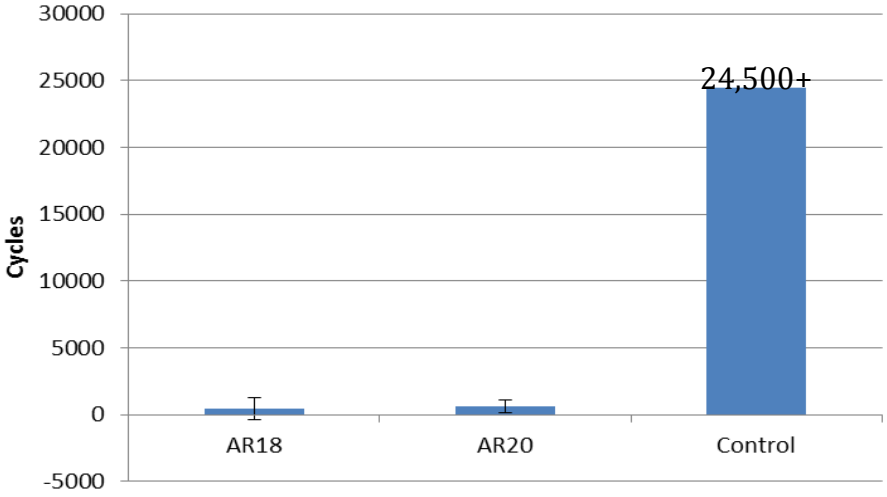

Figure 14. Number of cycles to failure at 80% of AR 18 average max failure load (49,000 psi)

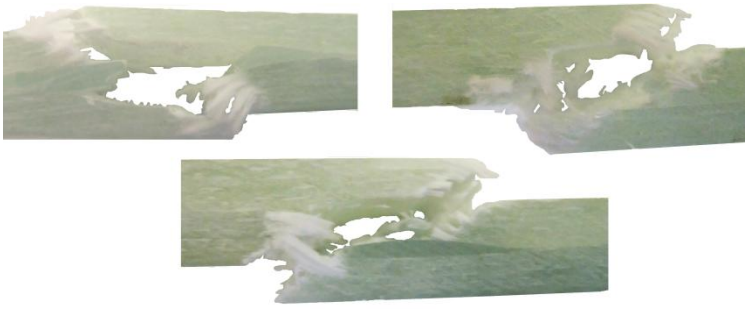

Figure 15. Types of failures observed in fatigue testing. Top left: AR 14 sample; Top Right: AR sample; Bottom: AR 18 sample

Figure 16. AR 12 sample clamped into place during fatigue testing. The illustration shows a failure around the wave.

5. Interpretation of Results

Overall, the results indicated that compressive strength decreases as the AR decreases. According to Yerramalli *et al* (n.d), lower aspect ratios could cause a 40% decline in compressive strength; a similar result was observed in this study. Samples with an AR 12 wrinkle were 47% weaker than control samples. Furthermore, the compressive strength of a composite can be represented by the equation:

$$y = -23959 \ln(x) + 74213$$

The previous equation may be beneficial in understanding the loads that marcels can withstand or what size marcels are acceptable for meeting blade performance expectations. An equation was also derived relating elasticity modulus to AR:

$$y = -41577x + 1E+06$$

Elasticity is the ability of a material to return to its original state after being stretched (Pavement interactive, 2007). Therefore, larger wrinkles (AR 12) have permanent damage at lower stresses than composites with smaller wrinkles (Figure 10).

According to this research, there may be composites containing small wrinkles that are satisfactory for wind blades. The overlap in error bars between the control and AR 20 samples suggests that there is similarity between the control's and AR 20's compressive strength (Figure 8 & Figure 10). However, there is a distinct difference in strength when comparing, the controls to the rest of the AR's; the control's failed at 73,000 psi (5,400 standard deviation) and AR 18's failed at 47,000 (standard deviation 7,500). Therefore, waves with any AR smaller than 20 may be unacceptable for blade manufacturing. In order to improve these results, compression analysis should be performed on composites containing AR's larger than 20; for instance, AR 25 or AR 30 should be studied. Additionally, statistical analysis could be used for concluding if there are any AR's that have a compressive strength that is statistically the same as the control. This would give more credibility to these results and also help determine if there is a wrinkle size that doesn't contribute to a decrease in strength.

Another important factor is the fatigue life of composites. Fatigue results showed that composites without waves have a longer life than composites containing waves (Figure 14). However, the fatigue data was generally inconclusive when comparing fatigue life between samples containing waves (Figure 13 & Figure 14). There were several reasons for the observed results. First, due to material availability, samples had to be made in multiple separate bag infusions. Visibly, the composites looked the same, but they may have contained different epoxy to fiber ratios, fiber alignment, *etc.* More reliable results would be expected by using samples made in one bag infusion. Also, this project was performed under time constraints. Therefore, there was difficulty in performing long fatigue tests. Wind turbines typically face 10^8-10^9 fatigue cycles over their lifespan. A study by Mendal *et al.* (2003), showed that a sample made of fiberglass, stitched straight strands, and polyester resin broke around 570 MPa (82,000 psi) under compression; the sample was able to tolerate about 1×10^4 cycles at 400 MPa (58015 psi) and about 1×10^6 cycles at 350 MPa (50000 psi). By lowering the R value to 0.6-0.75 for this study, longer fatigue cycles and more reliable results may be observed.

There was a frequent break observed in samples during fatigue and compression testing (Figure 12 & Figure 15). Samples tended to break at a 45 degree angle – a

characteristic of compression failure. For compression testing, the breaks tended to originate as a kink at the interface of the marcel edge and fiberglass; the first failure was also the final failure. In contrast, during fatigue testing, there were a few cases where samples would crack at the corners of the wave/fiberglass interface before failing catastrophically. These microscopic cracks were not observed until later in the study and complete analyses of the fractures were neglected. For crack identification, fatigue testing should be combined with nondestructive evaluation every 3000 - 5000 cycles to identify fractures before final failure. Failure should also be defined as a lowering of material stiffness by 5-10 %. This will help account for material cracking or small deformations that aren't catastrophic.

Conclusions

Because of the importance of productive and longer-lived blades, material defects need to be studied in composites. Additionally, for cost reduction and performance measures, the sizes of marcels in blades need to be classified as acceptable or unacceptable. Two equations were developed for predicting the effect of wrinkle size on compressive strength and elasticity. Compressive strength significantly decreased as the wave size increased. However, judging by their strength, AR's of 20 or higher may be acceptable for wind turbine blades. Further analysis on fatigue life and compressive strength of AR's above 20 may be important in resolving what size marcels are suitable for blades.

Acknowledgements

Support for this research was provided by a National Science Foundation Research Experience for Undergraduates site program in Wind Energy Science Engineering and Policy (WESEP) at Iowa State University.

References

Adams, D., & Bell, S. (1994). Compression strength reductions in composite laminates due to multiple-layer waviness. *Composites science and Technology, 53*, 207-212.

Brondsted, P., Lilholt, H., & Lystrup, A. (2005). Composite materials for wind power turbine blades. *Annual Review of Materials Research*. *35*, 505–38.

Chakrapani, S. K., (2011). Investigation of ply waviness in wind turbine blades: Experimental and numerical analysis. *Theses and Dissertations.* Paper10175. Retrieved from http://lib.dr.iastate.edu/etd/10175

Esteban, M. D., Diez, J. J., López, J. S., & Negro, V. (2011). Why offshore wind energy? *Renewable Energy, 36*(2), 444-450.

Hayman, B., Wedel-Heinen, J., & Brondsted, P. (2008). Materials challenges in present and future wind energy. *Harnessing Materials for Energy, 33,* 343-353.

Mandell, J. F., Samborsky, D. D., & Agastra, P., (2008). Composite materials fatigue issues in wind turbine blade construction. Retrieved from http://www.coe.montana.edu/composites/documents/SAMPE%202008.pdf

Mandell, J. F., Samborsky, D. D., & Wang, L. (2003). Effects of fiber waviness on composites for wind turbine blades. Retrieved from http://www.coe.montana.edu/composites/documents/SAMPE%202003%20paper.pdf

Mandell, J. F., Samborsky, D.D., Wang, L., & Wahl, N. K. (2003). New Fatigue Data for Wind Turbine Blade Materials. Retrieved from http://www.coe.montana.edu/composites/documents/AIAA_2003_0692.pdf

Murri, G. B. (1999). Influence of ply waviness on fatigue life of tapered composite flexbeam laminates. Retrieved from ntrs.nasa.gov/archive/nasa/casi.ntrs.../20000017962_2000015190.pdf

Panwar, N. L., Kaushik, S. C., & Kothari, S. (2011). Role of renewable energy sources in environmental protection: A review. *Renewable and Sustainable Energy Reviews, 15*(3), 1513-1524.

Pavement Interactic (2007). Elastic modulus. Retrieved from http://www.pavementinteractive.org/article/elastic-modulus/

Pollock, T. (1992). Introduction to Buckling. Retrieved from http://aeweb.tamu.edu/haisler/aero405/Lecture_Notes/A11_Introduction_to_Buckling_by_Pollock.PDF

Roylance, D. (2001). Stress-Strain Curves. Retrieved from *web.mit.edu/course/3/3.11/www/modules/ss.pdf*

Şahin, A. D. (2004). Progress and recent trends in wind energy. *Progress in Energy and Combustion Science, 30*(5), 501-543.

U.S. Department of Energy (2008). 20 % wind energy by 2030. Retrieved from http://www.20percentwind.org/

Varun, Prakash, R., & Bhat, I. K. (2009). Energy, economics and environmental impacts of renewable energy systems. *Renewable and Sustainable Energy Reviews, 13*(9), 2716-2721.

Veers, P., Ashwill, T. D., Sutherland, H. J., Laird, D. L., Lobitz, D. W., Griffin, D. A., Mandell, J. F., Musial, W., Jackson, K., Zuteck, M., Miravete, A., Tsai., S., & Richmon, J. L. (2003). Trends in the Design, Manufacture, and Evaluation of Wind Turbine Blades. *Wind Energy, 6*, 245-259.

Yerramalli, C. S., Miebach, T., Chandraseker, K., & QuekFiber, S. C., (n.d.).

Fiber waviness induced strength knockdowns in composite materials used in wind turbine blades. Retrieved from http://www.ewec2010proceedings.info/allfiles2/143_EWEC2010presentation.pdf

Appendices

Appendix 1: Results from compression test 1 using the infusion molds.

Sample (Sample #-AR)	Max Failure (PSI)	Elasticity Modulus (E)	Sample (Sample #-AR)	Max Failure (PSI)	Elasticity Modulus (E)
C2	69982.91674	1.35E+06	T3-12	39203.17845	1.27E+06
C3	71158.45896	1.29E+06	T4-12	36108.43429	1.18E+06
C4	69518.24725	1.33E+06	T5-12	35613.00643	1.14E+06
C5	67368.54224	1.26E+06	T6-12	34191.15541	1.16E+06
C6	71558.84594	1.30E+06	T7-12	37834.988	1.22E+06
C7	66201.39919	1.33E+06	T8-12	37804.42445	1.18E+06
C8	72864.35027	1.31E+06	T9-12	35948.20995	1.22E+06
C9	70957.06747	1.30E+06	T10-12	37862.57174	1.16E+06
average	69951.22851	1.31E+06	average	36820.74609	1.19E+06
Stdev	2218.74465	2.69E+04	Stdev	1621.277452	4.14E+04
T1-14	49181.70687	1.36E+06	T1-18	47187.54008	1.33E+06
T2-14	55413.83959	1.34E+06	T2-18	45003.39223	1.24E+06
T3-14	57090.79384	1.34E+06	T3-18	44152.69347	1.31E+06
T4-14	53078.77639	1.34E+06	T4-18	40404.68021	1.08E+06
T5-14	53399.14473	1.32E+06	T5-18	48020.10493	1.32E+06
T6-14	50486.74576	1.33E+06	T6-18	38534.88792	1.31E+06
average	53108.5012	1.34E+06	T7-18	46151.92944	1.32E+06
Stdev	2951.335706	1.37E+04	T8-18	44485.84575	1.23E+06
T1-16	41406.15605	1.31E+06	T9-18	41780.87676	1.28E+06
T2-16	43284.83701	1.25E+06	T10-18	41981.72343	1.30E+06
T3-16	43803.33224	1.30E+06	average	43770.36742	1.27E+06
T4-16	44483.57076	1.22E+06	Stdev	3045.634846	7.59E+04
T6-16	47274.27094	1.23E+06	T1-20	70063.35967	1.29E+06
T7-16	45793.3156	1.27E+06	T2-20	62277.75524	1.28E+06
T8-16	45983.60995	1.25E+06	T3-20	58821.19526	1.26E+06
T9-16	38660.65077	1.21E+06	T4-20	69004.30658	1.29E+06
T10-16	43039.47727	1.26E+06	T5-20	69380.96835	1.34E+06
T11-16	40359.91962	1.20E+06	T6-20	72058.80056	1.32E+06
average	43408.91402	1.25E+06	T7-20	62198.72839	1.37E+06
Stdev	2678.539317	3.50E+04	T8-20	64386.47381	1.26E+06
			T9-20	64419.79603	1.30E+06
			T10-20	65396.37522	1.23E+06
			average	65800.77591	1.30E+06
			Stdev	4197.681136	4.13E+04

Appendix 2: Results from compression test 2 and 3 using the vacuum bags for infusion.

Sample (Sample #-AR_Test)	Max Failure (psi)	Elasticity Modulus (E)
C1_TST2	72399.3019	1.30E+06
C2_TST2	74434.45323	1.34E+06
C3_TST2	71500.43297	1.30E+06
C4_TST2	65666.39037	1.25E+06
C5_TST2	72407.64186	1.30E+06
C6_TST2	62672.92098	1.33E+06
C7_TST2	71743.0815	1.27E+06
C1_TST3	82360.5019	1.34E+06
C2_TST3	76466.57976	1.24E+06
C3_TST3	71989.82565	1.27E+06
C4_TST3	70643.62606	1.27E+06
C5_TST3	77988.41785	1.34E+06
C6_TST3	80372.18614	1.31E+06
average	73126.56617	1.30E+06
stdev	5418.045732	3.43E+04
T1-14_TST2	38130.09823	1.17E+06
T2-14_TST2	37266.68215	1.15E+06
T3-14_TST2	30469.66472	1.10E+06
T4-14_TST2	38003.64941	1.16E+06
T5-14_TST2	37493.17523	1.14E+06
T6-14_TST2	36527.24045	1.13E+06
T7-14_TST2	32297.03139	1.13E+06
T8-14_TST2	34838.50539	1.16E+06
T1-14_TST3	49358.25982	1.24E+06
T2-14_TST3	52536.57944	1.28E+06
T3-14_TST3	53664.61864	1.19E+06
T4-14_TST3	47736.02587	1.19E+06
T5-14_TST3	52281.74067	1.23E+06
T6-14_TST3	47359.06365	1.20E+06
T7-14_TST3	46018.39419	1.10E+06
T8-14_TST3	43909.73951	1.09E+06
average	42368.1543	1.17E+06
stdev	7607.82765	5.27E+04

Sample (Sample #-AR_Test)	Max Failure (psi)	Elasticity Modulus (E)
T1-12_TST2	35538.13	1.13E+06
T2-12_TST2	28802.5	1.12E+06
T3-12_TST2	26750.83	1.08E+06
T4-12_TST2	31198.13	1.08E+06
T5-12_TST2	37108.69	1.12E+06
T6-12_TST2	28768.51	1.08E+06
T7-12_TST2	33200.77	1.15E+06
T8-12_TST2	27042.58	1.12E+06
T1-12_TST3	40009.53	1.18E+06
T2-12_TST3	40624.48	1.17E+06
T3-12_TST3	33801.64	1.17E+06
T4-12_TST3	37260.6	1.16E+06
T5-12_TST3	38308.34	1.18E+06
T6-12_TST3	38048.59	1.16E+06
T7-12_TST3	34376.82	1.18E+06
T8-12_TST3	35513.9	1.20E+06
average	34147.13	1.14E+06
stdev	4498.646	3.88E+04
T1-18_TST2	42895.24	1.24E+06
T2-18_TST2	48007.85	1.21E+06
T3-18_TST2	38642.69	1.14E+06
T4-18_TST2	40665.15	1.21E+06
T5-18_TST2	42843.74	1.19E+06
T6-18_TST2	38723.4	1.17E+06
T7-18_TST2	39301.88	1.18E+06
T8-18_TST2	35862.67	1.13E+06
T1-18_TST3	51996.96	1.26E+06
T2-18_TST3	61499.3	1.24E+06
T3-18_TST3	48666.97	1.24E+06
T4-18_TST3	56428.49	1.27E+06
T5-18_TST3	47752.83	1.26E+06
T6-18_TST3	52995.29	1.28E+06
T7-18_TST3	52583.29	1.26E+06
T8-18_TST3	54721.05	1.27E+06
average	47099.17	1.22E+06
stdev	7531.855	4.74E+04

Sample (Sample #-AR_Test)	Max Failure (psi)	Elasticity Modulus (E)
T1-20_TST2	66392.41	1.28E+06
T2-20_TST2	55146.49	1.27E+06
T3-20_TST2	68035	1.30E+06
T4-20_TST2	57869.09	1.26E+06
T5-20_TST2	51404.06	1.19E+06
T6-20_TST2	56847.7	1.26E+06
T7-20_TST2	51815.65	1.26E+06
T8-20_TST2	46535.69	1.28E+06
T1-20_TST3	66596.31	1.28E+06
T2-20_TST3	61980.37	1.30E+06
T3-20_TST3	56528.33	1.24E+06
T4-20_TST3	58019.98	1.29E+06
T5-20_TST3	56074.26	1.28E+06
T6-20_TST3	65438.51	1.28E+06
T7-20_TST3	64229.66	1.31E+06
T8-20_TST3	71078.63	1.29E+06
average	59624.51	1.27E+06
stdev	6891.468	2.81E+04

Appendix 3: Results from compression test 2 using the vacuum bags for infusion. The following 5 graphs plot stress vs strain for samples containing waves with different aspect ratios.

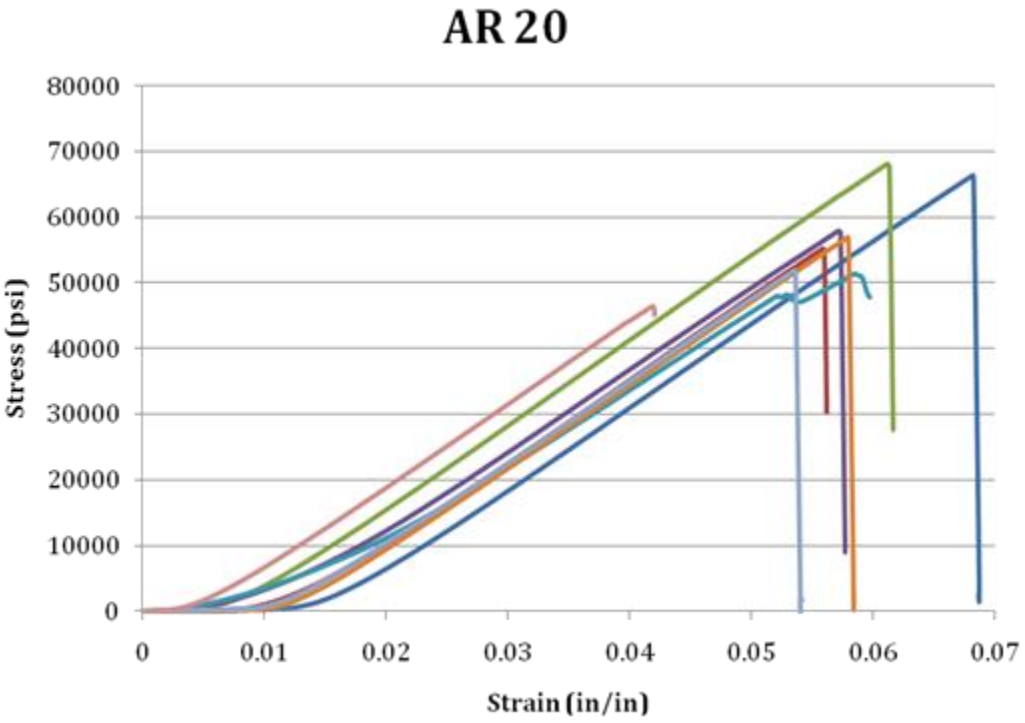

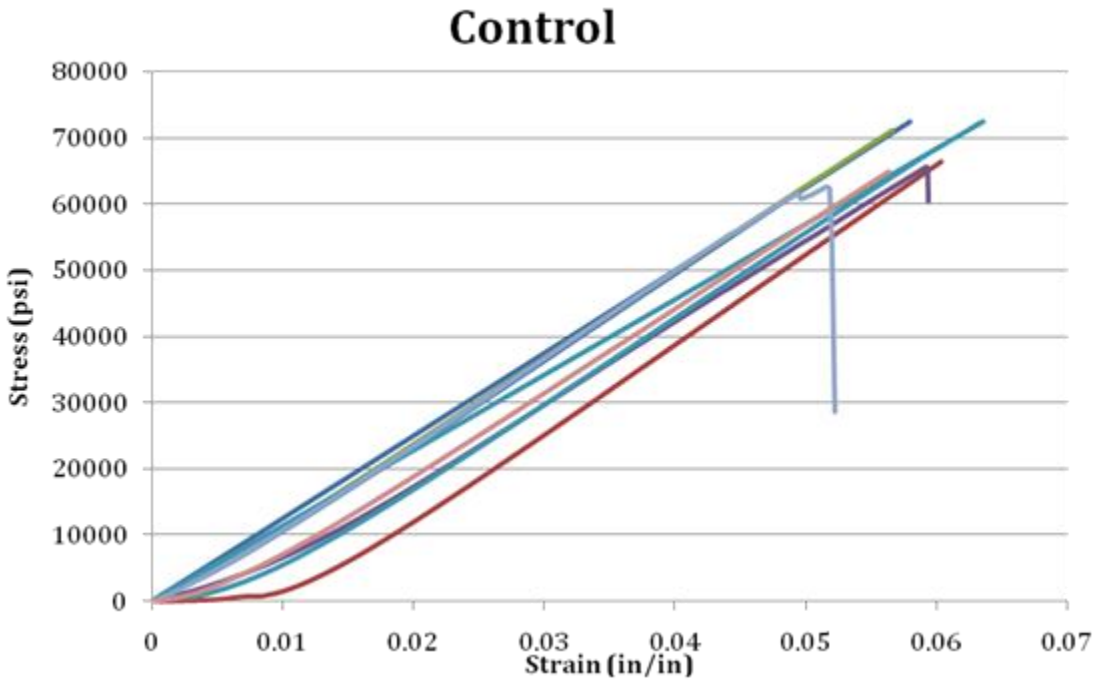

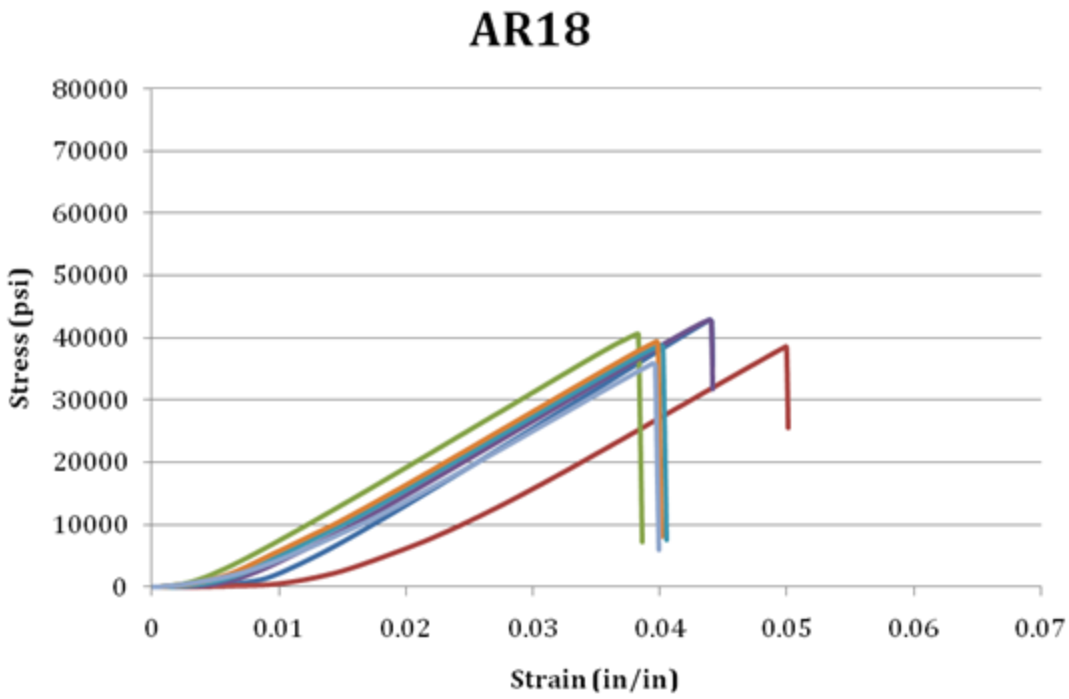
AR18
80000
70000
60000
50000
40000
30000
20000
10000
0
Stress (psi)
0
0.01
0.02
0.03
0.04
0.05
0.06
0.07
Strain (in/in)

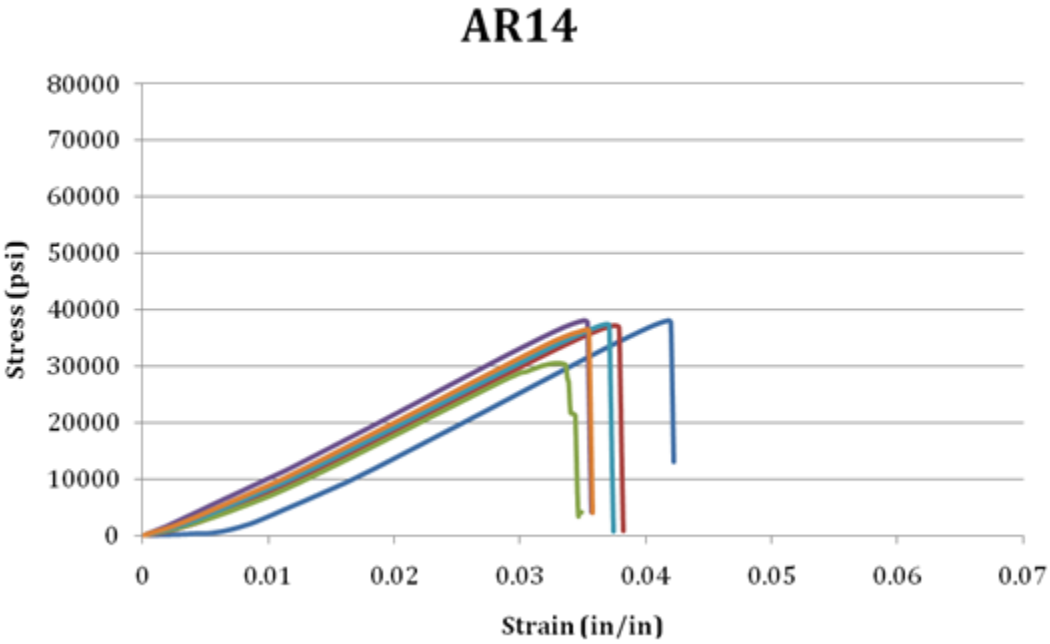
AR14
80000
70000
60000
50000
40000
30000
20000
10000
0
Stress (psi)
0
0.01
0.02
0.03
0.04
0.05
0.06
0.07
Strain (in/in)

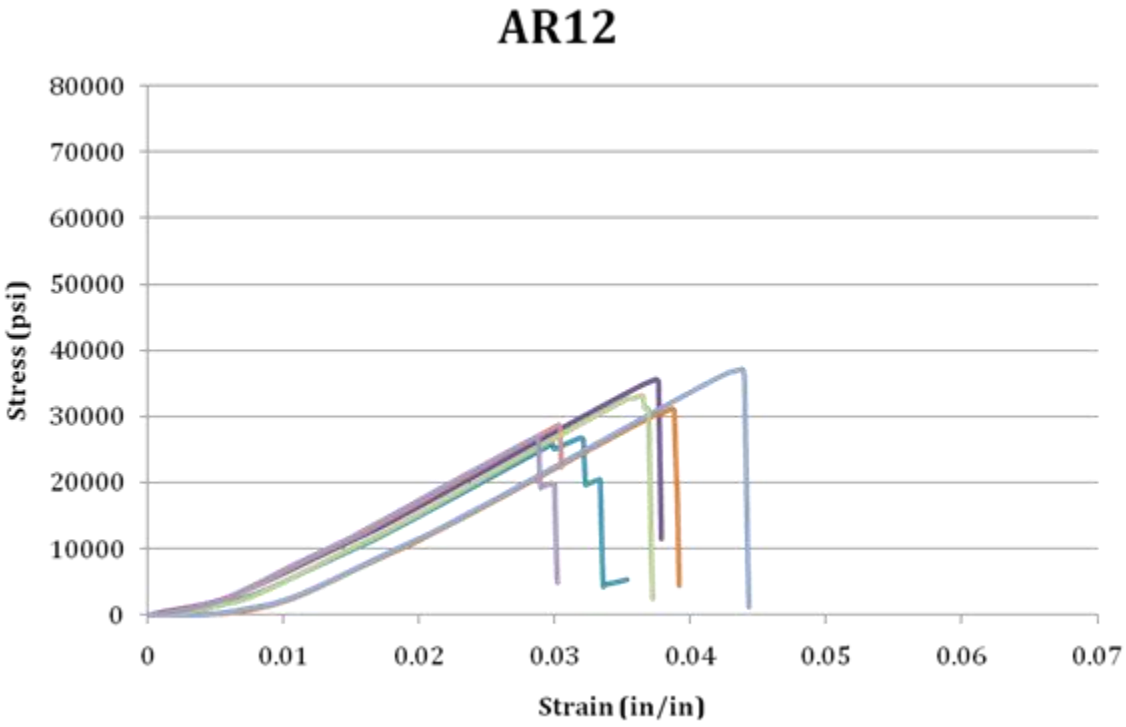
AR12
80000
70000
60000
50000
40000
30000
20000
10000
0
Stress (psi)
0
0.01
0.02
0.03
0.04
0.05
0.06
0.07
Strain (in/in)

Analysis of Biorenewable Precursor Fibers Formed From Blending Polylactic Acid, Butyrated Lignin, and Grafted Lignin

EDWARD J. ANGUS
Wind Energy Science Engineering and Policy REU, Iowa State University, Ames, Iowa
Mentors: Michael Kessler, Mahendra Thunga, and Gauri Ramasubramanian

Abstract

A lignin based blended copolymer is examined as a low cost, renewable material for the manufacture of precursor fibers to be converted into carbon fibers. These fibers have potential applications in composite materials in wind turbines. Lignin was chemically modified by a process called butyration and copolymerized with L-lactide forming polylactic acid (PLA) in a microcompounder. This grafted lignin was then blended with more butyrated lignin and purchased PLA to form samples with the following overall ratios of butyrated lignin to PLA: 1/2, 1/1, and 2/1. The different blends were melt extruded along with two other samples of grafted lignin and polymerized PLA from L-lactide. It was found that high quality continuous spools of fine precursor fiber with more than fifty percent lignin by weight could be made. These samples were analyzed by thermo-mechanical analysis and scanning electron microscopy (SEM). Finally, the fibers were thermally stabilized and carbonized. The finished carbon fibers were examined with SEM to characterize their structure.

1. Introduction

Carbon fibers possess unique properties that make them attractive for use in composites that are both high in strength and toughness, while being lightweight. Carbon fiber composites are already used extensively in aerospace applications and are being considered for use in the construction of blades for wind turbines as turbine dimensions are increased. Currently, carbon fibers are produced by the carbonization of precursor fibers extruded from either pitch or polyacrylonitrile (PAN). The process of manufacturing and carbonizing these precursor fibers is both expensive and not environmentally sustainable due to the high cost and chemical makeup of these materials [1]. Thus there is an effort to produce precursor fibers from readily available and renewable wood lignin, a byproduct of pulping process of the paper industry [2]. The ultimate aim of the project is to develop precursor fibers produced from various blends of chemically modified lignin, polylactic acid (PLA), and a PLA-lignin copolymer. Ideally, these fibers will exhibit superior mechanical and thermal properties pre-carbonization and produce a high quality and inexpensive carbon fiber when heated in a nitrogen atmosphere.

2. Literature review

The concept of manufacturing a lignin-based precursor fiber for industrial low-cost carbon fiber production is not new. The first lignin fibers for this purpose were introduced in a 1969 patent by Otani et al [3]. Numerous attempts have been made since, with varying success. Although the technical details of lignin carbon fiber production methods vary, they all share similar elements and bear the same key characteristic operations of carbon fiber production.

The distinct steps in the production of carbon fibers from any precursor material are as follows: synthesis of the fiber material, extrusion of this material into the precursor fibers, thermal stabilization of the precursor fibers, and finally carbonization of the fibers. After carbonization, the fibers must be analyzed to ensure appropriate mechanical properties for use in composites.

In the production of lignin-based precursor fibers, most of the challenge comes from synthesizing a blend or compound that is both able to be extruded into fibers that are robust while maintaining a high lignin content. The higher then lignin content, the better the yield of carbon in the finished fiber. Lignin (shown in Figure 1) is a complex, high molecular weight polymer with an aromatic structure that makes it attractive for use as a carbon fiber precursor. Its structure is composed of monolignols, three of the most common being the phenylpropane units p-coumaryl alcohol, coniferyl alcohol, and sinapyl alcohol (Figure 1) [1]. This dense structure, however, makes lignin difficult to extrude into fibers, as it lacks the necessary plasticity and thus toughness to form flexible fibers that can be manufactured to significant lengths. Many approaches have been taken to increase the plasticity of lignin, yielding promising results.

One method of increasing lignin's manufacturability is by blending it directly with a polymer to form a physical mixture that can be extruded and spooled. Upon carbonization, the polymer additive and lignin will experience thermal degradation, leaving behind a pure carbon structure due to the lignin. In this method, a greater miscibility between the lignin and polymer additive will produce a higher quality carbon fiber microstructure. It is necessary to determine the ideal ratio of lignin to plasticizer, as increasing the plasticizer

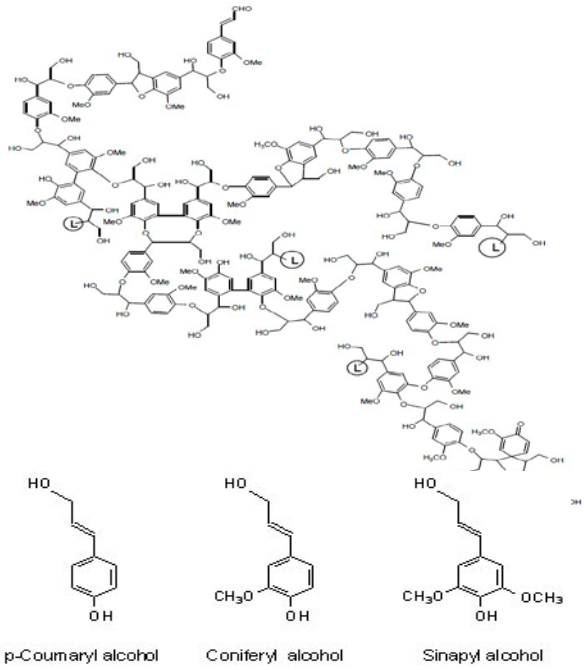

Figure 1 – Molecular makeup of softwood lignin and three common monolignols

content too much will lower the carbon content yield of the final fiber.

The work of Chen in 2012 used this method by forming physical blends of butyrated lignin and polylactic acid (PLA) [1]. Butyration was conducted in Chen's study according to previous work done by Thielemans and Wool [4]. In butyration of the lignin, hydroxyl groups in the lignin molecule were replaced by the ester group butyric anhydride (Figure 2). This increased the molecular weight of the lignin and accordingly the miscibility of the lignin and PLA. Because of the butyration procedure, Chen produced good quality lignin blends with promising properties for carbon fiber manufacture [1].

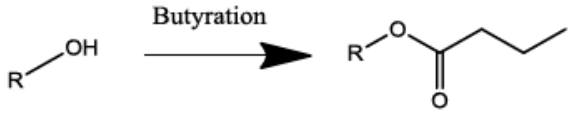

Figure 2 – Replacement of lignin hydroxyl groups with butyric anhydride

Lignin modification is not essential to this method, however. Kadla et al. [5] produced carbon fiber precursors from physical blends of unaltered hardwood kraft lignin and polyethylene glycol in different proportions, finding a ratio of 75/25 HWKL/PEO to yield good results.

Graft copolymerization of a polymer to lignin is a more sophisticated method. In this approach, a monomer is combined with a modified form of lignin that has an increased number of molecular bonding sites. The individual monomers link up with the lignin macromolecule and then polymerize with each other – leading to a high degree of integration between the lignin and plasticizing polymer. Teramoto et al. [6] readily displayed this technique with cellulose diacetate instead of lignin, grafting e-caprolactone and lactic acid onto its structure. They found that, with varying molar substitution amounts of lactic acid and e-caprolactone, the properties of the formerly brittle CDA transitioned to a highly plastic material, exhibiting a yield of nearly 70% at rupture in tensile tests.

The copolymerization method has been performed with lignin as well, with polyacrylonitrile as the copolymer in the work of Maradur et al. [7]. They showed that lignin is a viable option as a carbon fiber precursor component without notable losses in end product performance when grafted with PAN. This decreased the cost of the carbon fibers significantly by reducing the amount of the expensive PAN needed. In another study by Binh et al. [8], kraft lignin was polymerized with sebacoyl chloride to form high molecular weight thermoplastic copolyester that was capable of being melt-extruded into fibers. These fibers were thermally stable up to 200^{o}C, but no mention is made of attempts to carbonize them.

The next steps in carbon fiber production, extrusion and thermal stabilization, have also been the subjects of much research. The most common methods of producing precursor fibers from lignin have been melt spinning and wet spinning. In melt spinning, the fiber material is heated and subsequently extruded through a die. It is then spooled while cooling onto a roll which stretches the fiber, introducing a directionality into its microstructure and reducing its cross sectional area. Wet spinning is similar to melt spinning, but instead of thermal softening of the fiber material for extrusion, a solvent is used. The fiber exits the die into a coagulation bath in which it solidifies before it is spooled.

Melt spinning of lignin fibers has been shown to be effective in the work of Baker, Baker, and Gallego [9]. In their work, a twelve-hole spinneret (another name for the aforementioned die) was used to produce continuous fibers of organically purified hardwood lignin as thin as ten micrometers in diameter. Wet spinning was used in the previously mentioned Maradur study; a 150-hole spinneret was used to extrude the PAN copolymerized lignin fibers imbibed with the solvent dimethyl sulfoxide through four water coagulation baths [7]. Fiber spinning is not limited to these processes; a novel approach was taken by Ruiz-Rosas in 2009 with the electrospinning of lignin fibers, in which an electric charge was used to draw fine fibers from polar lignin based solutions [10].

Thermal stabilization has varied from study to study depending on the precise details of the chemical makeup of the precursor fibers, but its intended purpose is always the same. It serves to raise the glass

transition temperature of the fibers such that fusing is preemptively curtailed before the carbonization process. In some cases, the fibers are stretched as well during this step to further introduce directionality. The process involves ramping the temperature of the fibers at a linear rate to a specified value. Care must be taken to ensure that the thermal stabilization process is practical for industrial applications, as noted in the 2010 Baker Study. It was found that fibers produced from the organically purified hardwood lignin required a heat ramping of less than 0.05 degrees Celsius per minute to prevent fusing [9]. This slow rate of heating would lead to difficulty in the manufacture of these types of fibers on a large scale. More practical results have been had with blended and copolymerized lignin fibers; a 2002 study by Kadla et al. found that a ramping rate of at least 12°C per hour produced satisfactory stabilization [11].

The carbonization process of the precursor lignin fibers is the same in the multiple studies regardless of the chemical composition of the fibers. The fiber is heated in an inert gas, usually nitrogen, up to 1000°C at a constant rate, typically a couple of degrees per minute. What remains after this process is a fiber containing over ninety percent carbon by weight.

After carbonization, the fibers are tested to determine their mechanical properties. In several of the studies reviewed, this was done according to ASTM standard 3379 – a tensile test for determining the elastic modulus and ultimate strength of monofilament fibers [1] [9] [12]. This is accomplished by mounting the fiber to be tested on a paper tab that is then secured in a tensile testing machine. The tab is removed in the middle such that all of the subsequent stress will be handled by the fiber alone, and then the engineering stress is recorded versus recorded strain [12].

The multiple studies reviewed here contain a wide variety of processes and techniques to achieve the distinct steps in the carbon fiber manufacturing process when using lignin as a precursor. Although they differ widely on methods and outcomes, they offer an insight into potential areas of improvement in the use of lignin as a precursor fiber material.

3. Experimental methods

A physical blend of butyrated lignin, PLA, and copolymerized B-lignin/PLA represents a hybrid approach to enhancing the mechanical properties of lignin precursor fibers. It incorporates both physical blending and graft copolymerization. Finding the ideal reaction time for the copolymerization of PLA and butyrated lignin was the first step of the project. Softwood kraft lignin was purchased from Meadwestvaco Corporation and butyrated according to the same process used by Chen and described by Thielemans and Wool [4]. The butyrated lignin was then mixed with L-lactide from Purac in three samples each weighing 4.25g and with a 1-1 B-lignin/L-Lactide weight ratio. These mixtures were then loaded one at a time into a dual auger microcompounder/extruder from Daca instruments at 110^{o}C and 100 rpm with the catalyst tin (II) 2-ethylhexanoate in a quantity of 10% by weight. The subsequent copolymerization reaction is shown in figure 3. The samples were compounded for 30, 60, and 90 minutes. After extrusion, each sample was analyzed qualitatively and then on a TA Instruments AR2000ex rheometer using a torsional test. The shortest mixing time for satisfactory graft copolymerization at ~150^{o}C was determined from this rheometer data.

After finding the ideal time for complete grafting of PLA to B-lignin, three samples of 1/1 B-lignin/PLA grafted lignin, each with a mass of 1.67g, were produced. These samples were blended with PLA beads and butyrated lignin in the microcompounder in three mixtures each with a total mass of 5g at 180^{o}C. The amount of PLA beads and B-lignin was controlled so that the samples had the following overall B-lignin/PLA weight ratios: 1-2, 1-1, and 2-1. The samples were then extruded at 150^{o}C into bulk material and precursor fiber spools on an Xplore spooling machine from DSM. In addition to these samples, pure grafted lignin fibers and bulk material were produced, along with PLA bulk material polymerized from L-Lactide at 90^{o}C for 90 min in the microcompounder.

The bulk material from each blended sample as well as the grafted lignin and produced PLA was then formed into rectangular shaped samples on a compression-molding machine. Dynamic mechanical analysis was performed using a TA Instruments Q800 in three-point bending configuration on these samples to examine the storage and loss moduli and determine the glass transition temperatures (T_g) of the samples. Also, differential scanning calorimetry (DSC) was performed using a TA Instruments Q2000 on each blended sample to determine its glass transition temperature and thus PLA/lignin miscibility. Thermo gravimetric analysis (TGA) was conducted on the samples in air to test their thermal stabilities over the temperature range 20-750^{o}C and under a nitrogen atmosphere to determine the maximum carbon yields of each of the samples.

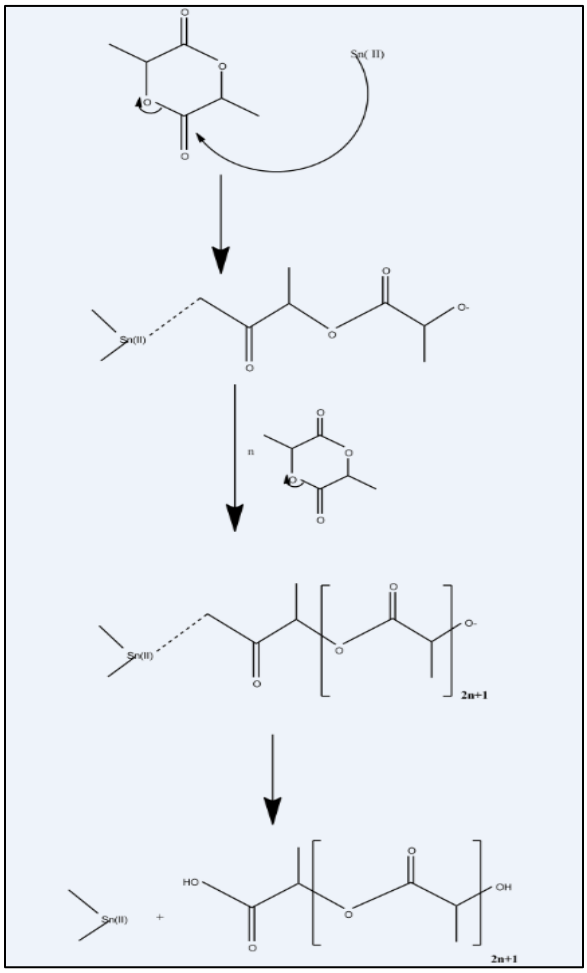

Figure 3 – Ring opening copolymerization of L-Lactide into PLA onto lignin

The spooled fiber samples were given a thermal stabilizing heat treatment in a programmable oven by heating at a rate of 3 ^{o}C min^{-1} to 105 ^{o}C, then 0.25 ^{o}C min^{-1} to 250 ^{o}C and held there for four hours. The samples were then allowed to cool to room temperature and checked to confirm that the fibers did not experience softening or fusing to one another. The samples were then carbonized by raising their temperature to 1000 ^{o}C at a rate of 3° min^{-1}. Samples of fibers from each of the blends pre-stabilization, post-stabilization, and post-carbonization were collected for morphological characterization by scanning electron microscope (SEM) and transmission electron microscope (TEM).

4. Results

The ideal time for the B-Lignin and L-Lactide to copolymerize in the microcompounder was found to be 90 min as it exhibited the most stable elastic modulus at temperatures over 125°C. The 30-min sample was obviously inadequate for processing, as fusing occurred at room temperature. Both the 60 and 90-min samples were found to be plastic at room temperature, but still exhibited evidence of polymerization at higher temperatures.

Rheological data is provided in the graph in Figure 4. It shows the storage shear modulus, G', of the three samples. It is clearly seen that the 90-min sample has the most stable storage shear modulus at a higher range of temperatures and thus is the most suitable for melt mixing with PLA. It should also be noted that the 90-min sample graph has a change in slope at ~90^{o}C that levels off near 110^{o}C, possibly indicating softening at an intermediate state and then re-polymerization upon further heating. Further rheological tests should be conducted on the 90-min grafted to determine that this is true.

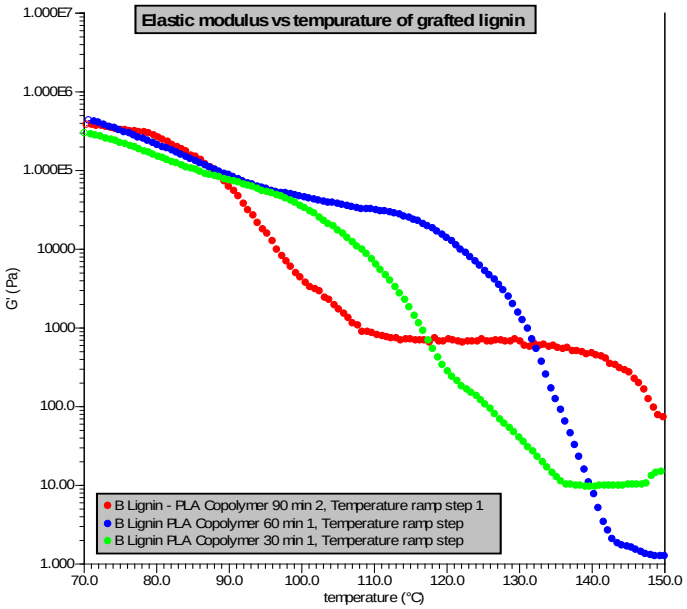

Figure 4 - Rheological storage modulus graph for copolymerized samples

Figure 5 and Table 1 show the Differential Scanning Calorimetry data (glass transition temperature, melting temperature, and crystallization temperature) of the various Lignin/PLA blends:

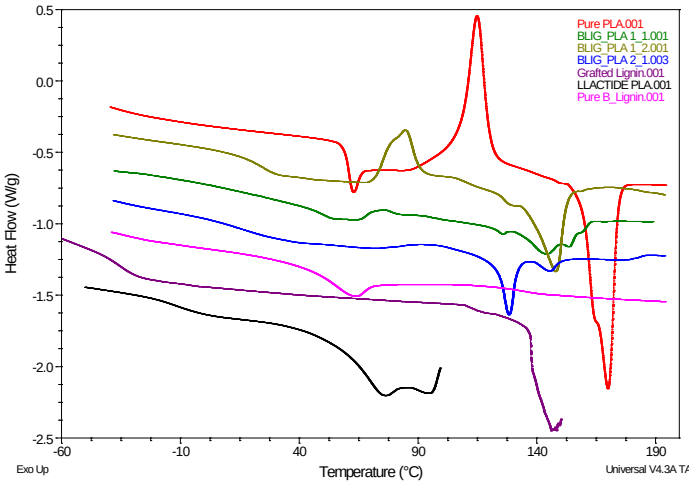

Figure 5 - DSC heat flow graph for blended samples

Table 1 - DSC data for blended samples

	Tg °C	Tm °C	Tc °C
Pure PLA	57.23	169.9	114.7
L-Lactide - PLA	-11.62	138.9	111.3
B-Lignin/PLA 1/2	24.46	147.8	84.57
B-Lignin/PLA 1/1	51.38	144.9	73.15
B-Lignin/PLA 2/1	12.82	128.1	96.78
Pure B-Lignin	39.23	60.96	//
Grafted Lignin	-35.97	146	//

Several trends are clear from the data. First, the melting temperature trough decreases in value and intensity as the proportion of B-lignin in the blend increases. The same can be said for the exothermic recrystallization peaks. The T_g temperature trough is also observed to decrease and broaden as the PLA proportion decreases, with the exception of the 1/1 sample.

Thermo gravimetric analysis data for the samples is shown in Figures 6a and 6b. The graphs are for TGA in air and nitrogen atmospheres respectively.

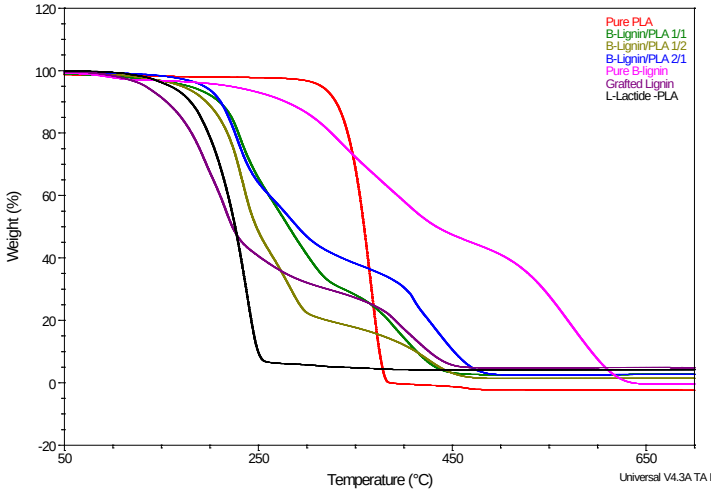

Figure 6a - TGA weight % graphs for blended samples in air atmosphere

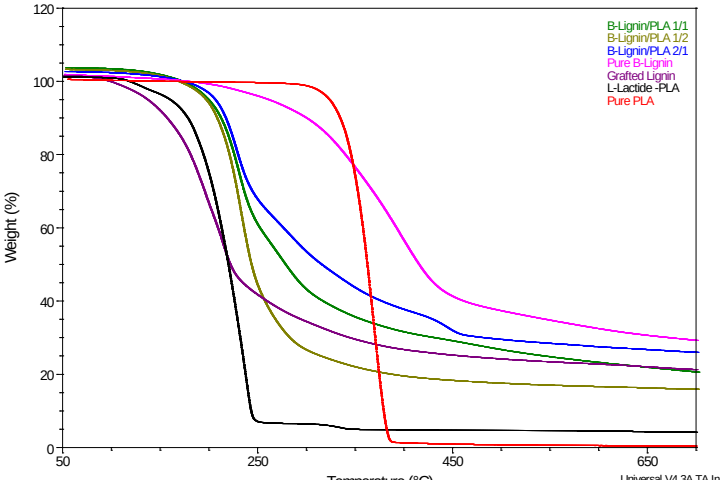

Figure 6b - TGA weight % graphs for blended samples in nitrogen atmosphere

It should be noted that in the air atmosphere TGA, all of the curves should eventually go to exactly zero, as the samples would have oxidized completely at that high of temperature. It is possible that the TGA machine was not properly calibrated, but the repeated error shown for the B-lignin/PLA blends seems to indicate something more systemic with the mixtures themselves. It is likely that the tin catalyst used left behind material that was not oxidized in each case. On the other hand, the N_2 TGA data looks good and confirms that increasing PLA yields lower carbon content, as the residual weight after carbonization increases with higher B-lignin blends.

Finally, dynamic mechanical analysis data (including T_g and storage modulus E') is shown in Figure 7 and Table 2.

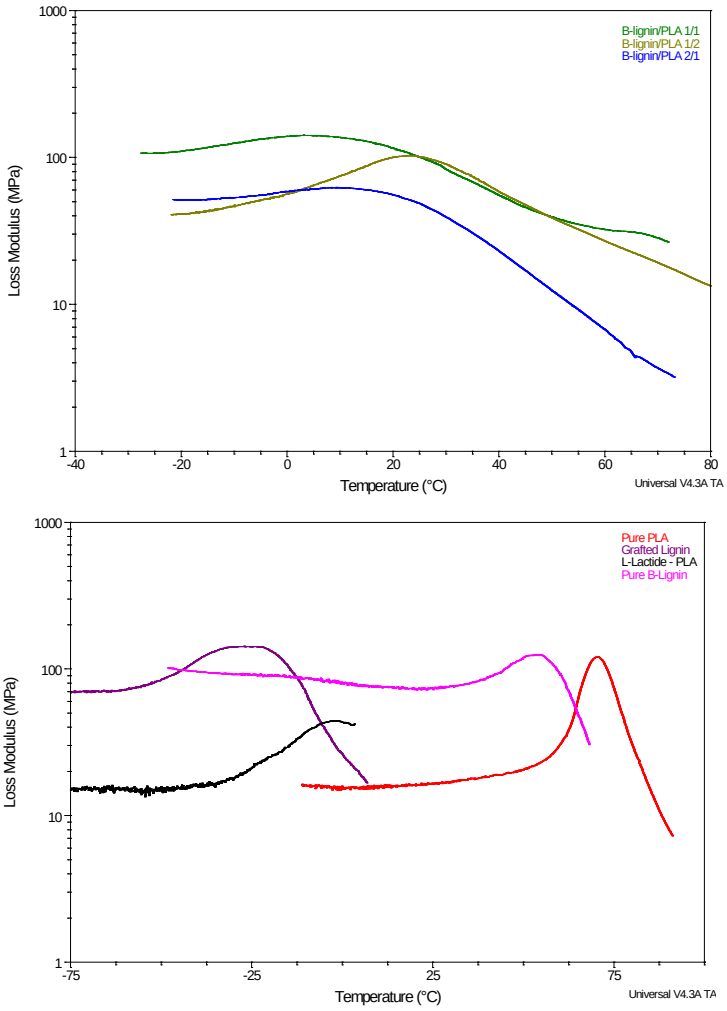

Figure 7 - DMA Loss modulus graphs for blended samples

Table 2 - DMA data for blended samples

	Tg °C	E' Mpa
Pure PLA	70.46	535.10
L-Lactide - PLA	-2.92	484.40
B-Lignin/PLA 1/2	23.27	1246.00
B-Lignin/PLA 1/1	3.10	1537.00
B-Lignin/PLA 2/1	8.30	563.30
Pure B-Lignin	54.32	1538.00
Grafted Lignin	-22.13	1758.00

The test indicates that T_g is lowered with an increase in lignin content as was shown in DSC, but the data is sporadic and varies without a clear trend as is present in DSC, showing T_g's as low as 3.10°C for one blend. Samples with internal physical defects are probably the cause for this discrepancy between DMA and DSC data, and the DMA tests should be redone with more care taken in sample quality. Despite this fault, in no place does the T_g increase with increasing lignin content, and that can be taken as a good sign of high miscibility between the lignin and PLA.

All samples proved to be easily spun into continuous fibers, including those with high lignin content (greater than fifty percent). The main hindrance in successfully obtaining a continuous spool proved be operator error, as being too quick or slow in attaching the fiber to the spooling machine led to fractures and excess accumulation of material from the extruder. With repeated trials high quality spools were produced, with particularly good results in one trial when a 1/1 B-lignin/PLA fiber was spun continuously for approximately five minutes, yielding a very fine continuous spool of fiber (Figure 8).

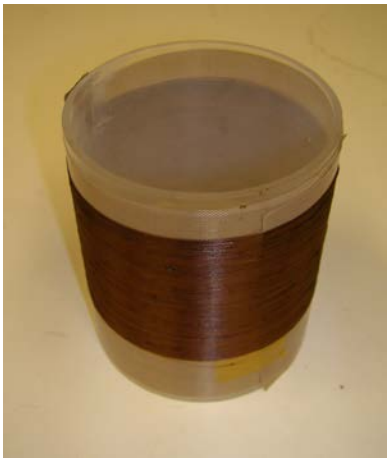

Figure 8 – 1/1 B-lignin/PLA precursor fiber spool

Figure 9 shows the B-Lignin/PLA/Copolymer blend fibers (Overall B-lignin/PLA content 1/2, 1/1, 2/1, and grafted lignin) before and after carbonization in the tray in which they were placed into a tube furnace. All of the fibers were stabilized in the manner described earlier. Only the 1/2 blend fiber was visibly compromised in structure; the PLA broke down in stabilization, yielding discontinuous fibers.

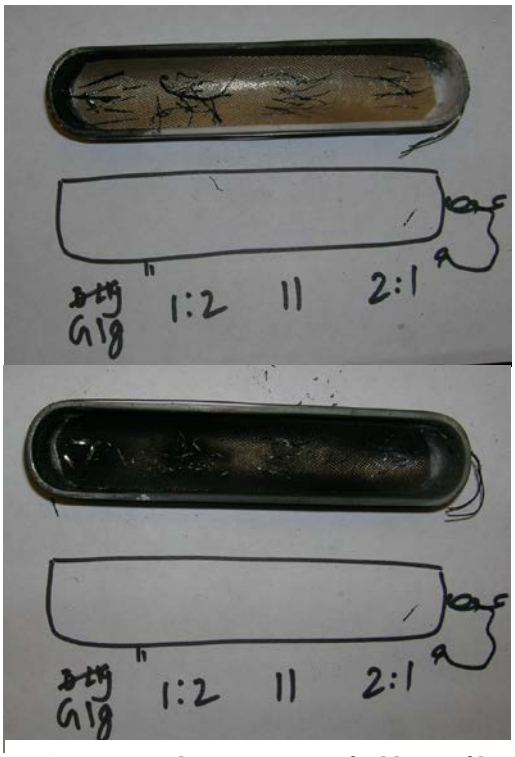

Figure 9 – B-lignin/PLA/Grafted lignin fibers before and after carbonization

As of yet, TEM images have not yet been received to characterize the morphology of the stabilized precursor and carbon fibers. SEM images are provided to characterize their structure (Figure 10).

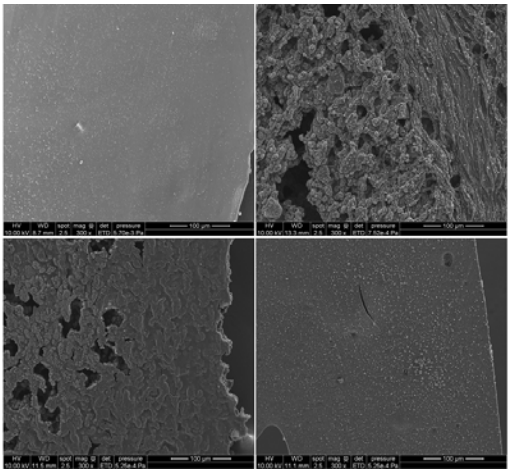

Figure 10 – SEM image of carbonized blended samples. Clockwise from top left – grafted lignin, 1/2, 2/1, 1/1

The 1/1 and 1/2 B-Lignin/PLA blend fibers exhibit significant void defects in their structure. This is due to the degradation of pockets of PLA during the carbonization process, and is indicative of a lower level of B-lignin/PLA miscibility. The pure grafted lignin and 2/1 samples show good miscibility with much smaller voids.

It is apparent in all of the SEM images that there is a crystalline substance present on the fiber surface. Preliminary analysis indicates that it is a form of carbon oxidation. A better view of one of these crystals is shown in Figure 11.

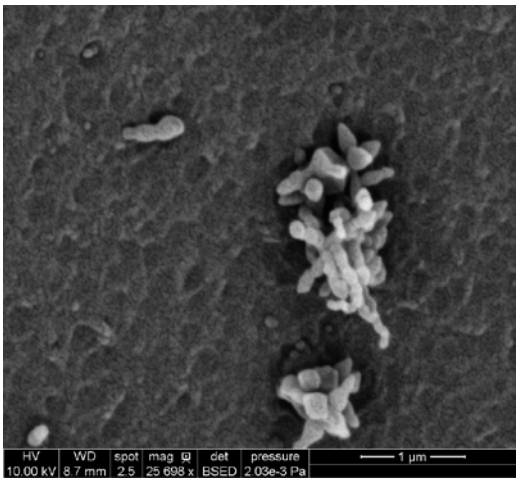

Figure 11 – SEM image of oxidation present on grafted lignin fiber surface

Another defect that was immediately visible from inspection of the post-stabilized fibers was a ribbon like structure of some of the samples. Not all of the fibers had this structure. A 1/1 fiber with good cylindrical morphology is displayed in Figure 12a, and a 1/1 fiber post carbonization with a "ribbon" form is shown in Figure 12b.

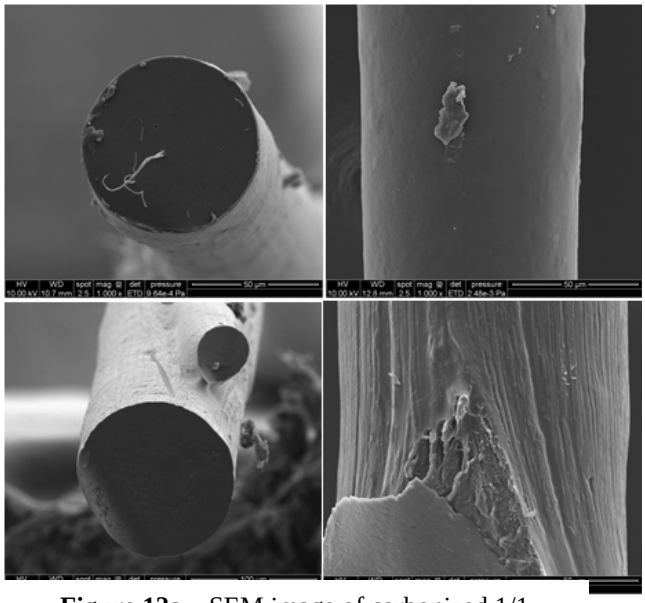

Figure 12a – SEM image of carbonized 1/1 sample, clockwise from top left: post stabilization end view and side view, Post carbonization side view and end view

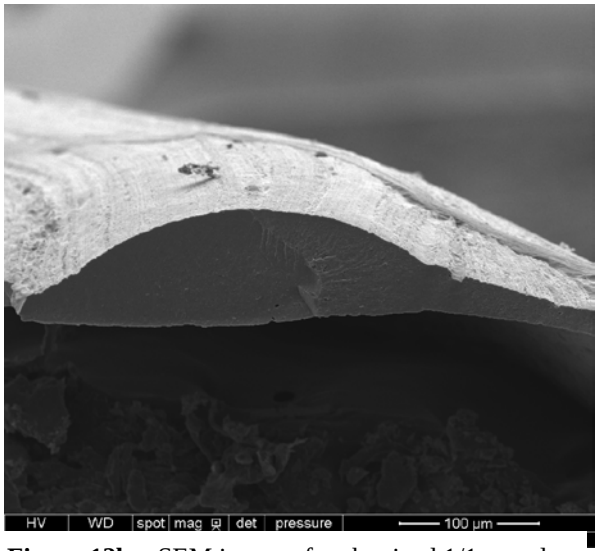

Figure 12b – SEM image of carbonized 1/1 sample, showing "ribbon" defect

5. Analysis and interpretation

It was previously noted that T_g, T_m, and T_c all decrease as the overall B-lignin content increases in the blends, although the 1/1 mixture is anomalous in having a higher T_g and T_c than predicted by this trend. Chen reported similar results in her B-Lignin/PLA blends, and observed that the lowering of melting temperature with increasing B-lignin indicated good miscibility and is usually observed in blends of crystalline polymers [1]. The DSC data clearly indicates that the L-lactide polymerized into PLA has not undergone a complete polymerization; the glass transition temperature and melting temperature are significantly lower than that of commercial PLA. The synthesized PLA also degrades at a much lower temperature than the purchased PLA – approximately 200^{o}C as compared to almost 400^{o}C. This undoubtedly is the cause for the discrepancy between the DSC and TGA data for grafted lignin and the 1/1 blend. In theory, they have an equal part of butyrated lignin and PLA, but the presence of the incompletely polymerized L-lactide causes the grafted lignin to experience a lower T_g and melting temperature Further work must be done to accurately discern the degree of polymerization in the PLA present in grafted lignin and to improve it.

TGA shows the thermo-stabilizing effect that increasing levels of PLA have on the blends. This is important in ensuring the fibers do not degrade at low temperatures in the manufacturing and stabilizing processes. As previously stated, the nitrogen atmosphere TGA is evidence of the strong connection between lignin content and subsequent carbon yield.

The peaks in the loss modulus curves of the DMA graph theoretically correspond to the glass transition temperatures of the samples. As stated earlier, there appears to

be no obvious trends in the T_g's of the samples from this data set. It is apparent from the figure that the low glass transition temperature of the L-lactide PLA and correspondingly that of the grafted lignin serve to significantly decrease the glass transition temperatures of the blended samples. The DMA tests should be conducted a second time with more carefully prepared samples to confirm that these findings are valid. Additionally, TEM data could provide insights to the structure of the grafted lignin to confirm that copolymerization occurred and also determine the degree to which the different blends are intermingling. This data may help to explain the seemingly erratic T_g values given by DMA.

In the SEM images, the darker substance present is the B-lignin, and the lighter substance is PLA. Looking at the 1/1 blend fiber, a slight directionality can be seen near the edges in which the voids are compressed and no holes left from degraded PLA are present. The 2/1 fiber has this quality throughout its structure, and because of its higher lignin content is the best quality carbon fiber produced in the study that has the potential to be manufactured en masse.

Finally, the ribbon form of the stabilized fibers retained through carbonization is most likely not due to an innate property of the fiber materials. The samples were stabilized while spooled on a quartz tube covered in a Teflon-glass composite sheet. This contact with a physical surface is the most likely cause for the fibers to have flattened out. Work must be done to devise a way to suspend the fibers such that they maintain a cylindrical directionality without being distorted or broken. Suspension of small amounts of weight from fibers during stabilization has been pursued as a possible solution, but none of the fibers have survived the process intact. The next method to try will be to produce a frame in which sections of fiber are unsupported so that their shape is unaffected.

6. Conclusions

Although much work has yet to be done to completely and accurately characterize the lignin blends to confirm appropriate thermo-mechanical characteristics, fiber morphology, and post carbonization structure, the larger objective of the project has been met. Continuous high quality spools of fibers containing over fifty percent lignin by weight were manufactured and shown to be able to survive thermo stabilization and carbonization intact without fusing or degradation. Theoretically, this process could be taken to the industrial scale, pending that a suitable blend of grafted lignin, B-lignin, and PLA is found so that the resulting carbon fibers have competitive properties.

Acknowledgements

Support for this research was provided by a National Science Foundation Research Experience for Undergraduates site program in Wind Energy Science Engineering and Policy (WESEP) at Iowa State University.

References

K. Chen, "Bio-renewable fibers extracted from lignin/polylactide (PLA) blend," M. S. Thesis, Materials Science and Engineering, Iowa State University, Ames, IA, 2012.

W. Thielemans, E. Can, S. S. Morye, R. P. Wool, "Novel applications of lignin in composite materials," Journal of Applied Polymer Science, vol. 83, pp. 323-331, 2002.

S. Otani, Y. Fukuoka, B. Igarashi, K. Sasaki, "Method for producing carbonized lignin fiber," US Patent 3,461,082; 1969.

W. Thielemans, R. P. Wool, "Butyrated kraft lignin as compatibilizing agent for natural fiber reinforced thermoset composites," *Composites: Part A*, vol. 35, pp. 327-338, 2004.

J. F. Kadla , S. Kubo, R. D. Gilbert, R. A. Venditti, "Lignin based carbon fibers," in *Chemical Modification, Properties, and Usage of Lignin*. Boston: Kluwer Academic/Plenum Publishers, 2002, ch. 7, pp 121-138.

Y. Teramoto, M. Yoshioka, N. Shiraishi, Y Nishio, "Platicization of cellulose diacetate by graft copolymerization of ἐ-caprolactone and lactic acid," *Journal of Applied Polymer Science*, vol. 84, pp. 2621-2628, 2002.

S. P. Maradur, C. H. Kim, S. Y. Kim, B. H. Kim, W. C. Kim, "Preparation of carbon fibers from a lignin copolymer with polyacronytrile," *Synthetic Metals*, vol. 162, pp. 453-459, 2012.

N. T. Thanh Binh, N. D. Luong, D. O. Kim, S. H. Lee, B. J. Kim, Y. S. Lee, J. Nam, "Synthesis of lignin-based thermoplastic copolyester using kraft lignin As a macromonomer," *Composite Interfaces*, vol. 16, pp. 923-935, 2009.

D. A. Baker, N. C. Gallego, F. S. Baker, "On the characterization and spinning of an organic-purified lignin toward the manufacture of low-cost carbon fiber," *Journal of Applied Polymer Science*, vol. 124, pp. 227-234, 2012.

R. Ruiz-Rosas, J. Bedia, M. Lallave, I. G. Loscertales, A. Barrero, J. Rodriguez-Mirasol, T. Cordero, "The production of submicron diameter carbon fibers by the electrospinning of lignin," *Carbon*, vol. 48, pp. 696-705, 2010.

J. F. Kadla, S. Kubo, R. A. Venditti, R. D. Gilbert, A. L. Compere, W. Griffith, “Lignin-based carbon fibers for composite fiber applications,” *Carbon*, vol. 40, pp. 2913-2920, 2002.

Standard Test Method for Tensile Strength and Young’s Modulus for High-Modulus Single-Filament Materials, ASTM Standard D3379, 1996.

Standard Test Method for Plastics: Dynamic Mechanical Properties: In Tension, ASTM Standard D5026, 2010.

Wind Farm Arrangement: Considering the Influence of Complex Terrain and Turbine Wake Interactions

S. ROSE EILENBERG
Wind Energy Science Engineering and Policy REU
Iowa State University
Ames, Iowa
Mentors: Dr. Hui Hu and Wei Tian

Abstract

Installed wind capacity is increasing, and as such many varied locations must be considered in siting a new wind farm. Hilly areas might be particularly appealing due to the speed-up effect of wind passing over a hill. Since the power in the wind is proportional to the cube of wind speed, a small increase in wind speed can give a large increase in output. There is, however, a decrease in wind speed before the hill associated with this increase – more must be understood about both in order to optimize wind farm siting and arrangement.

In this study, experiments were carried out on model wind turbines in a wind tunnel to investigate the effects on individual and multiple wind turbines sited in complex terrain, consisting of a two-dimensional ridge. The characteristics of the surface winds (mean velocity and turbulence profiles) were measured using a cobra probe. The force and moments as well as the output were also measured. The performance and flow characteristics on the hill were compared with those of a model on flat ground to better understand wind farm layout and design, and how to optimize power yield and improve durability. The effects of high and low turbulence in the incoming atmospheric boundary layer on the performance of the individual wind turbines were also investigated. All experiments were conducted in the Aerodynamic/Atmospheric Boundary Layer (AABL) Wind Tunnel in the Aerospace Engineering Department at Iowa State University.

Results obtained from the present study shed light on how complex dynamics of the wind farms could be affected by different factors such as the wind farm configuration, turbine spacing, incoming flow character, topography of the terrain (complex terrain) and operating conditions of the upstream turbines.

1. Introduction

In order to reach the 20% wind energy by 2030 scenario addressed by the United States Department of Energy (US DOE, 2008), there will have to be progress made in many areas of the industry to bring down costs and increase output. This paper will address two issues related to reducing the cost of wind energy. Primarily it will focus on the output effects of locating wind turbines on complex terrain, and secondarily it will consider the turbulence of the incoming flow, which causes dynamic loads on turbine blades, hence shortening their lifetime. All experiments were carried out in the Aerodynamic/Atmospheric Boundary Layer Wind Tunnel at Iowa State University.

2. Literature review

Wind is the movement of air caused by differences in air pressure. The two major factors in generating wind are the rotation of the earth (Coriolis effect) and the uneven heating of the earth's surface, which results in density gradients (horizontally and vertically). Wind turbines operate and extract energy from the atmospheric

boundary layer (ABL) — the lowest part of the atmosphere. By the definition of boundary layer flow, the ABL is highly influenced by frictional and viscous effects. Different surfaces have different effects, thus the thickness of the ABL depends on the type of terrain. The ABL is thinner over smooth surfaces such as water or ice (the lowest is about 50m thick in winter in the Arctic), and much thicker over hilly, forested or urban areas (2km in tropics). [1]

Boundary layer thickness is defined as distance from the ground to where $U\,(x,y) = 0.99\,U\,(x)$, where U (x, y) is the velocity inside the boundary layer and U (x) is the free stream velocity. The fluid velocity on the surface is zero due to the no-slip condition.

A boundary layer is characterized by strong velocity gradients, particularly the 10% closest to the surface. The velocity profile inside the boundary layer is defined by the logarithmic law, which depends on surface roughness, z_0, given in meters. [1] The velocity increases with height, z, with the logarithmic approximation $u(z) \propto ln(z/z0)$ [2]. As roughness increases, the boundary layer velocity tends to decrease, especially in the first 10% of the thickness. Some typical surface roughnesses: (Linacre & Geerts, 1999)

- 0.001m (rough sea)
- 0.03m open farm land, few trees
- Tens of meters for urban areas [2]

If the surface layer stability is also taken into account, the boundary layer velocity profile is given by $u(z) = u^*(ln(z/z0) + \Psi)/\kappa$, (where $u^* = \sqrt{(\frac{\tau w}{\rho})}$, with τ_w =the wall shear stress, κ the von Kármán constant (~ 0.4) and Ψ a function depending on stability. For a neutral atmosphere one might take $\Psi = 34.5fz/u*$ with f= $2\Omega\sin|\lambda|$, depending on the Earth's rotational speed Ω and latitude λ. [2]

Turbulence intensity is defined as $I=\sigma/u$, where σ is the standard deviation of the wind velocity in the average wind direction, and u is the magnitude of the average wind velocity. Turbulence increases with height inside the ABL. Since a wind turbine extracts energy from the wind, a fluid element passing through the rotor disk loses part of its kinetic energy. The incoming flow slows from an upstream value of u_∞ to an average far downstream value of u_w. The static pressure increases from p_∞ upstream to p_d^+ just in front of the disk, then drops suddenly to p_d^- behind the disk, which is associated with the axial force exerted by the disk. The pressure gradually recovers in the wake to reach free-stream value. The continuity equation can be given by $\dot{m} = \rho A_\infty u_\infty = \rho A_d u_d = \rho A_w u_V$, the force on disk by $T = \dot{m}\,(u_\infty - u_w) = (p_d^+ - p_d^{-+})A_d$, and the energy extracted: $E = \frac{1}{2}m(u_\infty^2 - u_w^2)$. [2]

The torque on turbine blades is exerted by the passing flow. A reaction torque acts on the flow, causing it to rotate in the direction opposite that of the rotor, introducing a tangential velocity component. At the tip of the blade the difference in pressure between the lower and upper side leads to the formation of a tip vortex. This vortex first decreases in diameter, then increases due to viscous effects. Tip vortices follow a helical path with rotation opposite the rotor. [2]

The wake of a turbine is characterized by the velocity deficit, which leads to reduced power for downstream turbines, where losses can be highest for first turbine downstream of leading turbine, and enhanced turbulence, which leads to dynamic loading and fatigue on the turbine blades, leading to reduced lifetimes. High turbulence levels in large wind farms, however, can increase wake recovery and actually increase output. [9]

A wind turbine wake is divided into a far and near wake. The near wake is the region from the turbine to approximately one rotor diameter downstream. The shape of the flow field in the near wake is determined by the turbine geometry. In the near wake the axial pressure gradient is important for the development of the wake deficit. The far wake is where the shape of the rotor is less important, but interactions between wakes in wind farms, turbulence, atmospheric stability, and topographical effects are dominant. The turbulence of a wind turbines wake mixes the low velocity fluid in the wake with the high velocity fluid outside it. Momentum is thus transferred into the wake and the velocity deficit is decreased with distance from the turbine. [2]

Lower ambient turbulence levels typically lead to larger wake velocity deficits, and longer recovery lengths. The turbine power deficit is maximal at low wind speeds and low ambient turbulence levels. The decay of the velocity deficit is more rapid than decay of turbulence intensity between turbines. In addition, the incremental energy loss between turbines decreases the farther the turbines are located from the first turbine. The rate of decrease of velocity tends to reach an equilibrium value. [5]

Flow characteristics over complex terrain are significantly different than those over a flat surface- including wind speed, direction, and turbulence levels. Most studies characterizing resources and quantifying performance are conducted over simplified flat surfaces. The primary change in flow over complex terrain is the speed-up effect: flow acceleration when passing over a hill, and the associated deceleration on the lee side of the hill. There are often huge differences in wind speeds in different positions over hilly terrain. Flow will decelerate at the upwind foot of the hill, before accelerating at the top of the 2D ridge. [1] Early wind tunnel studies of flow over low hills [6] revealed an asymmetric character to the speed-up and provided experimental data for comparison with results of an analytical model proposed by Jackson and Hunt [7]. The results of Arya, Capuano and Fagen [8] agree that boundary layer flow over “gentle” or moderately sloped hills is proportional to the average slope of the hill, reaching some optimum slope which would yield a maximum speed-up at the hills peak.

There is a larger reduction in output for turbine at the foot of a high slope hill than one at the base of a moderately sloped hill; slowdown is more pronounced for steeper hills. A turbine on the top of a hill will produce more power than one on flat ground because of this speed up effect. Speed-up of flow is dependent on the slope of the hill, with largest seed-ups observed for moderately sloped hills, with no significant separation on lee side. On the high slope ridge the speed up is lower because of the separation of the wake, which affects the whole flow field. With a steep enough hill, separation of the flow will occur on the lee side, characterized by strong adverse pressure gradients, causing velocity deficits and enhanced turbulence levels. The critical angle for flow separation on the lee side is 18˚-20˚. Turbines located in such a position will suffer from shorter lifetimes and reduced output. Behind long, steep ridges the wake may extend 10 hill heights downstream. [1]

3. Experimental methods

All experiments were conducted in the Aerodynamic/Atmospheric Boundary Layer (AABL) wind tunnel in the aerospace engineering department of Iowa state university. The AABL is a closed-circuit wind tunnel with a test section that is 20 m long, 2.4 m wide, and 2.3 m high. The

maximum wind speed of the wind tunnel is 45 m/s, with flow generated by an electric fan. The wind speed is controlled by the rotational frequency of the fan- in this experiment it was a constant 5.5 Hz.

Wood blocks and chains were installed as roughness elements in the first ten meters of the test section surface, upstream of the model turbines, to mimic atmospheric boundary layer (ABL) wind and obtain a logarithmic velocity profile. Spire-type vortex generators were used to change turbulence of inflow. The flow characteristics, including mean velocity and turbulence intensity, were measured using a cobra probe (a multi-directional anemometer made by Turbulent Flow Instrumentation Pty Ltd). The cobra probe has a range of 2-100m/s, and an accuracy of 0.5%. It can provide instantaneous measurements of three directional components of velocity, which were sampled at 1000 Hz for 60 s at each test point.

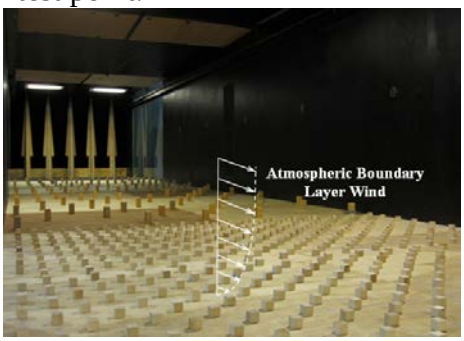

Figure 1. Wind tunnel section with roughness elements

Two hill slopes were tested— moderate and high. A two-dimensional hill model made of a wooden frame with a thin film covering was used, whose geometry is given by $z = h * \exp\left[-0.5\left(\frac{x}{\sigma}\right)^2\right], \sigma = L/1.1774$. L is the length in the x-direction between heights h/2 and h. The slope is taken to be $s = h/(2L)$. For the moderate slope hill, h/L=0.22 and s=12˚, for the high slope hill h/L=0.41 and s=22˚. No separation is observed on the lee side of the hill if the slope is less than 0.30.

Three-bladed horizontal axis wind turbine (HAWT) models were used, to represent the type most commonly installed today. The models have a rotor radius of 127 mm, and a hub height of 225 mm above the wind tunnel floor. Assuming a scale of 1:350, the models represent turbines with rotor diameter of 90 m and tower height of 80 m. The blades were based on ERS-100 prototype turbine blade developed by TPI. The blade model was generated by mathematically applying a spline in tension to interpolate between the defined input stations. NREL has developed airfoils specifically for HAWTs, with seven families of airfoils, using the Eppler Airfoil Design and Analysis Code. [4] These were designed to exhibit a maximum lift coefficient in stall-regulated, variable-pitch, and variable-rpm wind turbines. [4] Three NREL airfoils, one for root, primary, and tip sections, were used as inputs to generate blade profile. A constant circular section was used from blade root to 5% of the radius. S821 root was used between 0.208R and 0.40R, S819 primary airfoil was used at 0.70R and S820 tip airfoil was used at .95R.

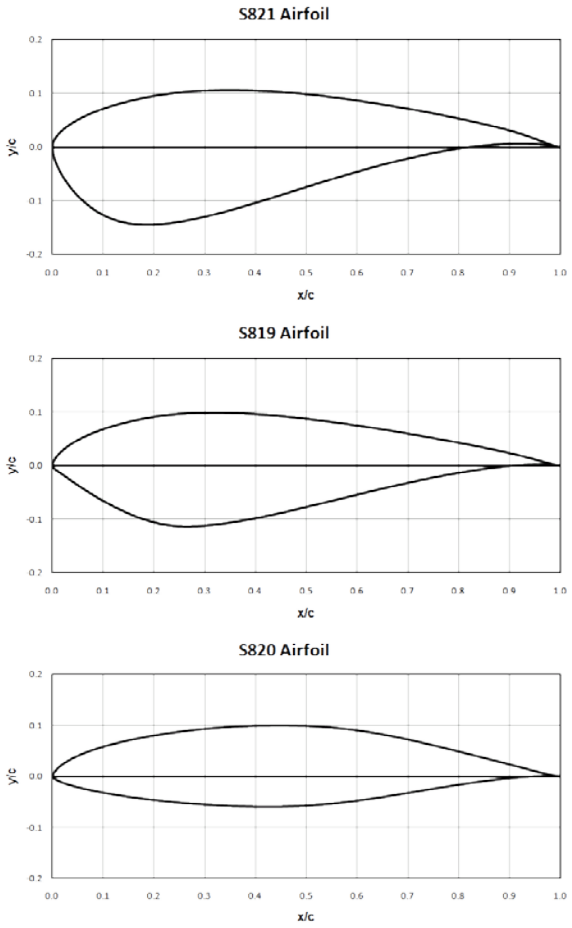

Figure 2 NREL Airfoil Sections [4]

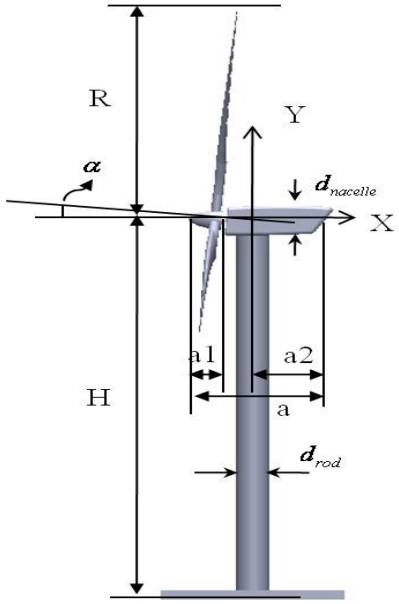

Figure 3. 1:320 scaled model to simulate a 2MW wind turbine with 90 m rotor blades

Table 1. The primary design parameters of the wind turbine model

Parameter	Dimension
R	127 mm
H	225 mm
d_{rod}	18 mm
$d_{nacelle}$	18 mm
α	5^o
a	78 mm
a1	15 mm
a2	50 mm

Aluminum rods were used as the towers, and were connected to a hole in the wind tunnel floor. The towers were connected to high-sensitivity force-moment transducers (JR3, model 30E12A-I40). The transducers have a full scale of 40 N, and an accuracy of ±0.25%. They were used to measure thrust and bending moment, which were used to find the thrust coefficient in the x direction and the moment coefficient in the z direction. Small DC motors were installed inside the nacelles of the model turbines and used as generators, to create power when the blades rotate. The voltage data was recorded at a scanning rate of 1000 Hz for 180 s.

Five positions were chosen to investigate the flow characteristics and turbine performance over the hill, all with distance of 3D (D=rotor diameter) between them. Surface flow characteristics and the performance of a single turbine at each position were measured. Next, wake characteristics and performance of all five wind turbines aligned in the free stream direction were measured to compare between hilly and flat terrain.

4. Results

Moderate slope, spires:

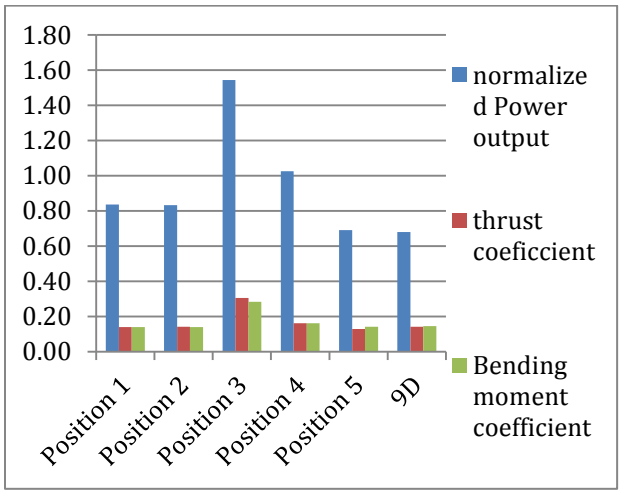

Figure 4. Output normalized with a lone turbine on flat ground with spires, thrust coefficient and bending coefficient of lone turbines on a moderately sloped hill with spires

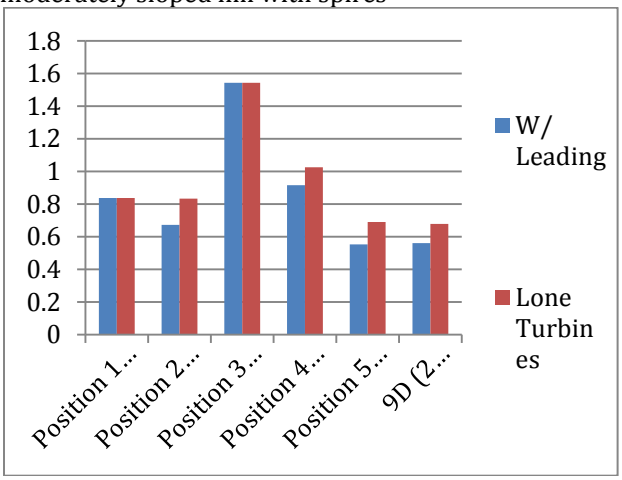

Figure 5. Output of lone turbines vs. output of those with leading turbines, normalized with power output of single wind turbine sited on flat surface

On the moderately sloped hill with spires (which create turbulent flow), the turbines in position 1 and 2, when tested without any leading turbines, have similar outputs, both around 80% of a lone turbine on flat terrain. The turbine located on the top of the hill has a significantly higher output than a lone turbine on flat terrain, about 1.5 times. When not influenced by any leading turbines, the first turbine on the lee side of the hill (position4) had a slightly higher output than a lone turbine on flat ground. The last two turbines, position 5 and one 9D downstream, have outputs lower than a lone turbine, and lower than leading two. The thrust and bending coefficients follow the same trends.

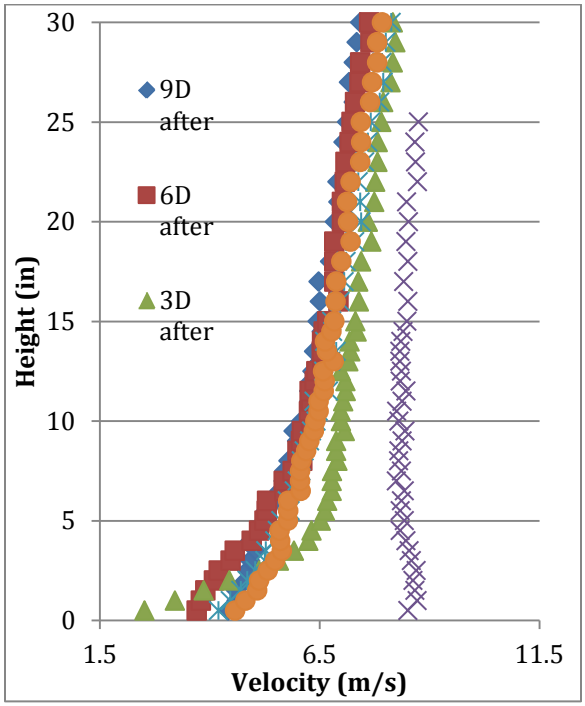

Figure 6. Velocity profiles of each position alone on the moderately sloped hill, with spires

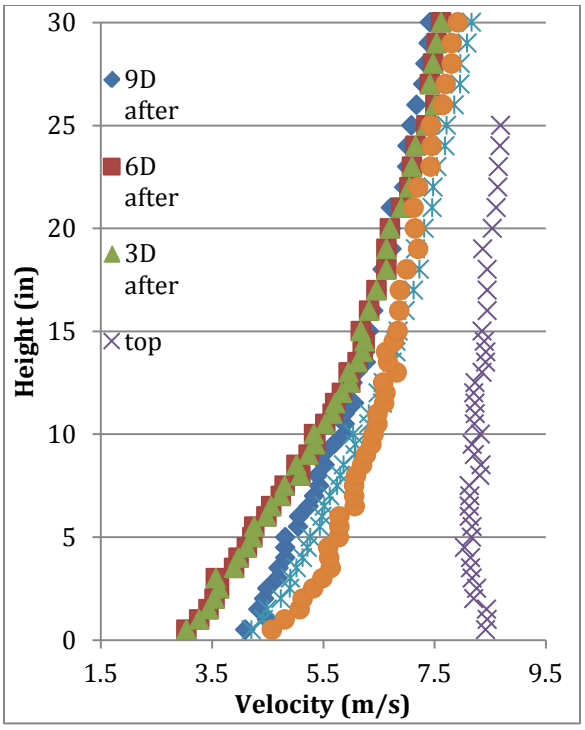

Figure 7. Velocity profiles of each position in the wake of leading turbines on the moderately sloped hill, with spires

It can be seen that the velocity profiles agree with the result of the turbine outputs. In the case without the wakes of leading turbines, the velocity profiles are very similar for the various locations besides the top, with a greater magnitude 3 blade diameters after the hill. When the wakes of leading turbines are measured, the velocity profile on the top of the hill remains much the same, and there is a bit more of a distribution between the velocities at hub height.

Moderate slope, no spires:

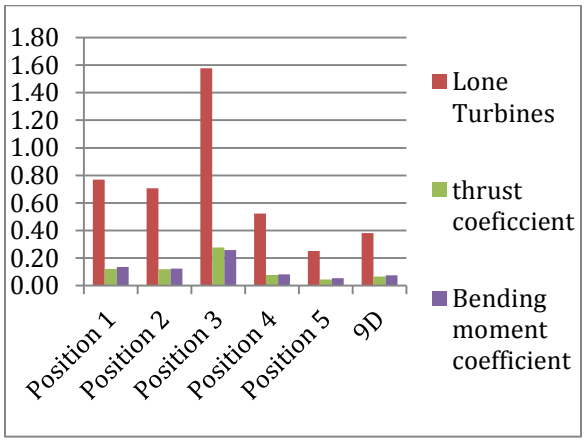

Figure 8. Output, thrust coefficient and bending coefficient of lone turbines on a moderately sloped hill without spires, normalized with a lone turbine on flat ground.

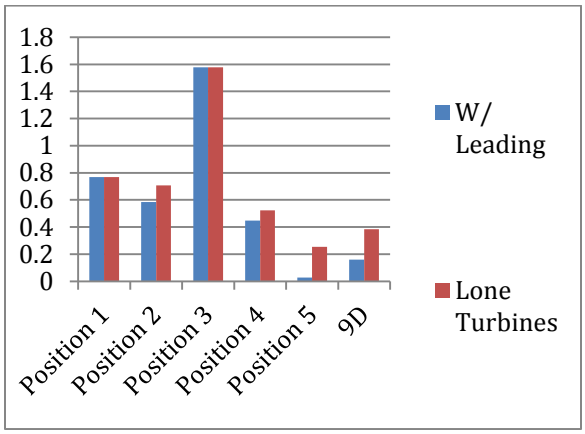

Figure 9. Output of lone turbines vs. output of those with leading turbines, normalized with power output of single wind turbine sited on flat surface

When tested on a hill with a moderate slope, but without the turbulence-inducing spires, the leading turbines had outputs significantly lower than a turbine on flat ground, 77% and 71% respectively. The output of second turbine is lower than the first, both with and without the influence of a leading turbine, though difference is more

pronounced with a leading turbine. The output of position 3, on top of the hill, is a similar increase to the spires case with 1.58 times the output of a turbine on flat ground. The outputs of last three positions are much lower than both the lone turbine and than the first two leading turbines. The turbine in position 5 has lowest output of all in this setup, with a bit of recovery in the last position, 9 blade diameter lengths after the hill.

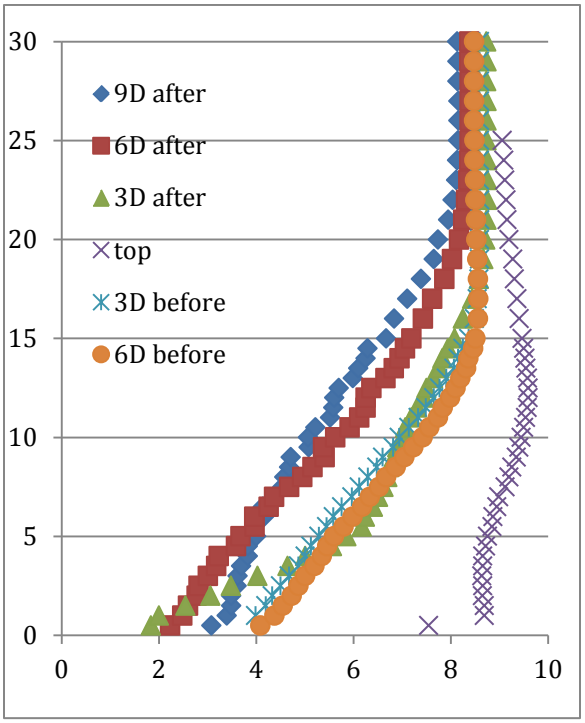

Figure 10. Velocity profiles of each position on the moderately sloped hill, without spires

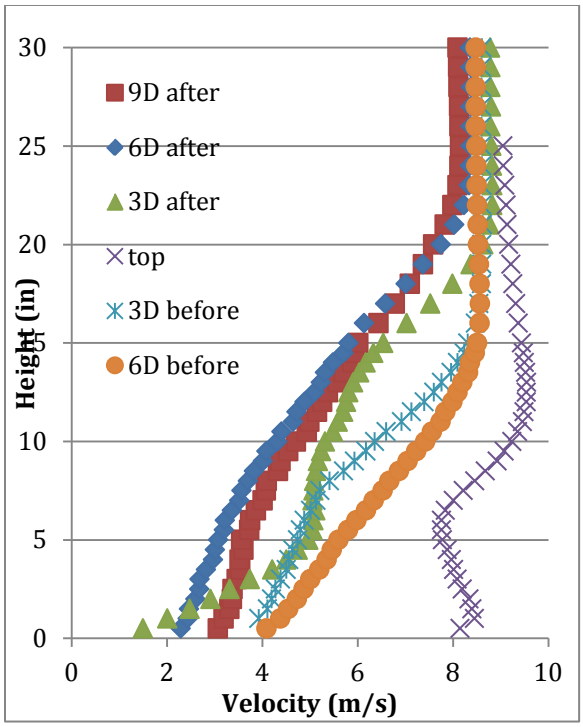

Figure11 . Velocity profiles of each position in the wake of leading turbines on the moderately sloped hill, without spires

In the case without the wakes of leading turbines, the velocity profiles are very similar for the various locations 6D before, 3D before, and 3D after. When the wakes of leading turbines are measured, the velocity profile on the top of the hill changes significantly, exhibiting a large wind shear at hub height. It can be seen that the lowest velocity at hub height is found 6D after the hill.

High slope, spire:

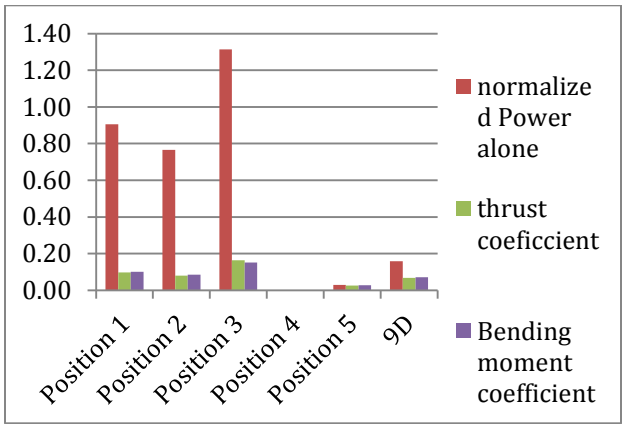

Figure 12. Output, thrust coefficient and bending coefficient of lone turbines on a high- slope hill with spires, normalized with a lone turbine on flat ground.

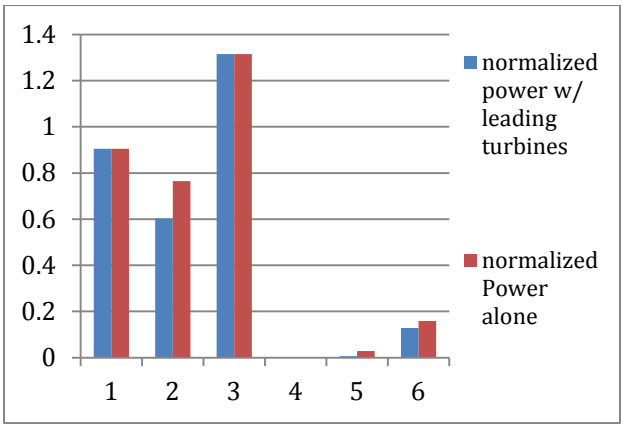

Figure 13. Output of lone turbines vs. output of those with leading turbines, normalized with power output of single wind turbine sited on flat

In the setup with spires and a high sloped hill, the leading turbine (position 1) has 90% of the lone turbine output. This decreases in position 2 to 75% of the full output. The turbine in position 3, as with all cases, has the highest output, about 130% of a lone turbine on a flat surface. There was no output in position 4, 3D after the hill, due to the separation of the flow after the high slope hill. The turbine in position 5 had very low output, about 3% of the lone turbine on flat ground. The wind recovers a little and output reached 16% at 9D.

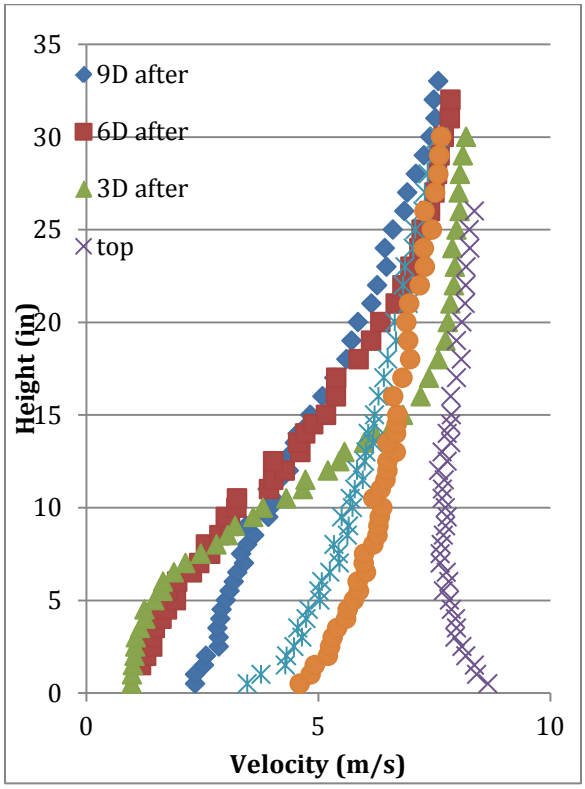

Figure 14. Velocity profiles of each position on the high sloped hill, with spires

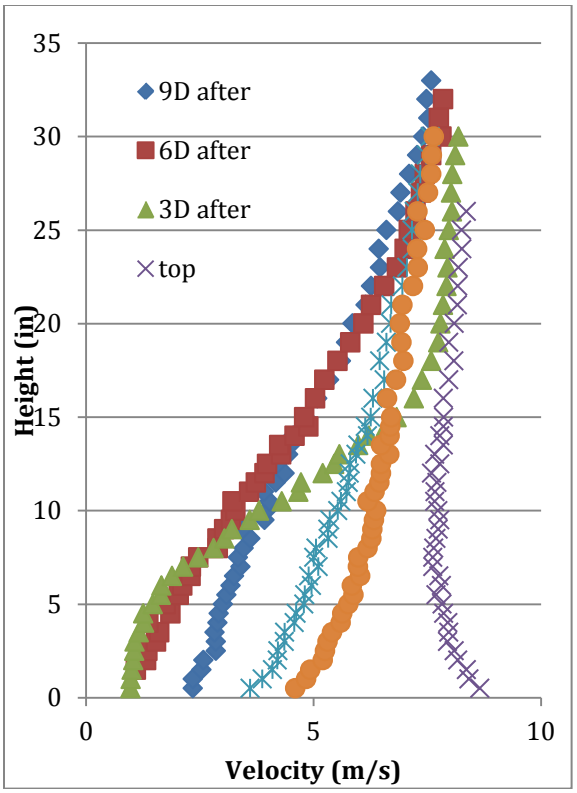

Figure 15. Velocity profiles of each position in the wake of leading turbines on the high sloped hill, with spires

On the High slope hill in flow with spires, the velocity profiles again follow the output trends. There is very little difference between the flow with leading turbines and that without. It can also be seen that the lowest velocities at hub height (9 inches) are 3D and 6D after the hill, where there is either very little or no output- the wind wasn't fast enough due to the separation to turn the model turbine.

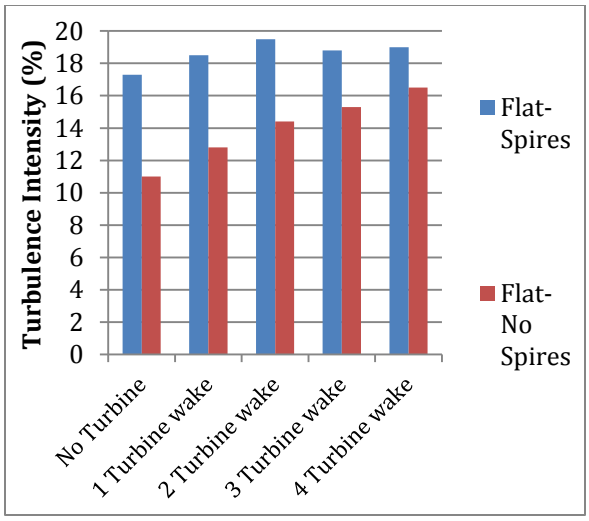

Figure 16. Turbulence levels at hub height on flat ground.

A reference for the change in turbulence levels in turbine wakes. In the spires case the turbulence in the wake stays relatively constant, and even decreases after the third turbine is added.

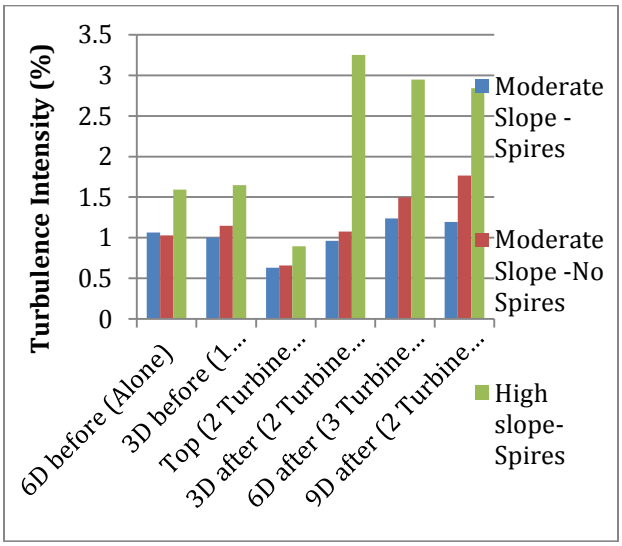

Figure 17. Hub height turbulence levels normalized with turbulence of similar incoming flow characteristics (spires or no spires) for turbines in the wakes of leading turbines in various positions on the hill.

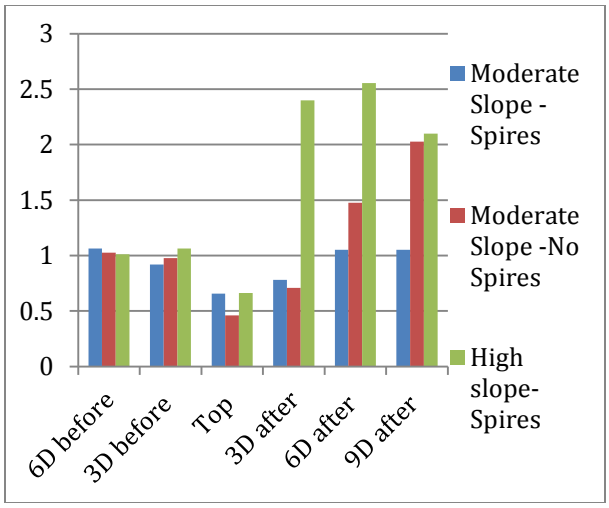

Figure 18. Hub height turbulence levels normalized with turbulence of similar incoming flow characteristics (spires or no spires) for lone turbines in various positions on the hill.

5. Analysis and interpretation

Comparing all three:

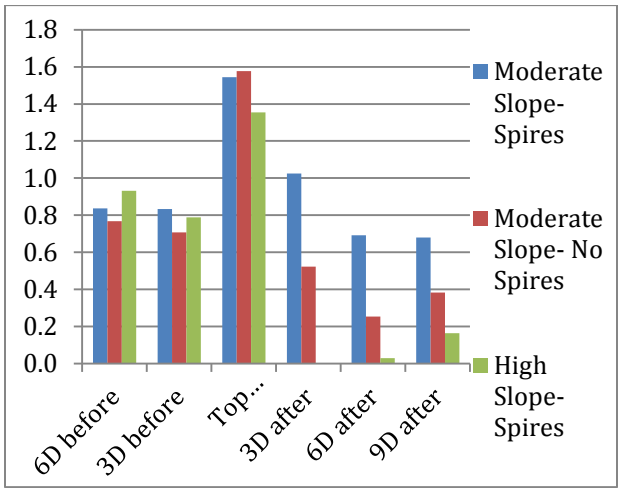

Figure 19. Normalized power of lone turbines on complex terrain

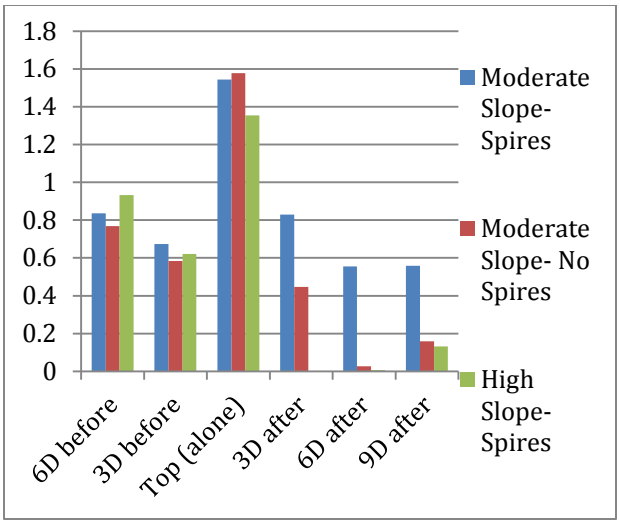

Figure 20. Normalized power of turbines with leading turbines on complex terrain

On the moderately sloped hill with spires, the output of turbines not influenced by the wakes of leading turbines are similar in the first two positions, a little more than 80% of the output on flat ground. This slowdown is more pronounced on the high slope hill, due to the slope of the hill and in the moderately sloped hill without spires, due to the lack of mixing generated from the higher turbulence.

It is clear that the next position, the top of the hill, is the most advantageous location for turbine siting. This turbine has an output of about 1.5 times one on flat ground for each hill and incoming flow condition, and experiences only 65% of turbulence levels for a turbine on flat ground.

The output of the lone turbine 3D after the hill was slightly higher than one on flat ground. This could be due to the carrying over of the same velocity increases experienced at the top and the lack of separation. Even in the wake of leading turbines, this position has greater output than the second position, and only half a percent lower than the output of the first position, 6 diameter lengths in front of the hill. In the lower turbulence case the output is much decreased- lower than both

positions before the hill. When considering locations for a turbine on a hill this position should not be used unless the incoming flow has a high level of turbulence.

Turbines on the moderately sloped hill without spires have highest output for first three positions, but after the peak of the hill those on the moderately sloped hill without spires have slightly higher output. The high slope output is virtually nonexistent after the hill-probably due to separation of flow on lee side of high slope. The output of position 1 is slightly higher in the high slope scenario than the moderate slope with spires. The turbine on the top of the hill, the position with the highest output, has the most advantage with the moderately sloped hill without spires, though this comparison does not include the influence of leading turbines.

The inclusion of spires generates greater turbulence in the flow than the roughness elements alone. This type of turbulent flow is observed in onshore wind farms (as opposed to offshore) ambient turbulence is higher, and where unstable atmospheric conditions exist.[1] This indicates that the observations with flow influenced by spires are the most relevant to be considered.

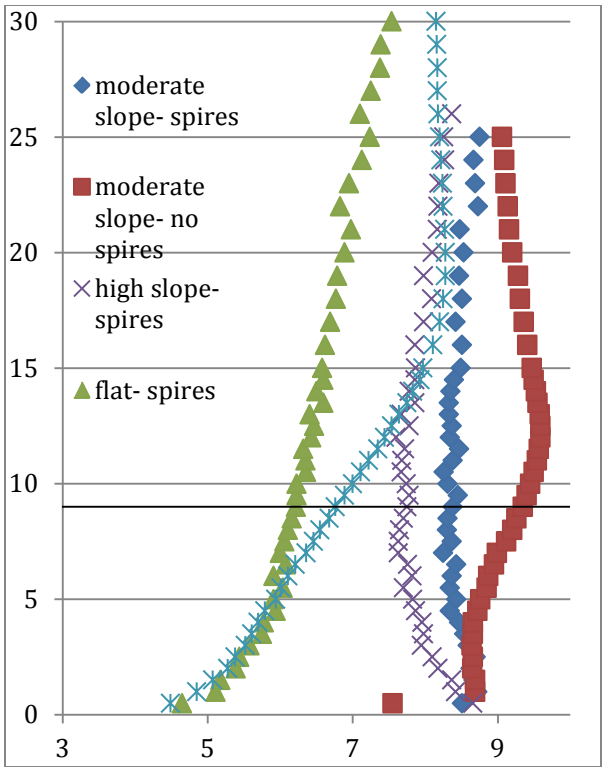

Figure 21. Velocity profiles at the top of the three configurations with the flat ground for comparison.

As can be seen, at hub height the moderately sloped hill without spires has the largest velocity, though the relative increase compared to a turbine on flat ground is lower than that of the moderately sloped hill with spires. The no spire case also has greater wind shear, which is less advantageous. The highly sloped hill has the lowest velocity at hub height over the peak, but it was still higher than either case on flat ground.

6. Conclusions

Wind turbine performance is affected significantly by character of incoming flow and by the terrain of the wind farm. The increased turbulence added by the inclusion of spires in the oncoming flow contributed to making vertical mixing an important mechanism in the flow,

allowing for greater wake recovery than the case without spires.

Wind turbines sited on top of the 2D-Ridge in all cases experience higher wind speeds and thus power output, and are exposed to reduced turbulence levels compared to those sited on flat terrain. Turbines sited after a hill however, will experience lower wind speeds and power outputs, and are exposed to higher turbulence levels. The turbine on the top of the moderately sloped hill in the high ambient turbulence case showed the greatest relative increase in output, as well as experiencing low turbulence and minimal wind shear.

Acknowledgements

Support for this research was provided by a National Science Foundation Research Experience for Undergraduates site program in Wind Energy Science Engineering and Policy (WESEP) at Iowa State University.

References

Ozbay, A., 2012, "Experimental investigations on the wake interferences of multiple wind turbines," master's thesis, Iowa State university, Ames IA.

Sanderse, B., 2009, "Aerodynamics of wind turbine wakes: Literature review," ECN-e--09-016, Energy Research Center of the Netherlands.

US Energy Efficiency and Renewable Energy, 2008, "20% Wind Energy by 2030: Increasing Wind Energy's Contribution to U.S. Electricity Supply," DOE/GO-102008-2567, U.S. Department of Energy

National Wind Technology Center, 2012, "Wind Turbine Airfoils" National Renewable Energy Laboratory, U.S. Department of Energy, Office of Energy Efficiency & Renewable Energy.

Barthelmie, R.J., S.C. Pryor, S.T. Frandsen, K.S. Hansen, J.G. Schepers, K.Rados, W.Schlez, A. Neubert, L.E. Jensen and S. Neckelmann, February 5, 2010. "Quantifying the Impact of Wind Turbine Wakes on Power Output at Offshore Wind Farms" Journal of Atmoshpheric Science and Oceanic Technology, Volume 27.

[Britter, R. E., Hunt, J. C. R., Richards, K. J., July 7 1980. "Air Flow Over a Two-Dimensional Hill: Studies of Velocity Speed-Up, Roughness Effects and Turbulence" Quarterly Journal of the Royal Meteorological Society, 107, pp 91-110.

Jackson, P. S., Hunt, J. C. R., March 19 1975. “Turbulent Wind Flow Over a Low Hill” Quarterly Journal of the Royal Meteorological Society, 101, pp 929-955.

Arya, S., Capuano, M., & Fagen, L. August 22 1986. “Some Fluid Modeling Studies of Flow and Dispersion over Two-Dimensional Low Hills”. Atmospheric Environment Vol.21, Issue. 4, pp 753-764.

Jensen, L. (2007). Array efficiency at Horns Rev and the Effect of Atmospheric Stability. Dong Energy Presentation.

Frequency Dynamic Impact by a Transmission Overlay in a Renewable Sourced Power System

ELENA C. HOFF
Wind Energy Science Engineering and Policy REU, Iowa State University, Ames, Iowa
Mentors: Dionysios Aliprantis and Hugo Villegas-Pico

Abstract

In this paper I seek to lay out the process by which one can analyze how the power system frequency dynamics may be improved by an EHV AC and HVDC national transmission overlay, when electric power is primarily sourced by renewables. Motivation stems from the necessity of a high-capacity network capable of transmitting energy across the United States due to an increased supply of renewable sources planned for the fast-approaching future. This process can be used as a tool to identify if a proposed transmission overlay will adequately reach standards of dynamic frequency stability. If these standards are not reached, the proposed transmission system should be refined for future assessments.

1. Introduction

The motivation behind a transmission overlay is to transport the energy generated by renewables to large load centers where cities and industries are located. Since, high penetration of renewables bring about problems related with the dynamic behavior (speed/frequency) in a power system, an assessment of the new transmission overlay technology is necessary to investigate if a specific design may minimize these concerns [1]. In order to do this, from a given proposed system [2], we estimate AC lines parameters of a new overlay to perform a dynamic simulation. DC lines are also to be analyzed to investigate how they may be used to improve the frequency dynamic behavior.

In order to lay out a comprehensive procedure for the analysis of frequency dynamics of a multi-line High Voltage AC and DC national transmission system, it is necessary to break down the process into various steps. First, the AC overlay parameters have to be estimated, given the length and capacity of each proposed transmission line. We determine these parameters from previous research projects – and accepted tables – to design a single transmission overlay system and to calculate the impedance of each tie-line along with phase differences through calculations done with Matlab. We, then, learn how we may optimize these numbers by manipulating each line's geometry and attempt to maximize the capacity of each line while limiting ourselves to consider economic and environmental costs. Finally, using this generated data, we are able to create differential equations that model the frequency dynamics of this system. Once the procedure is established, further refinements of parameters – as well as a more extensive cost/benefit analysis – can easily replace the approximated values in this study in order to complete the equations and provide useful direction for further planning of a transmission overlay.

2. Literature Review

The nation's transmission grid system is currently divided into three main self-sufficient regions: the Eastern Interconnection, Texas, and the West [3] depicted below in Figure 1.

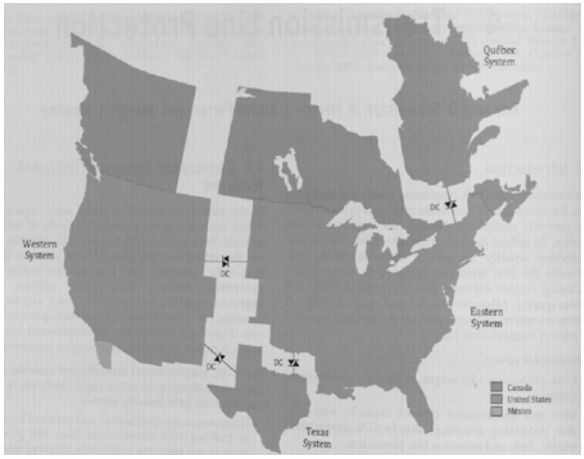

Figure 1: Three regions connected by DC links[4]

Figure 2 displays that the few existing transmission lines between these regions have very low capacity for there is little need for transferring energy between regions.

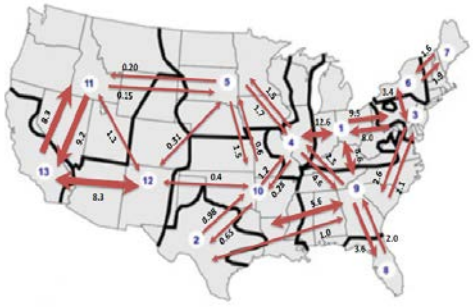

Figure 2: Estimated corridor capacity [3]

However, this need is constantly growing due to further development of renewable energy sources specific to regions of the United States, such as wind to the Midwest and solar to the Southwest. In order to reach the progressive standard set by the 2008 Department of Energy report maintaining that 20% of the U.S. Energy portfolio can come from Wind Energy by 2030 [4], a complete expansion of the transmission system will be required.

The theorized system is one that would equally connect and transmit power among all areas within the United States in a national transmission grid. Therefore, a new transmission overlay – a high-capacity network spanning the nation and integrated into the existing structure is required. Forming such a robust system could anticipate future energy needs of our country [6] by facilitating long-term flexibility [3] for accessing diverse generation resources, such as renewables [7], and solving energy demand at the national level.

Multiple aspects of a transmission overlay in a renewable sourced power system need to be considered in order for the planning process can begin. One such criterion is the frequency dynamic interplay between the sources and the loads – an indication of balance. There is slight concern about renewable sources because of their asynchronous nature when connected to the grid as opposed to conventional generation.

In an interconnected power system, one can simplify the model by assuming that frequency (rotor speed) is the same inside each control area consisting of generators and loads due to the synchronous nature of the localized system, which can be visualized as one large rotating mass. Through this assumption, frequency analysis can be isolated to the tie-lines, the transmission lines between control areas. The real power balance of a system is what dictates the frequency dynamics – which ideally should remain constant [8]. However, areas with large amounts of renewable sources may experience abnormal power unbalance, influencing frequency fluctuations. Thus, we need to investigate how a transmission overlay may help to improve, through damping, those fluctuations in frequency.

3. Experimental Methods

Maps

In order to simplify our analysis, we divide the major regions across the United States into 13 separate areas and approximately mapped out the existing interconnections, which can be seen in Figure 3.

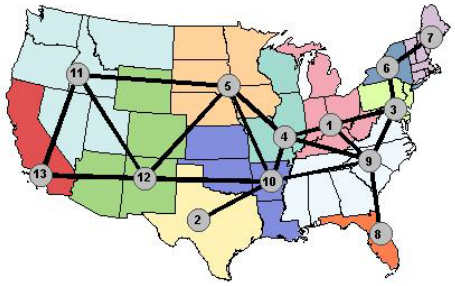

Figure 3: Existing HVAC and HVDC interregional Transmission System

Presented with an approximate transmission overlay design adapted from proposed future power transfer corridors [2] of over 250 additional transmission lines throughout the next 40 years, we sifted out the interregional connections – according to our defined areas – to use for our analysis. In order to visualize our data, we added another layer (Figure 4) to our transmission map in order to view the entire extent of the proposed system.

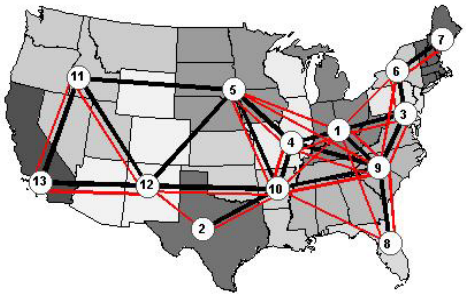

Figure 4: Existing HVAC and HVDC Transmission System with the proposed overlay [2]

Calculating Impedance for a new EHV AC – 765 kV Overlay

To analyze the frequency dynamics within the new transmission overlay, we need to estimate the new transmission parameters. In preparation to model each interconnection as a single tie-line, we investigate how power is transferred between two areas. It is necessary to first calculate the effective impedance, Z', of the tie-lines between the areas. The resistance, *R*, of the transmission line is assumed to be negligible, we arrive at impedance, *Z*, to be relatively equal to the imaginary part of the reactance, *X* – as shown in Figure 5.

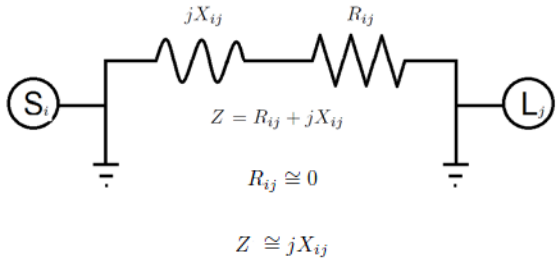

Figure 5: Approximated tie-line

Following specifications employed by AEP operating at 765 kV, we initially apply a line geometry consisting of a 6-conductor bundle with a bundle diameter of 30" and 45' phase spacing [9]. We then looked up the appropriate inductive reactance at 1ft spacing X_a from Table 3.3.1 [10] and inductive reactance spacing factor X_d from Table 3.3.12[9] for the designated line geometry and added them together to compute the inductive reactance X_L in ohms/mile.

Through Matlab, we multiplied the inductive reactance by the theoretical length of the tie-line (in miles), converted to per unit (using a base power of 100MVA), and supplied the correction factor that allows us to use our consolidated assumptions for lines longer than 100 miles [11]. This provided us with a useful *Z'* value, derived in Figure 6, for our supplementary calculations.

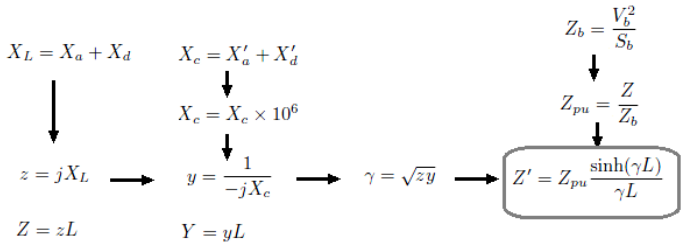

Figure 6: Equation map for calculating Z'

A table was created containing the interregional connections we sifted out from the original data, grouped from one specific region to another. The table also contained the length of each line (miles), required transmission capacity (GW), number of proposed transmission lines at that capacity, and the proposed year. We expanded the table to divide the lengths of each transmission line into segments of 300 miles or fewer in order to transmit at 100% loadability [12]. Intermediate substations are required to condition the voltage levels throughout the lines, as seen in Figure 7.

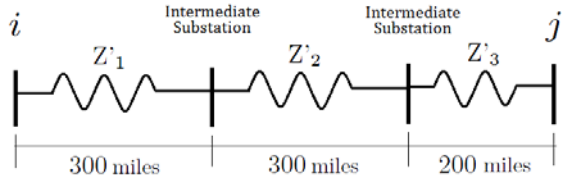

$$Z'_{eq} = Z'_1 + Z'_2 + Z'_3$$

Figure 7: Visual representation of segment division

Table 1: Z'eq calculation for one line segment

		6-Conductor TERN, 30" Bundle Dia, 45' Phase Spacing								
					Capacity					
From	To			Length	Plij (GW)	# Lines		Year	Z' (segment)	Z'eq
6	7	N1	NT	385	6	1		3		0.0297
				300					0. 022859	
				85					0. 006830	

This process outlined above was automated through a loop in Matlab that read in each segmented length from the excel spreadsheet, calculated the *Z'* and then wrote the output value in the specified column in the same spreadsheet through the "xlswrite" function. Table 1 indicates how the *Z'eq*, or equivalent impedance of the line, was calculated as the sum of impedances of each segment.

Calculating P_{SIL}

Once the equivalent impedance of each line is determined, a couple more factors need to be calculated before dynamic analysis can be made. The Surge Impedance Loading, P_{SIL}, is the power loading at which the reactive power is not produced or absorbed in the transmission line. The P_{SIL} of each line geometry is necessary to determine the number of required circuits needed for each line. It can be calculated by using the per-unit length impedance and admittance along with the Line-to-Line voltage, V_{LL}, of 765 kV and a power base, S_b, of 100 MVA.

$$Z_c = \sqrt{\frac{z}{y}}$$

$$P_{SIL} = \frac{V_{LL}{}^2}{Z_C}$$

$$P_{SILpu} = \frac{P_{SIL}}{S_b}$$

This is the maximum power capacity of each circuit per-unit (a method of stating values relative to a base value), as determined by the line geometry. With this information, we can calculate – through simple Excel formulas in Table 2 – the number of circuits necessary to reach the desired power capacity P_{Lij} delivered to the load.

Table 2: Required Circuit calculation for one line segment given P_{SIL}

					Capacity						
From	To			Length	Plij (GW)	# Lines	Year	Z' (segment)	Z'eq	Psil p.u.	# Required Circuits
6	7	N1	NT	385	6	1	3		0.0297	24.15	3
				300				0. 022859			
				85				0. 006830			

$$\Delta\theta = \theta_i - \theta_j = \arcsin\left(\frac{P_{Lijeq}}{b_{ijeq}}\right)$$

Calculating b_{ij} and $\Delta\Theta$

For dynamic analysis, we are looking for the susceptance, b_{ij} – a function of the impedance of each tie-line. To calculate this value, we once again approximate and assume that the voltage drop across the tie-line is negligible. As a result of working in per-unit, V_i and V_j are both approximated to be 1 p.u. This b_{ij} factor can be calculated by taking the reciprocal of the Z'_{eq} and then multiplying by the number of circuits required to transmit the the desired total power from area I to area j, since they are being added in parallel, visualized in Figure 8.

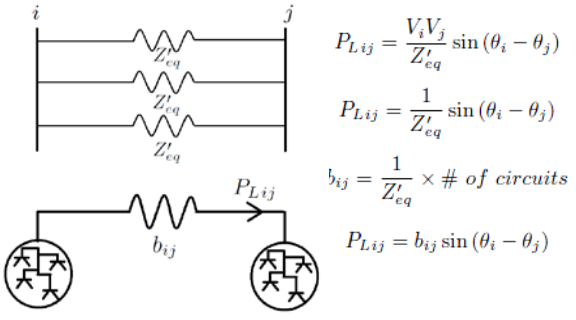

Figure 8: Visual representation adding Z'eq in parallel

The final step is to calculate the $\Delta\Theta$, the phase shift within each circuit. This quantity is used to double check that an adequate transmission line was designed.

A $\Delta\Theta$ must be calculated for each tie-line during the first period and the second period of time to double cheack that it remains within the stead state stability limits. Table 3 presents this process by adding up the equivalent power loaded and the equivalent b_{ij} for each time period and using the formula stated above.

Determining Line Geometries

The characterizations of line geometry consist of the number of conductors used in each bundle, the bundle diameter and the phase spacing in each circuit, which involves three phases. As depicted in Figure 9, conductors are bundled together in each phase in order to avoid the corona effect, audible noise for Extra High Voltage (between 300kV and 1000kV), and improve the loadability of overhead AC transmission lines [13].

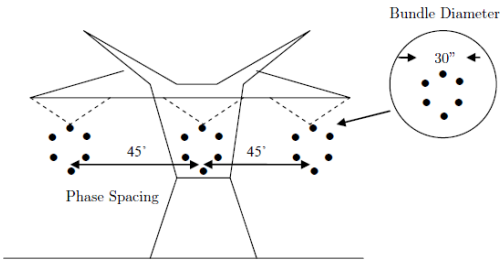

Figure 9: Line Geometry Diagram [9]

Table 3: b_{ij} and $\Delta\Theta$ calculation for a tie-line for each period of analysis

		6-Conductor TERN, 30" Bundle Dia, 45' Phase Spacing										20 years			
					Capacity						# Required	40 years			
From	To			Length	Plij (GW)	# Lines	Year	Z' (segment)	Z'eq	Psil p.u.	Circuits	bij (per length)	bij eq	Plij eq	dTheta
6	7	N1	NT	385	6	1	3		0.0297	24.15	3	101.047			
				300				0. 022859							
				85				0. 006830							
		NS	N1	368	6	1	19		0.0283	24.15	3	105.887			
				300				0. 022859							
				68				0. 005473							
		N2	NE	312	6	1	20		0.0238	24.15	3	125.903	333	18	32.7
				300				0. 022859							
				12				0. 000969							
		N1	NT	385	6	1	23		0.0297	24.15	3	101.047			
				300				0. 022859							
				85				0. 006830							
		NT	N3	111	4.1919142	1	34	0.008890	0.0089	24.15	2	224.965			
		NS	N4	98	4.5555236	1	38	0.007863	0.0079	24.15	2	254.368			
		NT	N3	111	4.1919142	1	40	0.008890	0.0089	24.15	2	224.965	1138	37	18.9

There is no need to choose one specific line geometry to use throughout the entire transmission overlay. The requirements of each segment should be carefully studied to choose the geometry best suited for that individual segment. The idea is to minimize the economic and environmental cost of the transmission line while maximizing the power that can be carried. Economic costs include (but are not limited to): the number of circuits required to transmit the desired capacity and, therefore, the number of towers to hold the lines (approximately one tower for two circuits), as well as the volume of the conductors used per mile – Table 4 and Figure 10. The number of circuits and towers used for transmission is also an environmental cost due to a 200m Right of-Way that comes with each 765kV tower [14] .

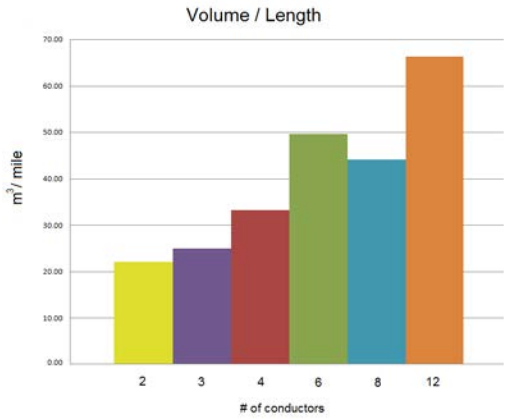

Figure 10: Conductor volume graph for economic analysis

Table 4: Volume calculations for given number of conductors

		Line Geometry			
# of Conductors	Conductor Diameter (cm)	Bundle Diameter (inches)	Phases	Circuits	Volume (m^3/mi
2	2.70	12	3	4	22.11
2	2.70	18	3	4	22.11
2	2.70	24	3	4	22.11
3	2.70	12	3	3	24.88
3	2.70	18	3	3	24.88
3	2.70	24	3	3	24.88
4	2.70	12	3	3	33.17
4	2.70	18	3	3	33.17
4	2.70	24	3	3	33.17
6	2.70	24	3	3	49.76
6	2.70	30	3	3	49.76
6	2.70	36	3	3	49.76
6	2.70	54	3	3	49.76
8	2.70	27	3	2	44.23
8	2.70	40	3	2	44.23
8	2.70	60	3	2	44.23
12	2.70	33	3	2	66.34
12	2.70	50	3	2	66.34
12	2.70	75	3	2	66.34

Note: number of circuits is limited to reasonable values due to the corresponding P_{SIL}

The benefit of each geometry can be portrayed through the P_{SIL}. A higher P_{SIL} is achieved by increasing the number of conductors used in a bundle, increasing the bundle diameter or decreasing the phase spacing. Figure 11 helped us with this process. The limitations of this, however, are followed by the minimum phase spacing to avoid flash over. For the purposes of our calculations, we are generally focusing on 45 ft phase spacing presented again by the AEP specifications. In practice, a higher P_{SIL} generally results in a lower $\Delta\Theta$, phase change, indicating a better line geometry. The ideal $\Delta\Theta$ is in the range of 10° – 30° at designed power transfer capacity.

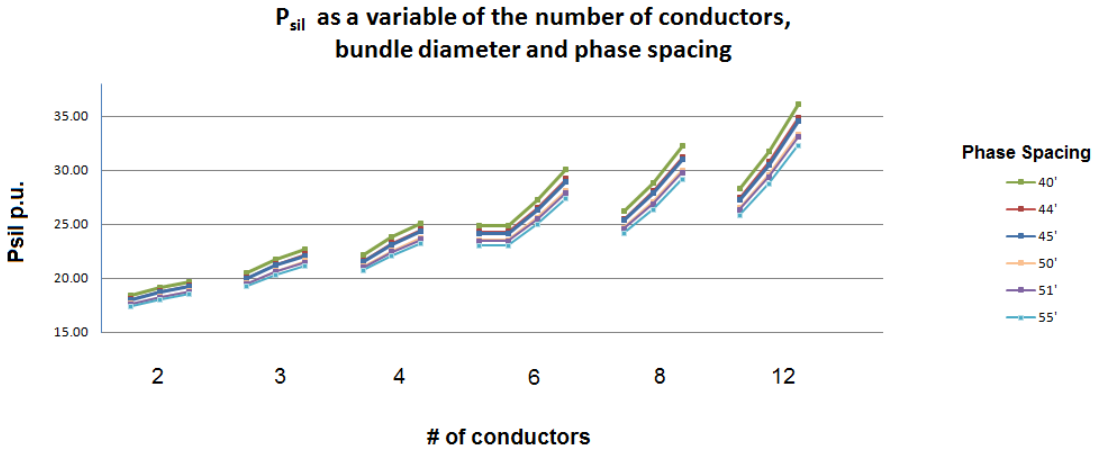

Figure 11: Graphical P_{SIL} analysis

The volume of material required to build the transmission lines for each geometry is weighed against the $\Delta\Theta$ obtained in each segment along with the number of circuits required to choose the best line geometry for that segment. By carefully scrutinizing this decision, we were able to determine our best b_{ij} associated with each proposed transmission tie-line at least cost, as seen in Table 5. Analysis allows consideration of how the proposed overlay will interact with the existing system as if installed in 20-year increments.

Table 5: Final b_{ij} and $\Delta\Theta$ calculations for each tie-line in the proposed transmission overlay

			Final Line Configurations				20 years			
							40 years			
From	To	Conductors	Bundle Diameter (in)	Phase Spacing (ft)	# of circuits	Notes on uniformity	bij	Plij eq		dTheta
6	7	8	60	51	2 or 3	3 circuits instead of rounding up to 6GW	396	25		39.1
		8	60	51	2 or 3	3 circuits instead of rounding up to 6GW	1350	44		19.0
10	8	4	24	45	4	Uniform - Overkill with 4	65	6		67.4
		4	24	45	4	Uniform - Overkill with 4	129	12		68.5
10	5	6	54	45	3	Uniform	397	24		37.2
		6	54	45	3	Uniform	770	42		33.1
12	2	---	---	---	---	---	---	---	---	---
		---	---	---	---	---	---	---	---	---
2	10	8	60	51	2 or 3	3 circuits instead of rounding up to 6GW	627	27		25.5
		8	60	51	3	3 circuits instead of rounding up to 6GW	745	33		26.3
1	9	8	60	51	3	Uniform - 3 circuits instead of rounding up to 6GW	662	42		39.4
		8	60	51	3	Uniform - 3 circuits instead of rounding up to 6GW	1640	108		41.2
1	6	2	12	45	4	Uniform	285	12		24.9
4	1	4	24	45	2 or 3	a few have 3 circuits	7490	183		14.1
		4	24	45	2 or 3	a few have 3 circuits	9062	222		14.2
13	11	8	60	51	3	Uniform - 3 circuits instead of rounding up to 6GW	80	6		48.6
		8	60	51	3	One 2 circuit - 3 circuits instead of rounding up to 6GW	324	15		27.6
13	12	4	24	45	4	Uniform - Overkill with 4	146	12		55.3
		4	24	45	4	Uniform - Overkill with 4	482	30		38.5
12	11	4	24	51	4	Uniform - Overkill with 4	63	6		72.2
12	10	4	24	45	4	Uniform - Overkill with 4	128	12		69.6
8	1	---	---	---	---	---	---	---	---	---
		---	---	---	---	---	---	---	---	---
4	5	6	30	45	2 or 3	Two 2 circuits	266	15		34.3
							944	53		34.2
5	9	6	54	51	3	Uniform	258	12		27.7
		6	54	51	3	Uniform	516	24		27.7
5	1	6	54	51	3	Uniform	719	60		56.6
8	9	4	24	45	4	Uniform - Overkill with 4	74	6		54.2
10	4	4	24	45	4	Uniform - Overkill with 4	333	18		32.7
4	9	4	24	45	4	Uniform - Overkill with 4	170	12		44.9
		4	24	45	4	Uniform - Overkill with 4	425	30		44.9
3	9	8	60	45	2	Uniform	393	10		14.7
		8	60	45	2	Uniform	499	16		18.7
3	6	8	60	45	2	Uniform	1449	40		16.0
		8	60	45	2	Uniform	1967	71		21.2
1	3	4	24	45	2	Uniform	1852	42		13.1
		4	24	45	2	Uniform	2922	63		12.5
9	6	4	24	45	4	Uniform - Overkill with 4	107	6		34.1

Note: The values highlighted in red are outside the stability limits, thus another transmission technology should be used. Another appropriate compensation, such as series capacitors, should be thought of to maintain the required stability limits.

Dynamic Simulation

In dynamic simulation, we will use the metaphor of a web of blocks (Figure 12) – each representing the individual control areas – connected by springs. Our theoretical "spring constants" will be our b_{ij} values or stiffness for each tie-line. The concept is to analyze what happens to the system when one spring is jostled. Ideally, the "springs" are stiff enough to account for a slight disruption and will hold the rest of the system intact by damping oscillations. If this is not the case, further considerations to the transmission technologies can be proposed and studied.

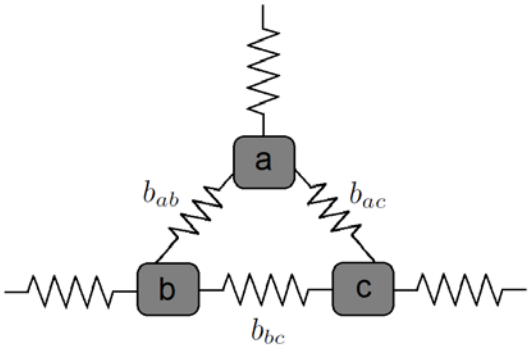

Figure 12: Block/Spring metaphor

This metaphor is possible due to the identical linear, first-order differential equations produced between the block/spring system and the tie-line dynamics seen in Figures 13 and 14. Once again, we simplify the model at first to investigate how two areas interact with each other given a slight disturbance. Each inertia constant, *H*, is specific to the individual area as well as the P_{mpu} and the P_{LOAD}.

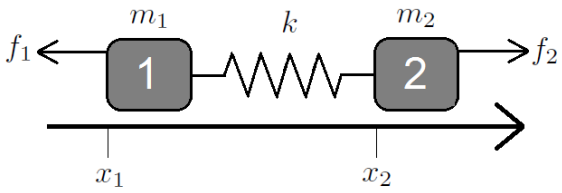

$$\begin{cases} f_2(t) - k(x_2 - x_1) = m_2\ddot{x}_2 \\ k(x_2 - x_1) - f_1(t) = m_1\ddot{x}_1 \\ \dot{x_1} = v_1 \\ \dot{x_2} = v_2 \end{cases}$$

Figure 13: Derivations of the block/spring differential equations.

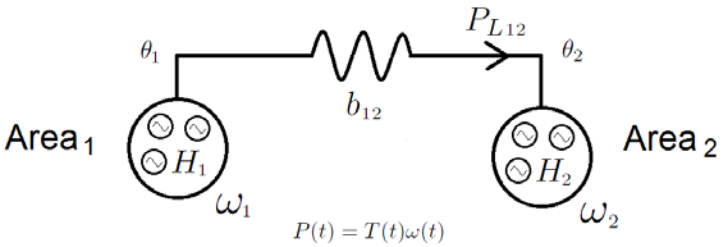

$$P(t) = T(t)\omega(t)$$

$I = moment\ of\ inertia$

$$T(t) = I\alpha = I\dot{\omega} = T_m - T_e$$

$T_m = mechanical$

$T_e = electrical$

$$\frac{\omega_b^2}{\omega_b^2}\left[\frac{2}{2}\right] I\,\dot{\omega} = T_m - T_e$$

$\omega_b = 2\pi f_b$

$f_b = 60Hz$

$$\frac{2}{\omega_b^2}\underbrace{\left[\frac{1}{2}I\omega_b^2\right]}_{W_k}\dot{\omega} = T_m - T_e$$

$$\frac{\frac{2}{\omega_b^2}[W_k]\,\dot{\omega}}{T_b} = \frac{T_m - T_e}{T_b}$$

$$T_b = \frac{S_b}{\omega_b}$$

$$2\underbrace{\left[\frac{W_k}{S_b}\right]}_{H}\frac{\dot{\omega}}{\omega_b} = \frac{T_m}{T_b} - \frac{T_e}{T_b}$$

$H = inertia\ constant$

$$2H\dot{\omega_{pu}} = T_{mpu} - T_{epu}$$

$T_{mpu} \approx P_{mpu}$

$T_{epu} \approx P_{epu}$

$$2H\dot{\omega_{pu}} = P_{mpu} - P_{epu}$$

$$\begin{cases} 2H_1\dot{\omega_{pu1}} = P_{mpu1} - P_{Load1} - P_{tie} \\ 2H_2\dot{\omega_{pu2}} = P_{mpu2} - P_{Load2} + P_{tie} \\ \dot{\theta_1} = \omega_1 \\ \dot{\theta_2} = \omega_2 \end{cases}$$

$$P_{tie} = b_{ij}\sin(\theta_i - \theta_j)$$

Figure 14: Derivations of the tie-line differential equations

After the simplistic model is complete, the next step is to model the entire transmission network in one system of equations. Analysis is to be done through Matlab and Simulink after the differential equations are combined into matrix notation.

4. Analysis and interpretation

The best way to interpret the data from the system of differential equations is through graphical analysis. We had Simulink output charts (Figure 15 and 16) to allow us to analyze the maximum displacement of the areas – the factor we are attempting to minimize.

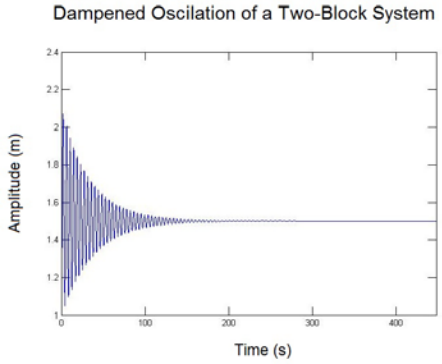

Figure 15: Example of graphical analysis of the dynamics of the two-block system

One can zoom in on the maximum point of the graph to determine the value of displacement.

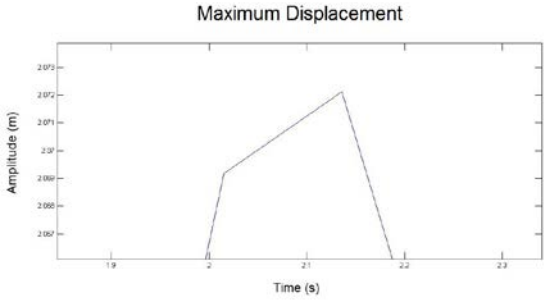

Figure 16: Example maximum displacement of the two–block system

When two springs are added in parallel, similar to the system we were conducting with tie-lines, the effective spring constant, *k*, becomes more stiff and the maximum displacement decreases. In the same sense, when we added more transmission lines in parallel between two areas the b_{ij} value increased creating a more robust connection. The displacement being discussed correlates to the synchronicity of the system. For the transmission system to function at optimum efficiency, the "displacement" must be minimized.

Considering that our calculations do not account for the existing infrastructure due to lack of precise data, there is still a lot to learn from this process. More than half of our calculated $\Delta\Theta$ values in Table 5 are much higher than desired. Indicated by a red highlight, these designs do not fulfill the expected steady state stability margins of AC design. This suggests that the implementation of a complementary technological method for high-capacity transmission is necessary. One such option is High Voltage DC. HVDC transmission is the energy efficient choice for bulk transmission over large distances (over 400 miles) [2] due to its controllability and insusceptibility to the impedance and reactive power behavior seen in AC lines. However, over shorter distances, EHV AC transmission is the preferred method considering cost efficiency [7]. Further studies are necessary on how best to integrate HVDC transmission into a primarily EHV AC transmission overlay in attempts to optimize results.

5. Conclusion

The procedure that has been laid out provides the framework for dynamic analysis of a proposed transmission overlay system necessary for the future implementation of renewable resources. Without such a system, a 20% by 2030 Wind Energy portfolio scenario is unlikely to occur. The derived system of equations allows understanding of the speed dynamics by transmission overlay – providing a mechanism to diagnose potential sources of instability and an opportunity to judge the

quality of the overlay design. By manipulating the different geometry of each transmission line in the proposed system, attempts can be made to optimize results and include EHV AC transmission where convenient. Future studies should extend the equation set to include accurate and precise existing transmission data as well as integrate HVDC into the dynamic analysis. At this point, the analysis can be done on the capabilities HVDC lines may have to improve dynamic performance.

In summary, representing the essential feature of the national transmission system by a comprehensive set of linear, first-order differential equations and performing a dynamic analysis as outlined provides a powerful diagnostic tool for the future of a safe and effective national transmission system.

Acknowledgements

Support for this research was provided by a National Science Foundation Research Experience for Undergraduates site program in Wind Energy Science Engineering and Policy (WESEP) at Iowa State University.

References

R. Doherty, A. Mullane, G. Nolan, D. J. Burke, , A. Bryson, and M. OMalley, "Trans. on power systems," *An Assessment of the Impact of Wind Generation on System Frequency Control*, vol. 25, pp. 452–460, Feb. 2010.

Y. Li, Adapted from NETSCORE meeting presentation, ISU, April, 2012

J. McCalley, J. Bushnell, V. Krishnan, and S. Cano, "Transmission Design at the National Level: Benefits, Risks and Possible Paths Forward," White Paper to PSERC, The Future Grid to Enable Sustainable Energy Systems, Funded by Department of Energy, Jan 2012

H.J. Altuve, E. O Schweitzer, III, Modern Solutions for Protection, Control and Monitoring of Electric Power Systems. Schweitzer Engineering Laboratories, Inc., 2010

U.S. Department of Energy, "20% Wind Energy by 2030: Increasing Wind Energy's Contribution to the U.S. Electricity Supply," May, 2008.

AEP. (2012, July 23rd). "A New Vision for Transmission in the U.S." [Video]. Available: http://www.aep.com/about/transmission/

J. Fleeman, R. Gutman, M. Heyeck, M. Bahrman, and B. Normark, "EHV AC and HVDC Transmission Working Together to Integrate Renewable Power," CIGRE Paper 978-2-85873-080-3, 2009.

H. Bevrani, "Robust Power System Frequency Control," Springer, New York, USA, 2009.

R. Lings, V.Chartier, P. Sarma Maruvada "Overview of Transmission Lines Above 700 kV," Inaugural IEEE PES 2005 Conference and Exposition in Africa.

"Transmission Line Reference Book: 345 kV and Above," Electric Power Research Institute, second edition, revised, publication EL-2500, 1982.

J. McCalley, Course Lecture Notes - EE 552: Power System Planning (Fall 2010). Available: http://home.eng.iastate.edu/~jdm/ee552/Transmission.pdf

R.D. Dunlop, R. Gutman, P.P. Marchenko, "Analytical Development of Loadability Characteristics for EHV and UHV Transmission Lines," *Power Apparatus and Systems, IEEE Transactions on*, vol.PAS-98, no.2, pp.606-617, March 1979

"Design Overhead Distribution Systems" Chisholm Institute of TAFE: Electrical, Electronics Engineering Department, Volume 1 of 2, May, 2010.
AEP. (2012, July 23rd), *American Electric Power: Transmission Facts,* Available: http://www.aep.com/about/transmission/docs/transmission-facts.pdf

Recycling Turbine Blade Composites: Concrete Aggregate and Reinforcement

MICHAEL HOFMEISTER
Wind Energy Science Engineering and Policy REU
Iowa State University
Ames, Iowa
Mentors: Dr. Peters, Dr. Sritharan, and Wenjun He

Abstract

To better assess the recyclability of fiberglass, a major component of wind turbine blades, different configurations and components of fiber reinforced plastic (FRP) were added to a concrete mix as reinforcement in different quantities. Additives include pure glass fabric fibers, post-pyrolysis glass fibers, fiberglass cubes substituting coarse aggregate and strips of fiberglass. Casts underwent compression testing and strain vs. stress analysis. FRP in concrete was found to retain or improve compressive strength while reducing weight. Glass fiber was effective in reducing crack propagation. Establishing an industry with recycled FRP as concrete reinforcement has potential to relieve the impending solid waste problem and help decrease the costs of wind energy.

1. Introduction

Making wind energy economically feasible will require a process that addresses the end-of-life plan for the large amount of composite blade materials being used to support the expected build-out of wind energy. The current destination for waste composites is landfills. This method, however, presents a solid waste/ environmental issue and does not take advantage of new product creation through recycling.

This research will evaluate how different fiberglass materials added to concrete affect compression strength and strain values. Additives include pure glass fabric fibers, post-pyrolysis glass fibers and strips of fiberglass. Cubes of fiberglass (~ ¼" and ½"), which substitute stone aggregate, will also be tested. FRP materials from the WEML (Wind Energy Manufacturing Lab) at Iowa State University will be cut to the appropriate configuration and added to concrete at a certain percentage by volume. Post – pyrolysis fibers will be collected from pyrolyzed fiberglass samples. FRP materials as concrete additives have been found to improve ductility and can help reduce weight. Establishing an industry with FRP use in concrete has potential to relieve the impending solid waste problem and help decrease the costs of wind energy.

2. Literature review

Currently, most FRP waste is sent to a landfill or incinerated. New regulations placing restrictions on FRP waste in landfills has driven the development of viable recycling methods for composites [1]. Relatively few studies have been conducted on composites used for concrete reinforcement. The development of fiberglass recycling has been limited by the thermoset properties of FRP materials and lack of characterization data [2].

Concrete has low tensile strength, low ductility and low energy absorption. Its low tensile strength is due to its naturally occurring internal defects. Reducing the amount of defects and crack propagation would improve concrete performance. This can be achieved by adding a small fraction (0.5% - 2%) of short fibers to the concrete mix that can bridge cracks and reduce crack propagation [3]. Fibers for concrete reinforcement should be durable in a cement

medium, easy to disperse and have an appropriate geometric configuration to be effective [3].

In one study, glass fiber reinforced polymer (GRP) waste powder and fiber were added to concrete and tested for compression strength, density, and bending strength. Results showed that glass fiber added to architectural cladding panels increased bending strength and decreased crack propagation.

Materials in concrete that bond poorly to cement due to a smooth surface and poor water absorption can decrease compression strength. A 9% polyester resin reinforced with glass fiber was added to concrete and tested for compression strength. Due to the inability to bond sufficiently to the cement matrix, compression strength was reduced by 16% [1].

Pyrolysis is currently used as a method for recycling thermoset waste. Pyrolyzed plastics reinforced with glass fiber undergo heating in an inert environment. A pyrolytic oil of high calorific value remains and can be used for energy recovery [1]. The remaining glass components have been added to concrete in previous studies [1, 5]. Powdered remains from pyrolyzed SMC (Sheet Molding Compound) underwent testing for pozzolanic properties in one study. Results showed that pyrolyzed SMC did improve overall strength and reduced alkali-aggregate reactivity [5].

A pozzolan is described as a siliceous material that, in powdered form, can react with calcium hydroxide and demonstrate cementitious properties. An example of a commonly used pozzolan is fly ash from coal fired plants.

Another study conducted experiments to analyze the feasibility of incorporating the fine waste generated during the production of glass reinforced polymer composites into concrete mixtures. It was found that a 5% substitution of sand by powdered GRP led to tensile splitting strength and the modulus of elasticity were only marginally affected (reductions of 2.7% and 3.0%, respectively), but the compressive strength suffered a noticeable loss (19.4%) [4].

Overall, incorporating FRP powder and fiber waste was most effective at reducing crack propagation, but was not feasible for applications that would require high compression strength. It was suggested that powdered FRP reinforced concrete be used primarily for small load applications [4].

3. **Experimental methods**

Different configurations and components of fiber reinforced plastic (FRP) were added to concrete mix in different quantities. Details of the basic concrete mix can be found in Appendix A. Two test cylinders were cast for each material mix. Test cylinders had a volume of 100 in^3 (Height of 8” and diameter of 4”) and were wet cured for seven days. Each cast underwent vertical compression testing until failure. The maximum load was recorded. During compression tests, strain was recorded to yield a strain and stress relationship. Target compressive stress for the tests was 4,000 psi.

Figure 1. Cylinder during compression test.

Fiberglass cubes cut between 0.25 and 0.5 inches substitute 100% and 50% of the stone coarse aggregate component (100CAS

and 50CAS). The mix design for these trials involves equating the necessary volume of stone aggregate with the same volume of glass content in the fiberglass. After noticing the excessive volume of aggregate, two casts of 50% coarse aggregate substitution, or 50CAS, were made by equating the volume of necessary stone coarse aggregate with the total volume of the fiberglass (both resin and glass fiber). This will ensure adequate cement paste coverage around coarse aggregate. Only the 50CAS trial was tested with the new mix design due to better compressive performance and time constraints. Control mixes contained 0.25 - 0.5 inch stone aggregate.

Figure 2. Cubes of Fiberglass Coarse Aggregate.

Strips of full composite material were cut parallel to unidirectional fibers. The length of each strip was between 1.00 and 1.25 inches. The width of each strip was approximately 0.125 inches and was added at 1% (by volume of glass fiber content) of the mix.

Figure 3. FRP Strips.

Fibers from the unidirectional strands of glass fabric between 1.00 and 1.25 inches in length were added to concrete at both 1% and 2% by volume. Another two casts of 1% glass fiber were made with more dispersed fiber after encountering a clumping issue with the preliminary casts.

Figure 4. Virgin glass fibers cut from unidirectional strands.

The glass fiber that was recovered from pyrolyzed fiberglass was cut to a length between 1.00 and 1.25 inches and was added at 1% by volume. Fiberglass samples were pyrolyzed at 600° Celsius in an inert nitrogen gas environment for three hours.

Figure 5. Glass fiber remaining after pyrolysis.

4. Results

Results from the 50CAS, 100CAS and glass fiber cylinders show that lower volumes of FRP materials yielded higher compression strengths. The 100CAS had the most surface voids and had the lowest compression strength. The 50CAS and the 1% glass fiber mix had similar compression strengths. Preliminary glass fiber samples as well as the glass volume oriented coarse aggregate substitutions did not reach the target compressive stress of 4,000 psi. The samples shown in figure 6 underwent compression tests only.

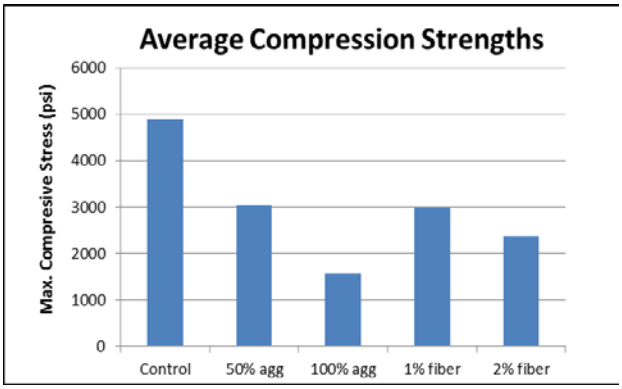

Figure 6. Compression data from preliminary samples.

The second set of samples underwent both compression testing and stress vs. strain analysis. This set of tests involved equal volume 50CAS, pre-mixed glass fiber, FRP strips, and pyrolysis fibers. Cylinders with FRP strips sustained the highest compressive stress at 5,153 psi and demonstrated a 13% improvement in compressive strength over the control samples. Cylinders with pyrolyzed fibers sustained the lowest compression stress at 3,240 psi and demonstrated a 27% decrease in compressive strength relative to the control samples. The equal volume 50CAS sustained a compressive stress comparable to that of the control. Only a 4% decrease in compressive strength was observed. Figure 7 shows the average maximum compressive stress for the second set of samples.

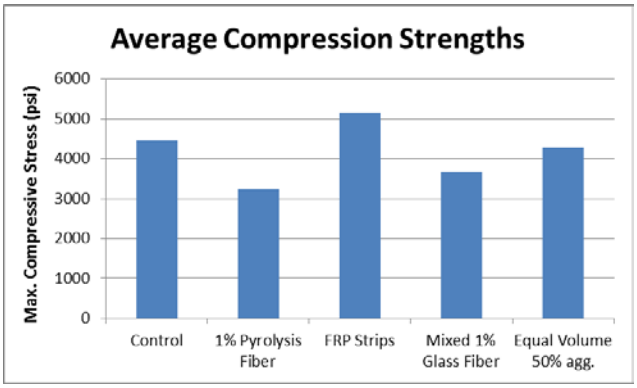

Figure 7. Compression data from secondary samples.

Reducing the volume of fiberglass coarse aggregate with the equal volume substitution increased compression strength by about 28%. Dispersing glass fiber before being added to the concrete mix increased compression strength by 18%.

The second set of samples also underwent strain analysis during compression tests. Figure 8 shows the stress to strain relation. Strain/stress curves terminate at failure stress.

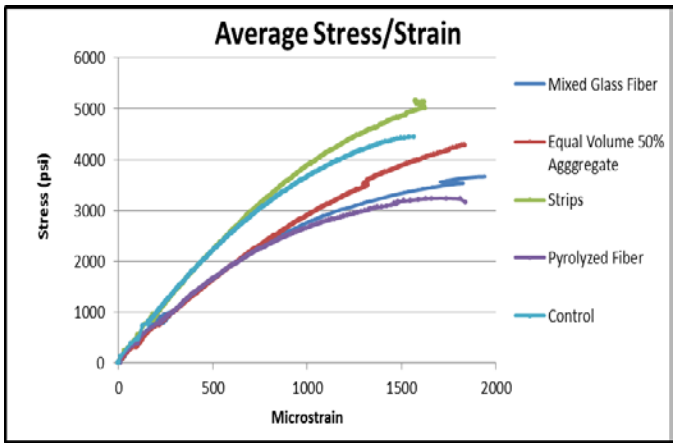

Figure 8. Stress and Strain relationship of secondary samples.

The mixed glass fiber cylinders showed the greatest strain value at failure stress. Equal volume 50CAS and pyrolyzed fibers showed similar strain values at failure. Control and FRP strip samples showed similar strain values at failure as well. Glass fibers had a 24% greater strain value than did the control. 50CAS strain at failure was 17% greater, strips were 0.6% greater, and pyrolyzed fiber was 11% greater. In this experiment, adding FRP materials increased strain values relative to the control.

Material	Maximum Microstrain	Maximum Stress (psi)
Control	1655	4455
Pyrolysis Fibers	1840	3240
Strips	1625	5153
Equal Volume 50% Aggregate	1850	4288
Mixed Glass Fiber	2100	3668

Figure 9. Table of maximum strain and stress.

Figure 9 shows the maximum strain and stress values for each material tested. Materials that contained resin (fiberglass cubes and strips) showed larger reductions in sample density. Mixtures that contained a 1% or 2% by volume additive did not show large changes in density relative to the control. The 50CAS had the most significant addition of FRP material to the concrete mix and had a 20% reduction in density. Figure 10 shows a relation between max compressive stress and the reduction in density relative to the control mix.

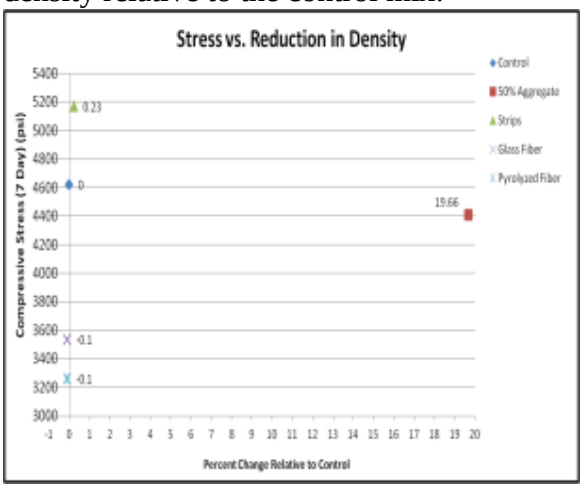

Figure 10. Relation between max. stress and density reduction

5. Analysis and interpretation

Through experimentation it was determined that the fiberglass aggregate volume should more closely substitute the volume component of stone aggregate that is being replaced. A volume percentage in terms of only the glass fiber component will lead to an excess volume of fiberglass aggregate. The excess surface area requires too much cement paste and will lead to voids if the mix is not adjusted. Mixes were redesigned to take into consideration the volume of the resin component in the fiberglass. Surface and internal voids may have led to lower compression strength with preliminary samples.

Clumps of fibers due to inadequate mixing increased the number of internal voids. Fractures usually occurred near large clumps of fibers. Mixing and dispersing the glass fibers before adding them to concrete improved compression strength by 18% but ultimately did not allow the sample to reach the target compression strength. Although clumping was reduced when pre-mixing was performed, glass fibers continued to clump together once wet.

Figure 11. Clump of glass fiber along fracture.

In previous studies, the maximum average length for fibers used for reinforcement was ~1 inch (20 mm). Fibers beyond that length may be more susceptible to clumping and poor mixing.

Poor cement bonding to flat resin surface on the fiberglass aggregate may mean that the material acted more as a foreign object than reinforcement. According to a previous study, geometric configuration plays a significant role in FRP performance as concrete reinforcement [3]. The sharp corners and flat faces of the fiberglass aggregate may have interfered with its ability to bond with and support the concrete matrix effectively. The elongated shape, as supposed to a cube, of the FRP strips may have aided compression strength by having a higher probability of bridging an impending fracture.

FRP strips may have also performed better than cubed FRP aggregate due to a higher ratio of surface area to volume. This ratio may improve the hardness of the cement paste through better bonding, elevating compression strength. Fiberglass cubes as aggregate may have yielded higher strain values because fiberglass is more flexible than limestone aggregate.

Slower and smaller breaks were noticed with glass fiber and pyrolyzed glass fiber samples. Fibers helped to prevent the usual sudden fracturing observed with the control groups. Stress and strain relationships show that although the ultimate compressive stress was lower for fibers, strain values were significantly higher than that of the control at failure (24% increase for glass fiber and 11% increase for pyrolyzed fiber).

The high volume of fiberglass coarse aggregate was effective in reducing density and also retained comparable compressive strength to that of the control. This particular test demonstrated that fiberglass as coarse aggregate can perform similar to regular concrete while reducing weight.

6. Conclusions

Effective mixing of fiber additives will be crucial to effective testing and utilization of fibers in concrete. Adding fibers in bulk to a wet concrete causes the fibers to stick together in wads and clumps. Agitating the fibers beforehand helped reduce visible clump formation and improved compression strength.

Adding fiberglass as coarse aggregate may increase strain values while retaining relatively higher compressive strengths than glass fibers. FRP coarse aggregate also has potential to significantly reduce density.

FRP strips in concrete increased compressive strength and stiffness. Mixes with FRP strips may have more potential for structural applications. Materials that produced higher strain values at lower stress failures may have potential for applications that require minimized crack propagation under smaller loads.

Acknowledgements

Support for this research was provided by a National Science Foundation Research Experience for Undergraduates site program in Wind Energy Science Engineering and Policy (WESEP) at Iowa State University.

References

P. Asokan, M. Osmani, A.D.F. Price, "Assessing the recycling potential of glass fibre reinforced plastic waste in concrete and cement composites," *Journal of Cleaner Production*, 17, pp. 821–829, 2009.

A. Conroy, S. Halliwell, T. Reynolds, "Composite recycling in the construction industry," *Composites*, 37, pp. 1216-1222, 2006.

Y. Wang, H. C. Wu, V.C. Li, "Concrete reinforcement with recycled fibers," *Journal of Materials in Civil Engineering*, 314-319, 2000.

J.R. Correia, N.M. Almeida, J.R. Figueira, "Recycling of FRP composites: reusing fine GFRP waste in concrete mixes," *Journal of Cleaner Production*, 19, pp. 1745-1753, 2011.

G.J. Xu, D.F. Watt, P.P. Hudec, K.A. MacDonald, D.O. Northwood, "Recycling automotive wastes in concrete," *Journal of Materials Processing Technology*, 48, pp. 385-390, 1995.

Appendices

A.

Materials	Specific Gravity	Abs (%)	SSD Batch Quantities c.y	
			Vol (cubic ft)	Wgt (lbs)
1/2" Limestone	2.68	1.06	7.53	1260
Regular Concrete Sand	2.60	1.4	10.85	1760
Type 1 Portland Cement	3.15	\	3.31	650
Water	1.00	\	4.81	300
Air	\	\	0.54	\
Fiber	\	\	\	\
Total	\	\	27.04	3970

Analysis of Wind Turbine Noise Using Semi-Empirical Noise Simulation Software

SAMUEL FRISHMAN
Wind Energy Science Engineering and Policy REU
Iowa State University
Ames, Iowa
Mentors: Dr. Anupam Sharma and Sunil Arolla

Abstract

The growth of wind as a source of energy has been driven by environmental concerns and goals of energy independence. Ultimately, however, for wind energy to become viable, it must be cost effective and publicly accepted. Aeroacoustics plays a significant role in both of these factors. As wind turbine blades rotate through the air, they produce a cyclic noise. This can disrupt the lives of local residents and must be considered before installing wind turbines in specific locations. In addition, as turbine sizes continue to grow, noise will only become an increasingly large issue. This paper documents work being done to create a computer program to simulate wind turbine noise production. The code utilizes existing simulators to create an aeroacoustic, wind turbine specific program.

1. Introduction

Noise generated by wind turbines is an important factor in the development of wind energy because it influences both the turbine dimensions and public acceptance of wind turbines. The National Wind Technology Center (NWTC) created a computer program called NAFNoise which predicts noise generated by an airfoil. This work focuses on creating a code that will iterate NAFNoise over a full turbine. This will allow for full turbine noise predictions and further improve simulation of wind turbine aeroacoustics. Similar software has been developed earlier (i.e. FAST), however it is not noise specific and has fewer noise related capabilities.

2. Literature review

NAFNoise (NREL Airfoil Noise, where NREL is the National Renewable Energy Laboratory) is a semi-empirical aeroacoustic noise prediction model developed by the NWTC. For given atmosphere conditions, airfoil properties, and other user determined settings, NAFNoise computes noise levels produced from five different airfoil sources: turbulent boundary layer trailing-edge noise, separated-flow noise, laminar boundary layer vortex-shedding noise, trailing-edge bluntness noise, and turbulent inflow noise. Sample schematics are provided in Appendix A. The noise sources are assumed independent and are combined to obtain the total noise produced by the airfoil. NAFNoise was built using semi-empirical relations determined by Brooks, Pope, and Marcolini (Brooks et al., 1989).

NAFNoise only has the capability of calculating noise produced by a single airfoil. In order to model a full turbine blade, which can be discretized into many airfoils, NAFNoise subroutines were integrated into an NREL simulator called FAST (Fatigue, Aerodynamics, Structures, and Turbulence). FAST's original purpose was to calculate fatigue loads; however, over time many features have been added to FAST. FAST discretizes the turbine blade into many pieces and calculates noise on each to obtain full turbine aeroacoustics.

NAFNoise was validated by comparing its noise level predictions to actual data. Predictions were compared to both wind tunnel tests and full-scale turbines.

Wind tunnel measurements were taken at the National Aerospace Laboratory in the Netherlands where both NACA 0012 and S822 airfoil models were tested. The results indicated that accuracy depends on angle of attack and sound frequency. The data and predictions were typically within 3dB apart, but there could be as much as 10dB difference.

A full-scale turbine comparison was done with an Atlantic Orient Corporation 15/50 turbine operated at the NWTC. There was only a 2-3dB difference between the predictions and the measured data.

3. Experimental methods

In this project, NAFNoise has been integrated with BEM (blade element momentum theory) code in order to obtain full turbine aeroacoustics. The following explains necessary information and illustrates the procedure through which the software runs.

In order to be executed, NAFNoise requires an input file. The input file contains properties of the airfoil for which NAFNoise calculates the noise level frequency distribution. In addition, the input file contains atmospheric parameters, XFOIL inputs, turbulent inflow noise inputs, the observer location at which noise levels are calculated, and other settings. A sample NAFNoise input file is provided in Appendix B.

To model full wind turbine noise, the turbine blades are discretized into individual airfoils with each airfoil having different properties, for example angle of attack and chord length. Properties of each airfoil are determined using blade element momentum theory (BEM). BEM equations calculate mean flow around the HAWT (horizontal axis wind turbine) and obtain quantities such as angle of attack, blade relative flow velocities, chord length, trailing edge thickness, and free-stream velocity for each airfoil of the turbine blade. In addition to varying properties, the relative position of an observer changes with respect to each airfoil. The relative position of each airfoil is calculated using matrix transformations.

The calculated properties and positions of an individual airfoil are fed into the NAFNoise input file. NAFNoise is executed and the noise levels omitted by that single airfoil are recorded to a total. Next, the properties and position of the airfoil in the next radial position are fed into the NAFNoise input file. NAFNoise is once again executed, and the noise levels emitted by the new airfoil are added to the total.

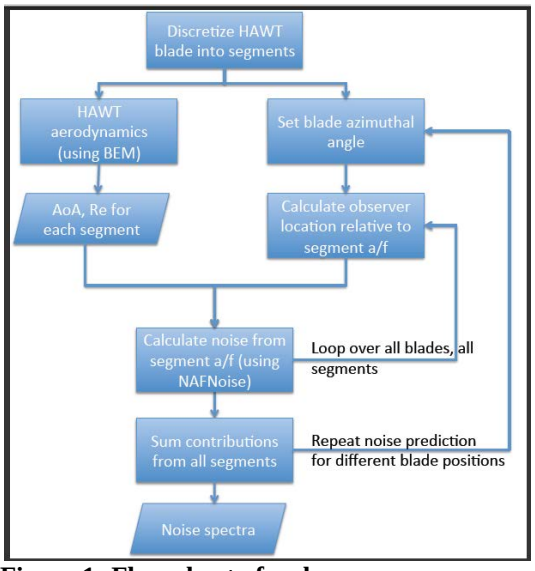

Figure 1: Flow chart of code

Through this process, NAFNoise is looped over the entire turbine blade. The process is repeated for all of the turbine blades to obtain noise emitted by a full wind turbine. Figure 1 is a flow chart illustration of the code.

4. Results

We have developed software that predicts aerodynamic noise from a Horizontal Axis Wind Turbine (HAWT). This software has been used to demonstrate the "swishing" noise wind turbine blades appear to make as they rotate. Noise levels experienced by the observer have been calculated at various blade positions. The results are presented in Figure 1. In this case, the observer is located at the bottom of the wind turbine, directly below the blade (at 180 degrees).

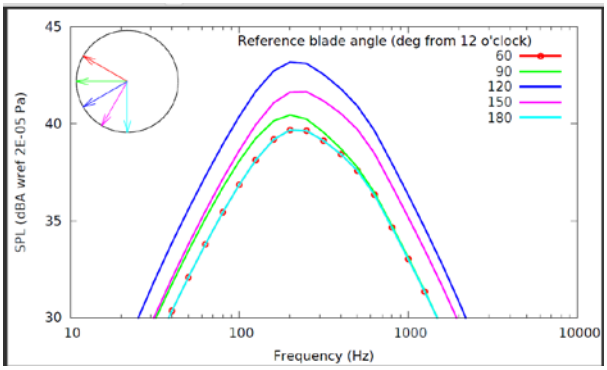

Fig 2: Noise levels at various blade positions

In Figure 2, the orientation of the turbine blades is determined by the angle of a single blade. The positions of this blade are depicted in the upper right hand corner of the graph. Figure 3 plots the logsum of noise across the entire frequency spectra as a function of blade position, demonstrating the overall noise heard by the observer.

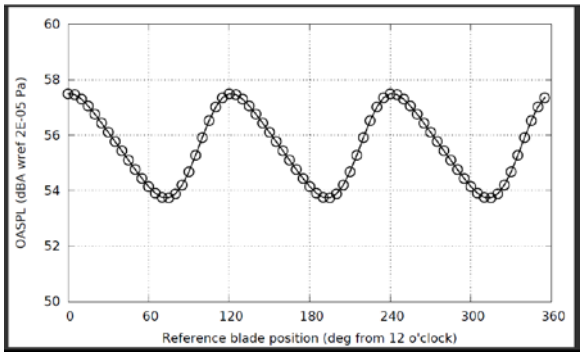

Fig 3: Noise as a function of blade position

Figure 3 shows noise levels at different positions around a single airfoil. The airfoil is located at the origin with the front facing to the left. The distance from the origin to a point any of the lines represents the magnitude of noise radiated in the direction defined by the line joining the point and the origin.

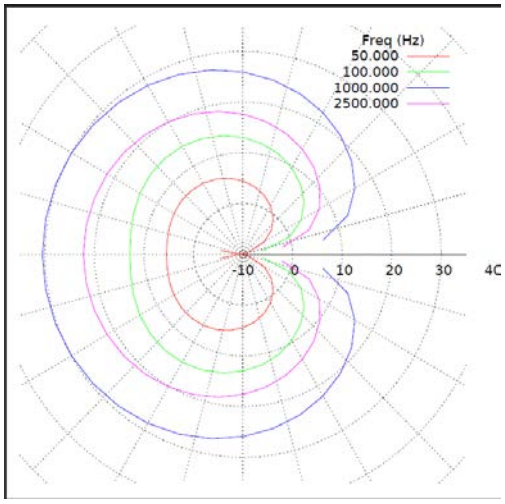

Fig 4: Noise levels around an airfoil

5. Analysis and interpretation

As seen from Figure 2 and Figure 3, the noise levels are periodic. The observer experiences the highest noise levels around factors of 120 degrees and the lowest noise levels around factors of 70 degrees.

The frequency distribution in Figure 1 shows that regardless of the blade position, the loudest noise (highest amplitude) is at about 250Hz.

Figure 4 illustrates a phenomenon known as directivity. The noise emitted by the airfoil is loudest in the forward (upstream) direction. Very little noise is observed behind (downstream) the airfoil.

6. Conclusions

The "swishing" noise experienced by an observer is caused by amplitude modulation. The amplitude of the noise spectra is higher

at certain blade orientations. This causes a louder noise at this orientation. In the scenario presented by the figures above, the observer hears the loudest noise when a blade is at the 120 degree mark (with 12 o'clock as 0 degrees).

The amplitude modulation is cause by several factors. A primary factor is directivity. The upstream direction of an airfoil experiences the loudest noise and thus, depending on where the observer is, certain blade positions cause the observer to hear a louder sound. Amplitude modulation is also a result of the changing distance between the observer and the noise source (the blades). A third factor influencing the amplitude modulation is Doppler amplification. Wind turbine blade tips rotate at speeds comparable to the speed of sound and thus Doppler effects are significant.

In addition to demonstrating the swishing noise, the developed software can be used to optimize turbine micrositing. The software can be used to predict how much noise local residents will experience if a turbine is placed in a specific location.

In the future, the code will be expanded to account for multiple observers and multiple wind turbines. This will allow for full wind farm noise modeling.

Acknowledgements

Support for this research was provided by a National Science Foundation Research Experience for Undergraduates site program in Wind Energy Science Engineering and Policy (WESEP) at Iowa State University.

References

Brooks, T., Pope, D., and Marcolini, M., "Airfoil Self-Noise and Prediction," NASA Reference Publication 1218, National Aeronautics and Space Administration, 1989.

Jonkma J., Buhl, M., "FAST User's Guide," National Renewable Energy Laboratory, 2005

Moriarty, P., Migliore P., "Semi-Empirical Aeroacoustic Noise Prediction Code for Wind Turbines," National Wind Technology Center, National Renewable Energy Laboratory, 2003

Moriarty, P., "NAFNoise User's Guide," National Wind Technology Center, National Renewable Energy Laboratory, 2005

Appendix A: Dominant Noise Sources

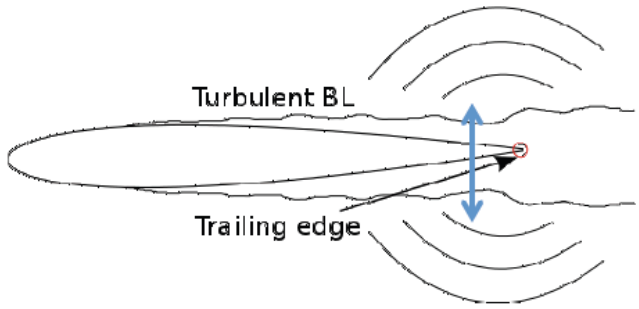

Trailing edge noise

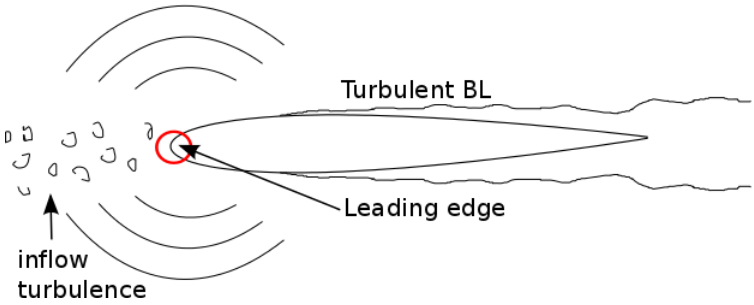

Leading edge noise

Appendix B: Sample NAFNoise Input File

```
Input file for 2-D aeroacoustic code
S809 Airfoil
---------------------- Atmospheric Constants ----------------------------------------
337.7559    C0              SPEED OF SOUND              METERS/SEC
1.4529e-5         VISC            KINEMATIC VISCOSITY         M2/SEC
1.225000    RHO             Air Density                         KG/M3
---------------------- Noise Calc Settings ------------------------------------------
2          ITRIP         Boudary layer trip no trip = 0 BPM, heavy trip = 1 (BPM only), light trip = 2
2          X_BLMethod    Integer describing calculation method for boundary layer properties,  =
1 BPM = 2 Xfoil
1          TBL_Method    Integer describing TBL noise calculation = 0 none =1 BPM = 2 TNO
3          TI_Method     Integer describing TI noise calculation = 0 none =1 Amiet (flat plate) = 2
Guidati = 3 Simplified Guidati
1          IBLUNT        FLAG TO COMPUTE BLUNTNESS NOISE    = 0 No, =1 Yes
1          ILAM          FLAG TO COMPUTE LBL NOISE          = 0 No, =1 Yes
---------------------- Airfoil Properties -------------------------------------------
0.2286      Chord Length                (m)
0.509       Airfoil Span                (m)
63.9200     Freestream Velocity         (m/s)
10.0000     Angle of Attack             (deg)
0.00021           Trailing Edge Thickness       (m)
12.5        PSI trailing edge solid angle  (deg)
---------------------- Xfoil Inputs -------------------------------------------------
0.02        XTR_upper = upper surface trip location  (normalized chord length)
0.1         XTR_lower = upper surface trip location  (normalized chord length)
.FALSE.     ISNACA = .TRUE. if Airfoil is a NACA else .FALSE.
s809.dat    Airfoil File Name or NACA Number (if spaces use quotes)
---------------------- Turbulent Inflow Noise Inputs ---------------------------
0.050       Turbulence Intensity            (%)
0.06          Turbulence Length Scale           (m)
0.02        Thickness @ 1% chord            (normalized thickness)
0.12        Thickness @ 10% chord           (normalized thickness)
40          Number of Streamlines           (Guidati full model)
0.005       Distance between streamlines        (Guidati full model)
---------------------- Observer Location --------------------------------------------
1.22          Observer Distance               (m)
90.             PHI angle relative to spanline     (deg)
90.         THETA angle relative to chordline  (deg)
```

Appendix C: Sample NAFNoise Output File

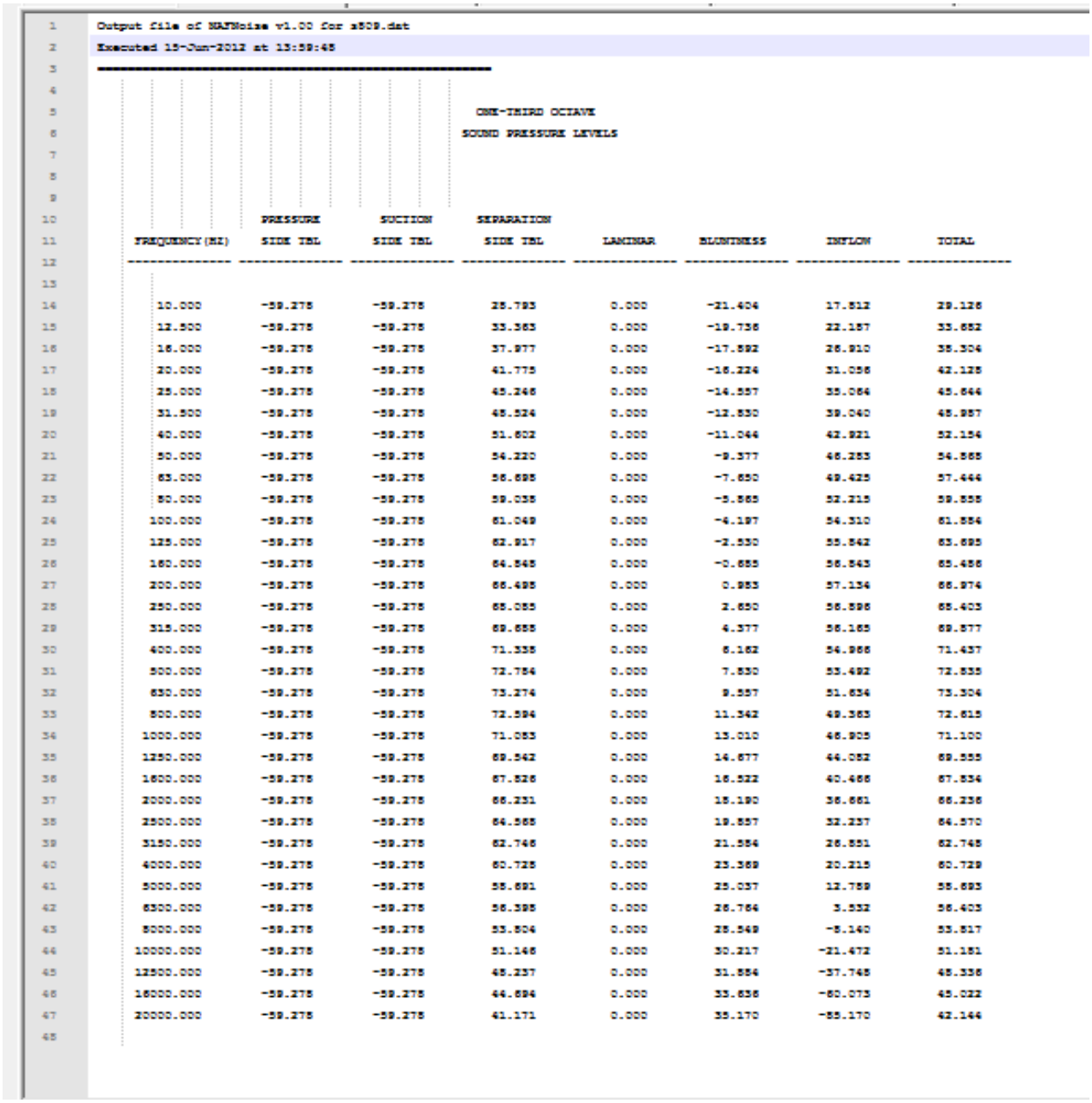

Output file of NAFNoise v1.00 for a500.dat
Executed 15-Jun-2012 at 15:59:45

ONE-THIRD OCTAVE
SOUND PRESSURE LEVELS

FREQUENCY (Hz)	PRESSURE SIDE TBL	SUCTION SIDE TBL	SEPARATION SIDE TBL	LAMINAR	BLUNTNESS	INFLOW	TOTAL
10.000	-59.275	-59.275	25.795	0.000	-21.404	17.812	29.126
12.500	-59.275	-59.275	33.365	0.000	-19.736	22.157	33.682
16.000	-59.275	-59.275	37.977	0.000	-17.892	26.910	38.304
20.000	-59.275	-59.275	41.775	0.000	-16.224	31.056	42.128
25.000	-59.275	-59.275	45.246	0.000	-14.557	35.064	45.644
31.500	-59.275	-59.275	48.524	0.000	-12.830	39.040	48.987
40.000	-59.275	-59.275	51.602	0.000	-11.044	42.921	52.154
50.000	-59.275	-59.275	54.220	0.000	-9.377	46.283	54.868
63.000	-59.275	-59.275	56.695	0.000	-7.650	49.425	57.444
80.000	-59.275	-59.275	59.038	0.000	-5.865	52.215	59.858
100.000	-59.275	-59.275	61.049	0.000	-4.197	54.310	61.884
125.000	-59.275	-59.275	62.917	0.000	-2.530	55.842	63.695
160.000	-59.275	-59.275	64.845	0.000	-0.655	56.843	65.486
200.000	-59.275	-59.275	66.495	0.000	0.953	57.134	66.974
250.000	-59.275	-59.275	65.055	0.000	2.650	56.896	65.403
315.000	-59.275	-59.275	69.655	0.000	4.377	56.165	69.577
400.000	-59.275	-59.275	71.335	0.000	6.162	54.966	71.437
500.000	-59.275	-59.275	72.754	0.000	7.830	53.492	72.835
630.000	-59.275	-59.275	73.274	0.000	9.557	51.634	73.304
800.000	-59.275	-59.275	72.594	0.000	11.342	49.365	72.615
1000.000	-59.275	-59.275	71.055	0.000	13.010	46.905	71.100
1250.000	-59.275	-59.275	69.542	0.000	14.677	44.052	69.555
1600.000	-59.275	-59.275	67.526	0.000	16.522	40.466	67.534
2000.000	-59.275	-59.275	66.231	0.000	18.190	38.661	66.236
2500.000	-59.275	-59.275	64.565	0.000	19.857	32.237	64.570
3150.000	-59.275	-59.275	62.746	0.000	21.584	26.851	62.745
4000.000	-59.275	-59.275	60.725	0.000	23.369	20.215	60.729
5000.000	-59.275	-59.275	58.691	0.000	25.037	12.759	58.693
6300.000	-59.275	-59.275	56.395	0.000	26.764	3.532	56.403
8000.000	-59.275	-59.275	53.804	0.000	28.549	-5.140	53.817
10000.000	-59.275	-59.275	51.146	0.000	30.217	-21.472	51.151
12500.000	-59.275	-59.275	48.237	0.000	31.884	-37.745	48.336
16000.000	-59.275	-59.275	44.694	0.000	33.636	-60.073	45.022
20000.000	-59.275	-59.275	41.171	0.000	35.170	-85.170	42.144